Karlsruhe Institute of Technology

Optics in Self-Assembled Metamaterials

Zur Erlangung des akademischen Grades eines
Doktors der Naturwissenschaften
(Dr. rer. nat.)

bei der Fakultät für Physik
des Karlsruher Instituts für Technologie (KIT)

genehmigte
DISSERTATION

von

M. Sc. Martin Fruhnert

Datum der mündlichen Prüfung:	27. Januar 2017
Referent:	Prof. Dr. Carsten Rockstuhl
Korreferent:	Prof. Dr. Martin Wegener

Ich habe nur die angegebenen Quellen und Hilfsmittel benutzt und mich keiner unzulässigen Hilfe Dritter bedient. Insbesondere habe ich wörtlich oder sinngemäß aus anderen Werken übernommene Inhalte als solche kenntlich gemacht.

Karlsruhe, den 16. Dezember 2016

Abstract

How does an object scatter or absorb electromagnetic radiation? It is often a non-trivial task to answer this question. A very elegant analytic solution can be found for a single sphere by expanding the fields into vector spherical harmonic functions and connecting their amplitudes with the Mie coefficients of the sphere. However, for general arbitrarily shaped objects, such an analytic solution does not exist. In this thesis, an approach is used that is very similar to the case of the single sphere. The amplitudes of the incident and scattered fields are connected by the transfer or T-matrix, instead of the Mie coefficients. We present a method to obtain the T-matrix of arbitrary objects. Furthermore, an extension is shown, where the scattering from several of such objects forming a cluster can be calculated.

We use this framework to study the interaction of single objects with light on the one hand and light propagation in metamaterials made out of many identical objects on the other hand. We focus on objects and materials that are suitable for self-assembly fabrication techniques. Such methods offer several key benefits, which are highlighted throughout the thesis.

After introducing the theoretical basis, we investigate in detail metamaterials that are composed of spheres and spherical shells. A main goal in this context is the availability of a three dimensional material that exhibits a magnetic response. This can ultimately lead to a material with a negative effective index of refraction. We present a metamaterial that attains a negative index of refraction theoretically and back it up by numerical calculations. For these calculations we use an extension to the Mie scattering for multiple spheres. Then, the aforementioned T-matrix method is introduced. We show how to calculate the T-matrix of arbitrarily shaped objects. Finally, we apply this T-matrix method to get a deeper understanding of the scattering behavior of complexly shaped objects. Three interesting concepts are investigated. First, the scattering cancellation of a dipolar particle with a tunable operating frequency in the visible spectrum. To achieve this, we use ellipsoidal particles instead of spheres in the scattering cancellation device. Second, we investigate the electromagnetic chirality of scattering objects. Its definition is based on the T-matrix of the object. We use this definition to design an optimally chiral object. Finally, we consider the homogenization of a three dimensional metamaterial. We compare full wave simulations of a larger number of metaatoms, obtained from our multiple T-matrix scattering method, to the case of a homogeneous effective medium. The results show very good agreement, confirming the validity of the approach.

In summary, we show that it is very valuable to have the T-matrix of an interesting object available and that it provides information, which is not accessible if conventional full wave methods are used.

Publications

Publications whose contents are part of this thesis are highlighted in bold.

[1] **M. Fruhnert, S. Mühlig, F. Lederer, and C. Rockstuhl, "Towards negative index self-assembled metamaterials,"** ***Physical Review B*****, vol. 89, no. 7, p. 075408, 2014.**

[2] **F. Kretschmer, M. Fruhnert, R. Geiss, U. Mansfeld, C. Höppener, S. Hoeppener, C. Rockstuhl, T. Pertsch, and U. S. Schubert, "Plasmonic nanoparticle clusters with tunable plasmonic resonances in the visible spectral region,"** ***Journal of Materials Chemistry C*****, vol. 2, no. 31, pp. 6415–6422, 2014.**

[3] **W. Lewandowski, M. Fruhnert, J. Mieczkowski, C. Rockstuhl, and E. Górecka, "Dynamically self-assembled silver nanoparticles as a thermally tunable metamaterial,"** ***Nature Communications*****, vol. 6, no. 6590 2015.**

[4] **I. Fernandez-Corbaton, M. Fruhnert, and C. Rockstuhl, "Dual and chiral objects for optical activity in general scattering directions,"** ***ACS Photonics*****, vol. 2, no. 3, pp. 376–384, 2015.**

[5] **M. Fruhnert, F. Kretschmer, R. Geiss, I. Perevyazko, D. Cialla-May, M. Steinert, N. Janunts, D. Sivun, S. Hoeppener, M. D. Hager,** ***et al.*****, "Synthesis, separation, and hypermethod characterization of gold nanoparticle dimers connected by a rigid rod linker,"** ***The Journal of Physical Chemistry C*****, vol. 119, no. 31, pp. 17809–17817, 2015.**

[6] M.-S. Kim, T. Scharf, S. Mühlig, M. Fruhnert, C. Rockstuhl, R. Bitterli, W. Noell, R. Voelkel, and H. P. Herzig, "Refraction limit of miniaturized optical systems: a ball-lens example," *Optics Express*, vol. 24, no. 7, pp. 6996–7005, 2016.

[7] **I. Fernandez-Corbaton, M. Fruhnert, and C. Rockstuhl, "Objects of maximum electromagnetic chirality,"** ***Physical Review X*****, vol. 6, p. 031013, 2016.**

[8] **M. Fruhnert, A. Monti, I. Fernandez-Corbaton, A. Alù, A. Toscano, F. Bilotti, and C. Rockstuhl, "Tunable scattering cancellation cloak with plasmonic ellipsoids in the visible,"** ***Physical Review B*****, vol. 93, no. 24, p. 245127, 2016.**

[9] A. Rahimzadegan, M. Fruhnert, R. Alaee, I. Fernandez-Corbaton, and C. Rockstuhl, "Optical force and torque on dipolar dual chiral particles," *Physical Review B*, vol. 94, no. 12, p. 125123, 2016.

[10] **M. Fruhnert, I. Fernandez-Corbaton, V. Yannopapas, and C. Rockstuhl, "Computing the T-matrix of a scattering object with multiple plane wave illuminations," Submitted to** ***Beilstein Journal of Nanotechnology*****, 2016.**

[11] R. N. S. Suryadharma, M. Fruhnert, I. Fernandez-Corbaton, and C. Rockstuhl, "Studying Plasmonic Resonance Modes of Hierarchical Self-Assembled Meta-Atoms based on their Transfer-Matrix," Submitted to *Physical Review B*, 2016.

Conference contributions

Conference contributions with presentations done by myself are highlighted in bold.

1. **M. Fruhnert, S. Mühlig, F. Lederer, and C. Rockstuhl, "Towards negative index self-assembled metamaterials,"** ***Metamaterials 2013*****, Bordeaux, France, September 2013.**
2. **M. Fruhnert, S. Mühlig, F. Lederer, and C. Rockstuhl, "Tunable magnetic dipole response of core-shell clusters,"** ***DoKDoK 2013*****, Suhl, Germany, October 2013.**
3. I. Fernandez-Corbaton, M. Fruhnert, and C. Rockstuhl, "Dual and chiral dielectric scatterers for optical activity in general directions," *PIERS 2015*, Prague, Czech Republic, July 2015.
4. **M. Fruhnert, W. Lewandowski, J. Mieczkowski, E. Górecka and C. Rockstuhl, "Dynamically self-assembled silver nanoparticles as a thermally tunable metamaterial,"** ***Metamaterials 2015*****, Oxford, United Kingdom, September 2015.**
5. I. Fernandez-Corbaton, M. Fruhnert, and C. Rockstuhl, "Dual And Chiral Objects For Optical Activity In General Scattering Directions," *Metamaterials 2015*, Oxford, United Kingdom, September 2015.
6. **M. Fruhnert, I. Fernandez-Corbaton, and C. Rockstuhl, "Optics in Self Assembled Metamaterials,"** ***Karlsruhe Days of Optics & Photonics 2015*****, Karlsruhe, Germany, November 2015.**
7. S. A. Schmid, R. N. S. Suryadharma, M. Fruhnert, C. Klusmann, H. Kalt, and C. Rockstuhl, "Studying the interplay of nanoparticles and dielectric whispering gallery mode resonators using a generalized Mie theory," *DPG spring meeting 2016*, Regensburg, Germany, March 2016.
8. C. Rockstuhl, M. Fruhnert, W. Lewandowski, J. Mieczkowski, and E. Górecka, "Thermally tunable self-assembled metamaterials," *CIMTEC 2016*, Perugia, Italy, June 2016.
9. I. Fernandez-Corbaton, M. Fruhnert, and C. Rockstuhl, "Electromagnetic Duality Symmetry in Optical Activity," *META 16*, Malaga, Spain, July 2016.
10. I. Fernandez-Corbaton, M. Fruhnert, and C. Rockstuhl, "How Optically Chiral a Chiral Object can be?," *EOSAM 2016*, Berlin, Germany, September 2016.

Abbreviations

CD	Circular dichroism
DBU	Diazabicycloundecene
FEM	Finite element method
SEM	Scattering electron microscopy
SERS	Surface enhanced Raman spectroscopy
T-matrix	Transfer matrix
TEM	Transmission electron microscopy

Contents

1 Introduction

How does light interact with a certain object?

and

How does light propagate through a material composed of such objects?

These are the central questions, which we are going to answer in this thesis.
Naturally available materials are commonly described by material properties such as the permittivity $\varepsilon(\omega)$ and the permeability $\mu(\omega)$. These are dispersive quantities that depend on the frequency ω of the impinging electromagnetic radiation. This is possible, despite the fact that these materials are made up of individual building blocks: atoms and molecules. Such a homogeneous description is applicable, because the atoms and the distance to their nearest neighbors are much smaller than the wavelength of the illumination. The optical response of the atoms can be very well approximated by that of electric dipoles. With this concept in mind, artificial materials, called metamaterials, where invented. These metamaterials are likewise made out of smaller building blocks, called metaatoms in reminiscence to real atoms that make up natural materials. These metaatoms and their respective distance should also be small when compared to the wavelength to allow for an effective description of the metamaterial. Then, the propagation of light in such a material can be described much simpler, by replacing the potentially very complex structure of the large number of metaatoms with a homogeneous material. This conceptual homogeneous material shall be described by effective material parameters. In order to determine the properties of the resulting metamaterial it is of utmost importance to know the electromagnetic response of the constituting metaatoms to an external illumination.

With state-of-the-art fabrication methods, it is possible to produce metamaterials with unprecedented properties. In natural materials the effective properties are governed by the polarizability of the atoms and molecules. However, these atoms and molecules are usually well approximated as electric dipoles. Thus, a dispersion in the permeability, which would require a magnetic polarizability of the building blocks is not found in natural materials. The first attempts to realize artificial materials were conducted in the microwave regime by David Smith and coworkers [12]. A material with a notable magnetic response was created by using split ring resonators as building blocks. These split ring resonators exhibit a magnetic dipole moment when they are excited by external electromagnetic fields. This behavior was predicted theoretically by Sir John Pendry and coworkers [13]. The proof of principle that such artificial materials are possible spurred research in this direction and created a whole new field of theoretical and experimental physics.

With top-down fabrication, complicated metaatoms can be created on a substrate. Usually such fabrication techniques involve a lithography step, where the material is treated for example with lasers [14,15], electron beams [16,17], or ion beams [18,19]. In the beginning, these pioneering work concentrated on metamaterials with special properties in the microwave regime, mainly because the precision of the fabrication techniques was not sufficient to create structures of the size necessary to reach the optical regime. In the recent years, top-down methods developed rapidly to allow tremendous precision and the optical domain was reached.

However, these top-down fabrication techniques also have some notable downsides. For many interesting applications, we want a metamaterial that has a three dimensional volume. Typically, the aforementioned lithography procedures allow only the fabrication of an approximately two dimensional arrangement with limited control of the height on the substrate. Furthermore, top-down techniques are optimized to fabricate multiple metaatoms at the same time or as fast as possible after each other. This usually restricts the arrangement of the metaatoms on the substrate to a highly ordered lattice. For some applications such an arrangement is advantageous. However, often we need an isotropic response of the material, for example to avoid problems at oblique illuminations. Such an isotropic response is not possible if anisotropic metaatoms are ordered with the same alignment. However, if they were placed in a random orientation, the response would be approximately isotropic.

These two problems can be solved with self-assembly techniques. The basic idea of self-assembly is to mimic nature in the way organisms are formed. As opposed to the fully deterministic process of top-down fabrication, self-assembly is driven for example by chemical processes [5,20], electrostatic forces [21–23], or biological processes [24,25]. Thus, the self-assembly fabrication can only be controlled indirectly.

The major selling point of self-assembled metamaterials is that they are usually inherently available as a three dimensional material. Metaatoms are formed in solution, which results in an isotropic three dimensional distribution. The resulting mixture can be further densified to reach the desired concentration. See Fig. 1.1 for examples of top-down fabricated and self-assembled metaatoms.

So far, an impressive number of interesting theoretical concepts has been proposed

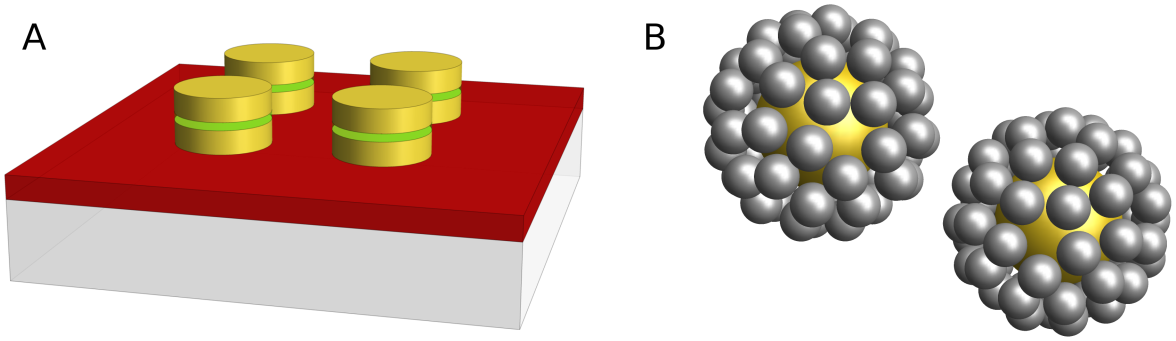

Figure 1.1: Schematic visualization of metaatoms fabricated with (A) top-down methods and (B) self-assembly methods.

in the fields of metamaterials. Many of these suggestions were already realized experimentally with considerable success. Notable examples are perfect absorbers [26–28], cloaks that can hide objects from detection [29–32], chiral materials which react differently to the two circular polarizations of light [33–37], and materials with a strong magnetic response [23, 38, 39], which can lead ultimately to a material with a negative index of refraction [1, 40, 41].

Furthermore, there are other branches of metamaterial science beyond the electromagnetic realm. Most notably, there are applications for mechanical metamaterials, in the area of acoustics [42, 43], elastostatics [44, 45], and fluid dynamics [46]. Moreover, artificial materials are also used in thermodynamics [47, 48]. Even though these fields are intriguing, they lie beyond the focus of this thesis and are not further considered.

State-of-the-art metamaterial designs cover a large fraction of the electromagnetic spectrum from radio waves [49, 50], microwaves [12, 51], the infrared regime [52–54], the visible spectrum [55–57], up to the ultraviolet regime [58, 59]. In the context of this thesis, we focus mainly on metamaterials in the optical regime, ranging in frequency from approximately 400 THz to 800 THz or, if we consider wavelengths, approximately from 400 nm to 800 nm.

Structure of the thesis

In this thesis we investigate the scattering behavior of specific objects. For this purpose, it is mandatory to introduce the fundamental theoretical concepts in the following chapter 2. There we show a method to calculate the scattered fields of an illuminated sphere. The electromagnetic fields are expanded into vector spherical harmonic functions. Such a decomposition is especially advantageous to describe the spherically symmetric problem of a scattering sphere. Then the incident and scattered electromagnetic fields are described by the expansion coefficients, called incident and scattering coefficients, respectively. Furthermore, an extension is presented to calculate the scattering by multiple spheres self-consistently with the multiple Mie scattering method. Within this method, the scattered field of each sphere is calculated by taking not only the external illumination into account, but also the scattered fields of all other spheres.

Afterwards, we show two important methods to homogenize materials made out of small particles: the surface homogenization and the volumetric homogenization. The surface homogenization is suitable to describe thin, quasi two dimensional layers in an effective way. The layer is modeled as an infinitely thin interface to which we can attribute a surface impedance. Alternatively, we use the volumetric homogenization to describe extended three dimensional structures. Here, the structure is modeled as a solid homogeneous material with effective properties $\varepsilon_{\text{eff}}(\omega)$ and $\mu_{\text{eff}}(\omega)$.

The chapter is concluded by an introduction to duality symmetry and the helicity of light. The helicity of an electromagnetic wave is a relativistically invariant property that describes the handedness of the wave. A circularly polarized plane wave is an example of a wave of pure helicity. If an object does not change the helicity of the light it interacts with, it is called dual symmetric.

In chapter 3, we apply the multiple Mie scattering method to investigate numerically the scattering behavior of metaatoms which are composed of spheres. Thereby, we focus also on the possible fabrication of such metaatoms. We introduce a design of a metaatom that exhibits a strong magnetic dipole resonance which is suitable for self-assembly fabrication. The design is further extended to sustain a magnetic and electric resonance in the same spectral region. This leads to a negative effective index of refraction of a metamaterial made out of the proposed metaatoms.
After this theoretical study, we investigate possible realizations of metaatoms with interesting optical properties. Hereby, we tightly collaborate with experimental partners and provide useful insights into the interaction of the investigated objects with light.
Finally, a dynamically tunable metamaterial is proposed. We show the design of a metamaterial consisting of silver nanospheres connected by a liquid crystal. The liquid crystal changes its geometrical structure depending on the temperature. Thus, we can switch the geometrical structure of the silver spheres by changing the temperature dynamically and reversibly. Thereby, the optical response of the material is likewise changed.

In chapter 4 we present an extension to the multiple Mie scattering method to include arbitrary objects instead of spheres. The scattering information of an object can be represented by the transition matrix, called T-matrix throughout this thesis. This matrix connects the incident and scattering coefficients. It depends only on the geometry and material composition of the considered object.
We present two methods to calculate the T-matrix. The first is suitable to consider clusters of spheres and is based on the multiple Mie scattering algorithm. The second method is more general and allows to calculate the T-matrix of an arbitrarily shaped object.
Finally, we present a multiple T-matrix scattering method. This algorithm makes it possible to calculate the collective scattering by multiple arbitrarily shaped objects.

In the last chapter, we investigate metaatoms made out of arbitrarily shaped objects. We apply the previously introduced multiple T-matrix scattering method to gain insights into the scattering behavior of the considered objects.
We present a novel design of a scattering cancellation device. Most notably the scattering response of a core object is reduced at a tunable frequency. This is possible because we employ ellipsoidal nanoparticles instead of nanospheres in the shell that cancel the scattering. This way we are able to tune the operating frequency by changing the aspect ratio of the constituting ellipsoids. The results obtained from the multiple T-matrix scattering method are compared to analytically obtained results, where the shell is homogenized with the methods introduced in chapter 2.
Subsequently, we investigate the chirality of scattering objects. A new definition of electromagnetic chirality is introduced. This definition allows a quantitative classification of scattering objects. We underpin our definition by investigating a realistic object that achieves a strong value of electromagnetic chirality at resonance, a silver helix. This is achieved by calculating the T-matrix of the object numerically.

From the T-matrix we obtain the value of the electromagnetic chirality which we maximize by varying the geometrical parameters of the helix.

Finally, we present a scheme to construct a metamaterial with complexly shaped metaatoms. This is done by combining the top-down fabrication with self-assembly methods to benefit from the respective advantages of both methods. Metaatoms are fabricated with high precision by top-down methods. Then, they are lifted off of the substrate and distributed in a random isotropic manner. We investigate exemplary a metaatom that consists of two separated metal disks. The resulting three dimensional metamaterial is then described with a full wave simulation using the multiple T-matrix scattering method. Additionally, we perform a volumetric homogenization of the metamaterial and calculate the effective material parameters. Ultimately, we compare the results of the full simulation to a simulation of a homogeneous object with the obtained effective parameters to demonstrate the validity of the approach.

2 Theory

In this chapter, we introduce the theoretical foundation of this thesis. In the first section, we give an introduction to the electromagnetic scattering theory of spheres. The scattering by a single sphere in a homogeneous isotropic medium can be described fully analytically, which was first described by Gustav Mie [60]. With an extension, it is also possible to calculate self-consistently the scattered fields for a finite cluster of spheres. This extension constitutes a very powerful tool to describe the optical properties of metallic or dielectric nanosphere clusters in the context of several practical applications. We use this multiple Mie scattering method to a great extent in chapter 3.

In the second section, we discuss how metamaterials made from basic scatterers can be homogenized. A simple and effective description as a material with effective properties in the case of a bulk material or as a surface in the case of a planar material is outlined. In many cases we can apply the dipole-approximation to describe the scattering response of small scattering objects. This requires considering only the induced electric and magnetic dipole moments. Then, a bulk material or a surface consisting of these scattering building blocks can be modeled as an effective homogeneous entity with specific optical properties.

Finally, we provide insights into the electromagnetic duality symmetry of objects and the closely related helicity. In a nutshell, an electromagnetic scatterer is considered to be dual, if its electric and magnetic responses are balanced. This duality symmetry preserves an observable quantity: the helicity of the field.

2.1 Electromagnetic scattering

When electromagnetic radiation, such as light, interacts with a particle, usually two phenomena occur. Light can be absorbed or scattered. The quantitative extent of this absorption and scattering depends strongly on the properties of the particle, such as its size, shape, and the intrinsic properties of the materials the particle is made of. Because in general, this can lead to very complex calculations, we want to focus in this section on the special case of spherical scatterers. In essence, we are always solving Maxwell's equations in the frequency domain

$$\nabla \cdot \mathbf{E}(\mathbf{r}, \omega) = 0, \tag{2.1}$$

$$\nabla \cdot \mathbf{H}(\mathbf{r}, \omega) = 0, \tag{2.2}$$

$$\nabla \times \mathbf{E}(\mathbf{r}, \omega) = \mathrm{i}\omega\mu(\omega)\mathbf{H}(\mathbf{r}, \omega), \tag{2.3}$$

$$\nabla \times \mathbf{H}(\mathbf{r}, \omega) = -\mathrm{i}\omega\varepsilon(\omega)\mathbf{E}(\mathbf{r}, \omega). \tag{2.4}$$

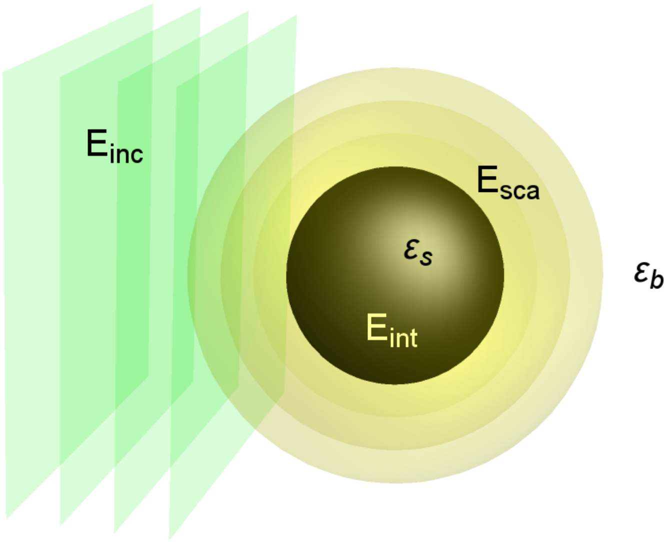

Figure 2.1: Schematic representation of the incident $\mathbf{E}_{\mathrm{inc}}$, scattered $\mathbf{E}_{\mathrm{sca}}$, and internal field $\mathbf{E}_{\mathrm{int}}$ of a sphere.

Here, $\mathbf{E}(\mathbf{r}, \omega)$ is the electric field, $\mathbf{H}(\mathbf{r}, \omega)$ is the magnetic field, $\mathbf{r}$ is the spatial coordinate, ω is the frequency, and $\varepsilon(\omega)$ and $\mu(\omega)$ are the permittivity and permeability of the considered material, respectively. Throughout the thesis, we denote vectors and vector fields with bold characters.

2.1.1 Scattering by a single sphere

In this section, we consider the scattering of light by a single sphere, as seen schematically in Fig. 2.1. Contrary to arbitrarily shaped objects, the scattering by a sphere can be solved fully analytically. This case is very relevant, because many self-assembled metaatoms are either composed of spheres or can be approximated as such.

Wave equation

We start with the vector wave equations (also called Helmholtz equation), which directly follow from Maxwell's equations 2.1-2.4 [61]

$$\nabla^2\mathbf{E}(\mathbf{r}, \omega) + k^2\mathbf{E}(\mathbf{r}, \omega) = 0 \tag{2.5}$$

$$\nabla^2\mathbf{H}(\mathbf{r}, \omega) + k^2\mathbf{H}(\mathbf{r}, \omega) = 0, \tag{2.6}$$

where $\mathbf{k}$ is the wave vector. The dispersion relation requires that

$$k^2 = |\mathbf{k}|^2 = \omega^2\varepsilon(\omega)\mu(\omega). \tag{2.7}$$

Here, $\varepsilon(\omega) = \varepsilon_{\mathrm{r}}(\omega)\varepsilon_0$ where ε_0 is the free space permittivity and $\varepsilon_{\mathrm{r}}(\omega)$ is the relative permittivity of the material. Analogously we have $\mu(\omega) = \mu_{\mathrm{r}}(\omega)\mu_0$.

To exploit the symmetry of the problem, spherical coordinates are adopted. This simplifies the wave equation considerably. We consider a scalar function $\psi(\mathbf{r},\omega)$ and an arbitrary constant vector $\mathbf{c}$ (the guiding vector) and construct a vector function $\mathbf{M}(\mathbf{r},\omega)$ as

$$\mathbf{M}(\mathbf{r},\omega) = \nabla \times (\mathbf{c}\psi(\mathbf{r},\omega)) \tag{2.8}$$

with vanishing divergence. We insert this into the vector wave equation and get

$$\nabla^2\mathbf{M}(\mathbf{r},\omega) + k^2\mathbf{M}(\mathbf{r},\omega) = \nabla \times [\mathbf{c}(\nabla^2\psi(\mathbf{r},\omega) + k^2\psi(\mathbf{r},\omega))] = 0. \tag{2.9}$$

From the right hand side of Eq. 2.9 we extract the scalar wave equation

$$\nabla^2\psi(\mathbf{r},\omega) + k^2\psi(\mathbf{r},\omega) = 0. \tag{2.10}$$

This implies that if $\psi(\mathbf{r},\omega)$ is a solution to the scalar wave equation then $\mathbf{M}(\mathbf{r},\omega)$ satisfies the vector wave equation. Now we construct a second vector function $\mathbf{N}(\mathbf{r},\omega)$ as

$$\mathbf{N}(\mathbf{r},\omega) = \frac{\nabla \times \mathbf{M}(\mathbf{r},\omega)}{k}. \tag{2.11}$$

This function is by definition divergence free and also satisfies the vector wave equation. Additionally, $\mathbf{M}$ and $\mathbf{N}$ satisfy the relation $\nabla \times \mathbf{N}(\mathbf{r},\omega) = k\mathbf{M}(\mathbf{r},\omega)$ and, therefore, have all the properties of electromagnetic fields. This can be appreciated by applying $\nabla\times$ to Eq. 2.11 and inserting the wave equation. Now, in order to have a solution to the vector wave equation, it is only required to solve the much simpler scalar wave equation 2.10 for the generating function $\psi(\mathbf{r},\omega)$. Then, the solutions to the vector wave equation can be constructed using Eqs. 2.8 and 2.11. The two functions are called vector harmonic functions.

In the present case of a scattering sphere, the generating function $\psi(\mathbf{r},\omega)$ should be a solution to the scalar wave equation in spherical coordinates. As the guiding vector $\mathbf{c}$, we take the position vector $\mathbf{r}$ in order to ensure that $\mathbf{M}(\mathbf{r},\omega)$ is a solution to the vector wave equation in spherical coordinates. Then we get the generating function with a separation ansatz as [62]

$$\psi_{nm}^{(l)}(\mathbf{r},\omega) = z_n^{(l)}(kr,\omega)P_n^m(\cos\theta)\mathrm{e}^{\mathrm{i}m\phi}, \tag{2.12}$$

where $r = |\mathbf{r}|$. $P_n^m(\cos\theta)$ are associated Legendre functions and $z_n^{(l)}(kr,\omega)$ are Bessel functions of first or second kind $[z_n^{(1)}(kr,\omega) = j_n(kr,\omega)$ and $z_n^{(2)}(kr,\omega) = y_n(kr,\omega)]$ or Hankel functions of first or second kind $[z_n^{(3)}(kr,\omega) = h_n^{(1)}(kr,\omega)$ and $z_n^{(4)}(kr,\omega) = h_n^{(2)}(kr,\omega)]$, respectively. The indices take the values $n = 1, 2, \ldots$ and $m = -n, -n+1, \ldots, n-1, n$, respectively. Every solution to the wave equation can be expressed as a series of these functions

$$\begin{aligned}\mathbf{M}^{(l)}_{nm}(\mathbf{r},\omega) &= \gamma_{nm}\nabla\times(\mathbf{r}\psi^{(l)}_{nm}(\mathbf{r},\omega))\\ &= \gamma_{nm} z^{(l)}_n(kr,\omega)\nabla\times[\mathbf{r}P^m_n(\cos\theta)\mathrm{e}^{\mathrm{i}m\phi}], \qquad (2.13)\\ \mathbf{N}^{(l)}_{nm}(\mathbf{r},\omega) &= \frac{1}{k}\nabla\times\mathbf{M}^{(l)}_{nm}(\mathbf{r},\omega)\\ &= \gamma_{nm}\frac{n(n+1)}{kr} z^{(l)}_n(kr,\omega)\frac{\mathbf{r}}{r}P^m_n(\cos\theta)\mathrm{e}^{\mathrm{i}m\phi}\\ &\quad+\frac{\gamma_{nm}}{kr}\frac{\mathrm{d}}{\mathrm{d}(kr)}\left(krz^{(l)}_n(kr,\omega)\right) r\nabla(P^m_n(\cos\theta)\mathrm{e}^{\mathrm{i}m\phi(\mathbf{r},\omega)}), \qquad (2.14)\end{aligned}$$

with the normalization factor

$$\gamma_{nm} = \sqrt{\frac{(2n+1)(n-m)!}{4\pi n(n+1)(n+m)!}}. \qquad (2.15)$$

Due to the use of the coordinate $\mathbf{r}$ as the guiding vector the functions $\mathbf{N}^{(l)}_{nm}(\mathbf{r},\omega)$ and $\mathbf{M}^{(l)}_{nm}(\mathbf{r},\omega)$ are now called vector spherical harmonic functions. They are now used for the expansion of the electromagnetic fields in the scattering problem.

Field decomposition

We continue by considering a sphere with radius r_s and material parameters $\varepsilon_\mathrm{s}(\omega)$ and $\mu_\mathrm{s}(\omega)$ that can be freely chosen. The sphere is surrounded by a homogeneous, isotropic medium. We decompose the total fields in the entire space into the field inside and outside the sphere. Then, the field outside the sphere, called the external field, is further decomposed into incident and scattered fields (Fig. 2.1)

$$\mathbf{E}_\mathrm{ext}(\mathbf{r},\omega) = \mathbf{E}_\mathrm{inc}(\mathbf{r},\omega) + \mathbf{E}_\mathrm{sca}(\mathbf{r},\omega). \qquad (2.16)$$

Note that this is always possible for theoretical considerations, but experimentally such a distinction is not possible.

As outlined before, we can expand each of these fields into vector spherical harmonic functions 2.13 and 2.14 with appropriate coefficients. The incident field has to be finite at the center of the coordinate system, thus, we take Bessel functions and the expansion reads

$$\mathbf{E}_\mathrm{inc}(\mathbf{r},\omega) = \sum_{n=1}^{\infty}\sum_{m=-n}^{n}\left[p_{nm}(\omega)\mathbf{N}^{(1)}_{nm}(\mathbf{r},\omega) + q_{nm}(\omega)\mathbf{M}^{(1)}_{nm}(\mathbf{r},\omega)\right]. \qquad (2.17)$$

Likewise, the internal field is expanded as

$$\mathbf{E}_\mathrm{int}(\mathbf{r},\omega) = \sum_{n=1}^{\infty}\sum_{m=-n}^{n}\left[c_{nm}(\omega)\mathbf{N}^{(1)}_{nm}(\mathbf{r},\omega) + d_{nm}(\omega)\mathbf{M}^{(1)}_{nm}(\mathbf{r},\omega)\right]. \qquad (2.18)$$

The scattered field needs to satisfy the Sommerfeld radiation condition and is expanded with Hankel functions

$$\mathbf{E}_{\text{sca}}(\mathbf{r},\omega) = \sum_{n=1}^{\infty} \sum_{m=-n}^{n} \left[a_{nm}(\omega)\mathbf{N}_{nm}^{(3)}(\mathbf{r},\omega) + b_{nm}(\omega)\mathbf{M}_{nm}^{(3)}(\mathbf{r},\omega) \right]. \tag{2.19}$$

Here, $p_{nm}(\omega)$ and $q_{nm}(\omega)$ are the incident coefficients, $a_{nm}(\omega)$ and $b_{nm}(\omega)$ are the scattering coefficients, and $c_{nm}(\omega)$ and $d_{nm}(\omega)$ are the internal coefficients.

The task is now to calculate the scattering (and, if required, the internal) coefficients for given incident coefficients. In general, this linear connection is given by the transfer or T-matrix defined as

$$\begin{pmatrix} \mathbf{a}(\omega) \\ \mathbf{b}(\omega) \end{pmatrix} = \mathbf{T}(\omega) \cdot \begin{pmatrix} \mathbf{p}(\omega) \\ \mathbf{q}(\omega) \end{pmatrix}. \tag{2.20}$$

Here, $\mathbf{a}(\omega)$, $\mathbf{b}(\omega)$, $\mathbf{p}(\omega)$, and $\mathbf{q}(\omega)$ are vectors that contain the scattering and incident coefficients, respectively. A similar matrix can be used to obtain the internal coefficients. However, this is beyond the scope of this thesis. We investigate the T-matrix in more detail in chapter 4. For now, it is sufficient to consider the Mie coefficients $a_n(\omega)$ and $b_n(\omega)$ that form the T-matrix of a sphere as a diagonal matrix

$$\begin{aligned} a_{nm}(\omega) &= a_n(\omega)p_{nm}(\omega) \\ b_{nm}(\omega) &= b_n(\omega)q_{nm}(\omega). \end{aligned} \tag{2.21}$$

With the interface conditions for the electromagnetic fields on the surface of the sphere

$$(\mathbf{E}_{\text{inc}}(\omega) + \mathbf{E}_{\text{sca}}(\omega) - \mathbf{E}_{\text{int}}(\omega)) \times \mathbf{r} = (\mathbf{H}_{\text{inc}}(\omega) + \mathbf{H}_{\text{sca}}(\omega) - \mathbf{H}_{\text{int}}(\omega)) \times \mathbf{r} = 0 \tag{2.22}$$

we can derive expressions for the Mie coefficients [61]

$$a_n(\omega) = \frac{m^2e^2 j_n(ekr_{\text{s}},\omega)[kr_{\text{s}}\, j_n(kr_{\text{s}},\omega)]' - m^2 j_n(kr_{\text{s}},\omega)[ekr_{\text{s}}\, j_n(ekr_{\text{s}},\omega)]'}{m^2e^2 j_n(ekr_{\text{s}},\omega)[kr_{\text{s}}\, h_n^{(1)}(kr_{\text{s}},\omega)]' - h_n^{(1)}(kr_{\text{s}},\omega)[ekr_{\text{s}}\, j_n(ekr_{\text{s}},\omega)]'} \tag{2.23}$$

$$b_n(\omega) = \frac{j_n(ekr_{\text{s}},\omega)[kr_{\text{s}}\, j_n(kr_{\text{s}},\omega)]' - m^2 j_n(kr_{\text{s}},\omega)[ekr_{\text{s}}\, j_n(ekr_{\text{s}},\omega)]'}{j_n(ekr_{\text{s}},\omega)[kr_{\text{s}}\, h_n^{(1)}(kr_{\text{s}},\omega)]' - m^2 h_n^{(1)}(kr_{\text{s}},\omega)[ekr_{\text{s}}\, j_n(ekr_{\text{s}},\omega)]'} \tag{2.24}$$

with $e = \sqrt{\frac{\varepsilon_{\text{b}}}{\varepsilon_{\text{s}}}}$, $m = \sqrt{\frac{\mu_{\text{b}}}{\mu_{\text{s}}}}$, where ε_{b} and μ_{b} are the permittivity and permeability of the surrounding medium, respectively. The dash represents a derivative with respect to the first argument of the function. The Mie coefficients can then be used to calculate the scattering coefficients for any given illumination coefficients.

Now that we have obtained the scattering coefficients, we can use them to calculate quantities in the near field and observable quantities in the far field. The total scattering, extinction, and absorption cross section are given as [62]

$$C_{\text{sca}}(\omega) = \eta \sum_{n=1}^{\infty} \sum_{m=-n}^{n} \left(|a_{nm}(\omega)|^2 + |b_{nm}(\omega)|^2 \right), \tag{2.25}$$

$$C_{\text{ext}}(\omega) = \eta \sum_{n=1}^{\infty} \sum_{m=-n}^{n} \text{Re}(p_{nm}(\omega)a_{nm}^*(\omega) + q_{nm}b_{nm}^*(\omega)), \tag{2.26}$$

$$C_{\text{abs}}(\omega) = C_{\text{ext}}(\omega) - C_{\text{sca}}(\omega). \tag{2.27}$$

Here, η is a scaling factor, depending on the illumination. For a plane wave we have $\eta = \frac{1}{k^2|\mathbf{E}_0|^2}$, where $\mathbf{E}_0$ is the amplitude of the incident plane wave.

To get more information about how this cross section is composed, we can modify the equations to calculate the contributions of each multipolar order by considering only the relevant coefficients

$$C_{\text{sca}}^{(n)}(\omega) = \eta \sum_{m=-n}^{n} |f_{nm}(\omega)|^2, \tag{2.28}$$

where n is the multipolar index which we want to investigate and $f_{nm}(\omega)$ stands for $a_{nm}(\omega)$ if we want to consider the electric part or $b_{nm}(\omega)$ if we consider the magnetic part, respectively. For example, the electric and magnetic dipole contributions, which are dominant for electromagnetically small particles, read

$$\begin{aligned} C_{\text{sca}}^{\text{el.dip.}}(\omega) &= \eta \left(|a_{1-1}(\omega)|^2 + |a_{10}(\omega)|^2 + |a_{11}(\omega)|^2\right) \\ C_{\text{sca}}^{\text{magn.dip.}}(\omega) &= \eta \left(|b_{1-1}(\omega)|^2 + |b_{10}(\omega)|^2 + |b_{11}(\omega)|^2\right). \end{aligned} \tag{2.29}$$

This means, if we know the scattering coefficients of an object with the corresponding illumination, we know exactly how different multipoles contribute to the total scattering. That is particularly valuable if we want to design a specific multipole resonance of a nanoparticle or if we want to investigate a known resonance, for example from experimental measurements.

The infinite series of the expansions need to be truncated at a finite number $n = N$ for numerical calculations. This number is the multipole order that we take into account, $N = 1$ corresponding to dipoles, $N = 2$ to quadrupoles and so on. Thus, by choosing which maximum order we want to consider, we can strongly influence the computation time and final accuracy. An estimation for N to warrant a high accuracy for a single sphere is given by [61]

$$N = kr_{\text{s}} + 4(kr_{\text{s}})^{\frac{1}{3}} + 2. \tag{2.30}$$

Plane waves

As stated above, we can calculate the scattering coefficients of a sphere if we know the illumination coefficients $p_{nm}(\omega)$ and $q_{nm}(\omega)$. A very useful illumination scenario that can be used to approximate numerous real world scenarios is the plane wave.

We present the coefficients of the plane wave with a spatial dependency

$$\mathbf{E}_{\text{inc}}(\mathbf{r}) = \mathbf{E}_0 \mathrm{e}^{\mathrm{i}\mathbf{k}\cdot\mathbf{r}}, \tag{2.31}$$

with the constant amplitude vector that satisfies $\mathbf{E}_0 \cdot \mathbf{k} = 0$. The illumination coefficients $p_{nm}(\omega)$ and $q_{nm}(\omega)$ depend on the direction of k which is given through the angles θ and ϕ. The coefficients are given as [62]

$$p_{nm}(\omega) = 4\pi(-1)^m \, \mathrm{i}^n d_n \mathbf{E}_0 \cdot \mathbf{C}_{nm}(\theta)\mathrm{e}^{-\mathrm{i}m\phi}, \tag{2.32}$$

$$q_{nm}(\omega) = 4\pi(-1)^m \, \mathrm{i}^{n-1} d_n \mathbf{E}_0 \cdot \mathbf{B}_{nm}(\theta)\mathrm{e}^{-\mathrm{i}m\phi}. \tag{2.33}$$

Here, we use the following functions

$$d_n = \sqrt{\frac{2n+1}{4\pi n(n+1)}}, \tag{2.34}$$

$$\mathbf{B}_{nm}(\theta) = \hat{\boldsymbol{\theta}}\tau_{nm}(\theta) - \hat{\boldsymbol{\phi}}\mathrm{i}\pi_{nm}(\theta), \quad \mathbf{C}_{nm}(\theta) = -\hat{\boldsymbol{\theta}}\mathrm{i}\pi_{nm}(\theta) - \hat{\boldsymbol{\phi}}\tau_{nm}(\theta), \tag{2.35}$$

$$\pi_{nm}(\theta) = \frac{m}{\sin\theta} d^n_{0m}(\theta), \qquad \tau_{nm}(\theta) = \frac{\mathrm{d}}{\mathrm{d}\theta} d^n_{0m}(\theta), \tag{2.36}$$

where $\hat{\boldsymbol{\theta}}$ and $\hat{\boldsymbol{\phi}}$ are unit vectors in the respective directions and $d^n_{m\mu}(\theta)$ is the Wigner d-function which is given as

$$d^n_{m\mu}(\theta) = A^n_{m\mu}(1-\cos\theta)^{\frac{m-\mu}{2}}(1+\cos\theta)^{-\frac{m+\mu}{2}}\partial^{n-l}_{\cos\theta}\left[(1-\cos\theta)^{n-m}(1+\cos\theta)^{n+m}\right], \tag{2.37}$$

with the prefactor

$$A^n_{m\mu} = \frac{(-1)^{n-\mu}}{2^n}\sqrt{\frac{(n+\mu)!}{(n-m)!(n+m)!(n-\mu)!}}\,. \tag{2.38}$$

These incidence coefficients of a plane wave illumination can be used in Eq. 2.21 with the known Mie coefficients of a single sphere to obtain the scattering coefficients.

2.1.2 Scattering by a cluster of spheres

The case of a single sphere is a very important first step, but in most practical cases we will have multiple particles in close vicinity (in the order of a few nanometers) that will interact. This interaction is often the most interesting part to consider. Thus, we need a method to calculate not only the response of multiple spheres corresponding to the incident light, but also the interaction of all spheres with each other should be included. This is taken into account by an extension of the Mie scattering in a self consistent way [63]. The approach is called *multi Mie scattering method*.

In principle, the situation for each sphere in the cluster is the same as in the single sphere case. The fields relevant in the interaction with a specific sphere are again expanded into the vector spherical harmonic functions $\mathbf{N}^{(l)}_{nm}(\mathbf{r},\omega)$ and $\mathbf{M}^{(l)}_{nm}(\mathbf{r},\omega)$ in the coordinate system corresponding to the sphere j. We just add an index to the incident and scattering coefficients $p^j_{nm}(\omega)$, $q^j_{nm}(\omega)$ and $a^j_{nm}(\omega)$, $b^j_{nm}(\omega)$. However, the incident coefficients are actually very different from the single sphere case. In the cluster, not only the external incident light impinges on each sphere, but also the scattered light from all other spheres contained in the considered cluster. In the following, we describe how to deal with this situation.

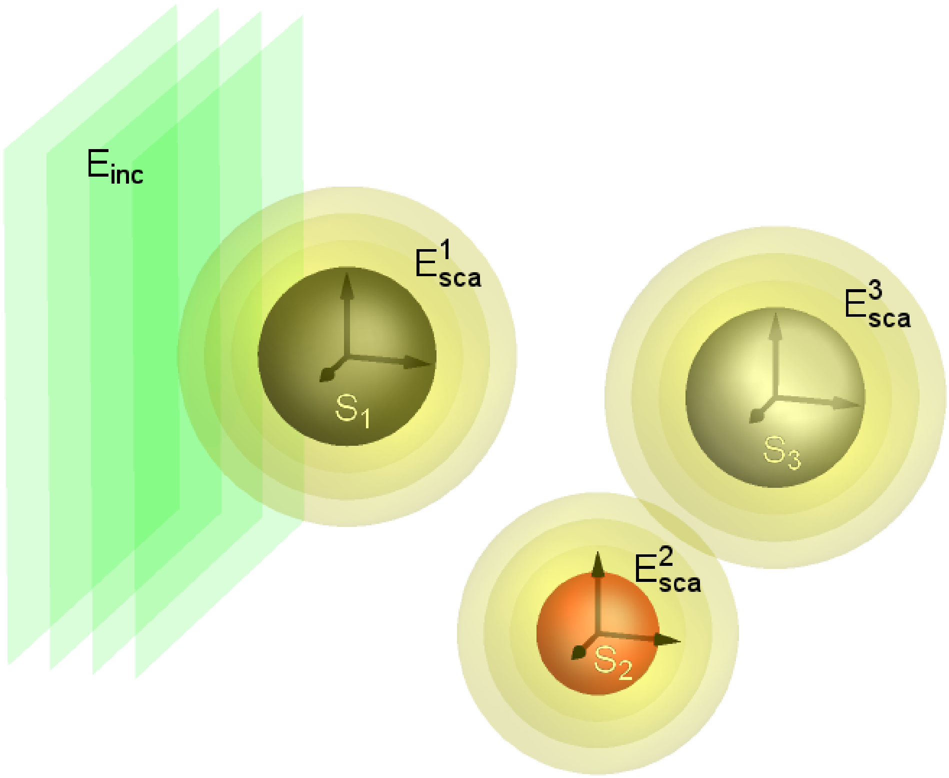

Figure 2.2: Schematic representation of a cluster of different spheres S_1, S_2, S_3 with corresponding local coordinate systems. These coordinate systems are positioned at the center of each sphere. The scattered field corresponding to each sphere is labeled accordingly.

Multiple scattering

To calculate the scattered fields of a cluster of J spheres as depicted in Fig. 2.2, we need to simultaneously take the scattering by all spheres into account. This is done by writing the incident field on each individual sphere as the sum of the external incident field and the scattered fields of all other spheres in the cluster. Then, the field impinging on sphere j is given as

$$\mathbf{E}^j_{\text{inc}}(\mathbf{r},\omega) = \mathbf{E}_{\text{inc}}(\mathbf{r},\omega) + \sum_{l\neq j} \mathbf{E}^{(l,j)}_{\text{sca}}(\mathbf{r},\omega). \tag{2.39}$$

Here, the superscript (l, j) denotes the transformation of the field from the coordinate system centered at the l^{th} sphere to the j^{th} sphere. This is done with the translational addition theorems applied to the vector spherical harmonics as [64, 65]

$$\begin{aligned}
\mathbf{N}^{(3)}_{nm}(\mathbf{r},\omega) &= \sum_{\nu=1}^{\infty}\sum_{\mu=-\nu}^{\nu}\left[A^{\nu\mu}_{nm}(\mathbf{d}_{lj},\omega)\mathbf{N}^{(1)}_{\nu\mu}(\mathbf{r},\omega) + B^{\nu\mu}_{nm}(\mathbf{d}_{lj},\omega)\mathbf{M}^{(1)}_{\nu\mu}(\mathbf{r},\omega)\right], \\
\mathbf{M}^{(3)}_{nm}(\mathbf{r},\omega) &= \sum_{\nu=1}^{\infty}\sum_{\mu=-\nu}^{\nu}\left[A^{\nu\mu}_{nm}(\mathbf{d}_{lj},\omega)\mathbf{M}^{(1)}_{\nu m'}(\mathbf{r},\omega) + B^{\nu\mu}_{nm}(\mathbf{d}_{lj},\omega)\mathbf{N}^{(1)}_{\nu\mu}(\mathbf{r},\omega)\right],
\end{aligned} \tag{2.40}$$

where we use the translation coefficients $A_{nm}^{\nu\mu}(\mathbf{d}_{lj},\omega)$ and $B_{nm}^{\nu\mu}(\mathbf{d}_{lj},\omega)$. The translation is quantified with the vector $\mathbf{d}_{lj}$, which points from the position of sphere l to the position of sphere j. A detailed definition of the translation coefficients is given in the appendix.

Now that we can express the scattered fields of several scatterers in different coordinate systems, we can form a system of equations that yields the scattering coefficients of each individual scatterer self-consistently. We consider the incident field coefficients for each sphere j

$$\begin{aligned} p_{nm}^{j}(\omega) &= p_{nm}^{j,j}(\omega) - \sum_{l\neq j}\sum_{\nu=1}^{\infty}\sum_{\mu=-\nu}^{\nu}\left[a_{\nu\mu}^{l}(\omega)A_{nm}^{\nu\mu}(\mathbf{d}_{lj},\omega) + b_{\nu\mu}^{l}(\omega)B_{nm}^{\nu\mu}(\mathbf{d}_{lj},\omega)\right], \\ q_{nm}^{j}(\omega) &= q_{nm}^{j,j}(\omega) - \sum_{l\neq j}\sum_{\nu=1}^{\infty}\sum_{\mu=-\nu}^{\nu}\left[a_{\nu\mu}^{l}(\omega)B_{nm}^{\nu\mu}(\mathbf{d}_{lj},\omega) + b_{\nu\mu}^{l}(\omega)A_{nm}^{\nu\mu}(\mathbf{d}_{lj},\omega)\right], \end{aligned} \tag{2.41}$$

where $p_{nm}^{j,j}(\omega)$ and $q_{nm}^{j,j}(\omega)$ are the original incident coefficients translated to the position of the particle. This translation is done by adding a phase, corresponding to the shift relative to the point of origin

$$p_{nm}^{j,j}(\omega) = \mathrm{e}^{\mathrm{i}\mathbf{k}\cdot\mathbf{d}_{0j}}p_{nm}(\omega), \quad q_{nm}^{j,j}(\omega) = \mathrm{e}^{\mathrm{i}\mathbf{k}\cdot\mathbf{d}_{0j}}q_{nm}(\omega). \tag{2.42}$$

The other terms appearing in Eq. 2.41 represent the scattered fields of all other particles incident on sphere j. Then we insert these incident coefficients into Eq. 2.21 and arrive at

$$\begin{aligned} a_{nm}^{j}(\omega) &= a_{n}^{j}(\omega)\left\{p_{nm}^{j,j}(\omega) - \sum_{l\neq j}\sum_{\nu=1}^{\infty}\sum_{\mu=-\nu}^{\nu}\left[a_{\nu\mu}^{l}(\omega)A_{nm}^{\nu\mu}(\mathbf{d}_{lj},\omega) + b_{\nu\mu}^{l}(\omega)B_{nm}^{\nu\mu}(\mathbf{d}_{lj},\omega)\right]\right\}, \\ b_{nm}^{j}(\omega) &= b_{n}^{j}(\omega)\left\{q_{nm}^{j,j}(\omega) - \sum_{l\neq j}\sum_{\nu=1}^{\infty}\sum_{\mu=-\nu}^{\nu}\left[a_{\nu\mu}^{l}(\omega)B_{nm}^{\nu\mu}(\mathbf{d}_{lj},\omega) + b_{\nu\mu}^{l}(\omega)A_{nm}^{\nu\mu}(\mathbf{d}_{lj},\omega)\right]\right\}, \end{aligned} \tag{2.43}$$

a system of equations for the scattering coefficients $a_{nm}^{j}(\omega)$ and $b_{nm}^{j}(\omega)$ with known Mie and incident coefficients. The Mie coefficients $a_{n}^{j}(\omega)$ and $b_{n}^{j}(\omega)$ also have indices j because the spheres can all be different.

Like before, the infinite series are truncated at a finite number N for numerical calculations. The estimate for single spheres in Eq. 2.30 can serve as a guideline, but due to the coupling of close spheres and the inclusion of addition coefficients, a higher number might be required.

Collective scattering

Finally, the scattering coefficients of the entire cluster can be calculated instead of those of each individual sphere. These coefficients explain how the cluster scatters light as a combined object. The individual scattering coefficients $a_{nm}^{j}(\omega)$ and $b_{nm}^{j}(\omega)$

are defined in each individual coordinate system. They need to be transformed to a common central coordinate system, where we can add them together to obtain the total coefficients

$$a_{nm}(\omega) = \sum_{j=1}^{J} \sum_{\nu=1}^{\infty} \sum_{\mu=-\nu}^{\nu} \left[a^{j}_{\nu\mu}(\omega) A^{\nu\mu}_{nm}(\mathbf{d}_{j0}, \omega) + b^{j}_{\nu\mu}(\omega) B^{\nu\mu}_{nm}(\mathbf{d}_{j0}, \omega) \right] ,$$

$$b_{nm}(\omega) = \sum_{j=1}^{J} \sum_{\nu=1}^{\infty} \sum_{\mu=-\nu}^{\nu} \left[a^{j}_{\nu\mu}(\omega) B^{\nu\mu}_{nm}(\mathbf{d}_{j0}, \omega) + b^{j}_{\nu\mu}(\omega) A^{\nu\mu}_{nm}(\mathbf{d}_{j0}, \omega) \right] , \tag{2.44}$$

where $\mathbf{d}_{j0}$ represents the translation to the central coordinate system. We need to take care to choose the correct translation coefficients corresponding to spherical Bessel or Hankel functions as indicated in Eqs. A.1 and A.2 in the appendix. From the scattering coefficients we can calculate again the total scattering cross section as it was done in the case of a single sphere in Eq. 2.25.

Similarly, we can obtain the total scattered field by computing the scattered field of each sphere individually from the scattering coefficients and superimposing the fields.

2.2 Light propagation in homogenized materials

Usually, self-assembled metamaterials are composed of particles that are arranged in a three dimensional space ,where they form an actual bulk material, or in a two dimensional fashion, where they form a thin film, also called metasurface. The arrangement of these particles typically has no long-range order due to the nature of the self-assembly process. Now, suppose we know the electromagnetic properties of the individual particles, for example due to a multipole analysis, it is still a challenging task to know the properties of the composite material.

How will the final assembly interact with light and how will the embedding material influence the optical response? These questions can be answered within an effective medium theory, where the composite material is treated as a homogeneous medium with effective properties. The process of identifying the effective properties of a metamaterial is known as homogenization. In the process of this homogenization, some assumptions must be made. The most important restriction concerns the size of the particles. In particular, the particles must be small compared to the wavelength and to the average distance of the particles. In other words: we are considering a low concentration. Otherwise, higher order multipole moments and the coupling between multiple particles need to be taken into account. This would require much more sophisticated homogenization techniques which are not considered here.

In the following, we want to outline two homogenization methods. For this purpose we study exemplarily a scattering structure that consists of a dielectric core sphere covered with a shell consisting of silver ellipsoids, as depicted in Fig. 2.3. Each ellipsoid is characterized by the major axis a_1 and minor axes $a_2 = a_3$. In the following, we take this example to demonstrate different strategies to homogenize

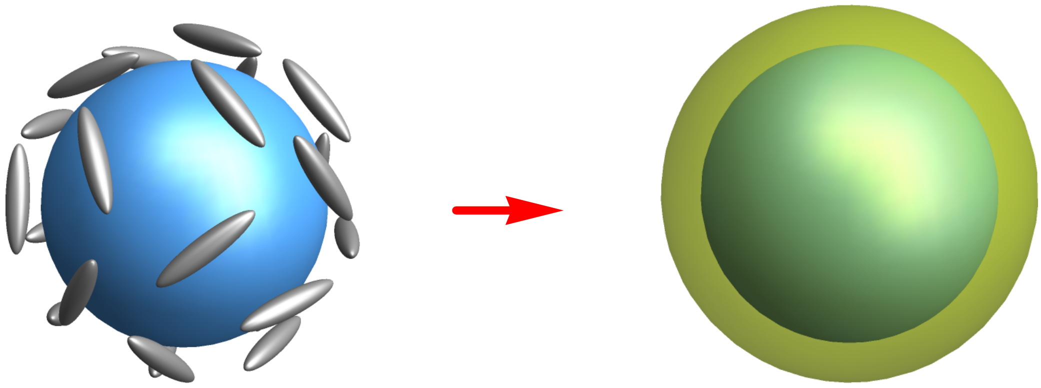

Figure 2.3: Scattering cancellation structure as an example for homogenization. The left picture shows the actual structure composed of a central sphere with silver ellipsoids on top. On the right hand side we see the homogenized object, where the fine details of the ellipsoids are hidden in an effective shell.

the shell material. This example is particularly interesting, because it constitutes a scattering cancellation structure. The technique relies on covering the object of interest with a shell that scatters light into a far field of equal strength as the light scattered by the object object, but with a phase shift of π. The resulting destructive interference prohibits the detection of the entire object in measurements that probe the scattered light.

Such a scattering cancellation structure is of great interest in the recent nanooptics research. Hiding micro- or nanoscopic objects from electromagnetic detection proves useful in a multitude of applications, such as reducing the scattering from a near field scanning optical microscope tip. Here we introduce the theoretical basis for the scattering cancellation structure. The concept is further investigated in section 5.1.

In a first approach, the shell is treated as a thin metasurface to which we can attribute a surface reactance. After that, we show a different method that is better suited for three dimensional materials. A volumetric homogenization with the Clausius-Mossotti relation, is performed. The shell is homogenized and described by the effective material properties $\varepsilon_{\text{eff}}(\omega)$ and $\mu_{\text{eff}}(\omega)$.

2.2.1 Surface homogenization

Surface homogenization can be very useful for treating a thin layer as an interface. Then, we do not need to consider the electromagnetic fields inside the layer which can have a very complicated form. Instead, the layer is described by the effective surface reactance, which we introduce in the following.

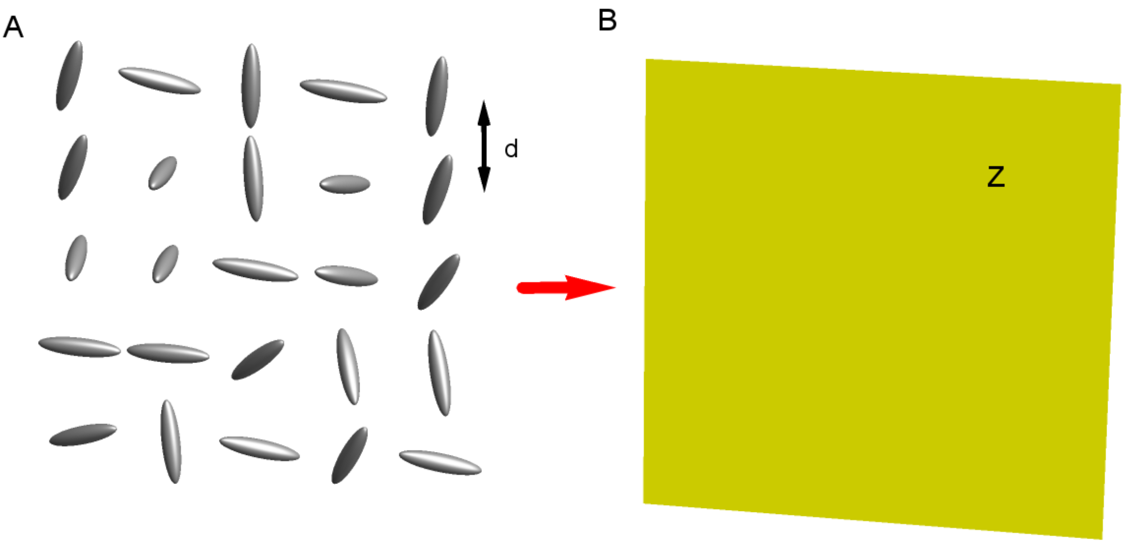

Figure 2.4: (A) Array of particles with nearest neighbor distance d. (B) Effective surface with impedance $Z(\omega)$.

Surface reactance

We consider a square array of small particles that is infinitely extended in two dimensions and has a lattice constant d, as shown in Fig. 2.4. The particles could be spheres or ellipsoids, as shown in the figure, but also more complicated particles with known polarizability tensor $\boldsymbol{\alpha}(\omega)$. To satisfy the dipole approximation, the particles have to be much smaller than the wavelength of the incoming field.

The polarizability relates the local electric field to the induced dipole moment

$$\mathbf{p}(\mathbf{r},\omega) = \varepsilon_0 \boldsymbol{\alpha}(\omega) \mathbf{E}_{\text{loc}}(\mathbf{r},\omega), \tag{2.45}$$

where ε_0 is the vacuum permittivity. The local field is the sum of the incident field and the interaction field. This interaction field is related to the dipole moment by the interaction constant $\beta(\omega)$ like

$$\mathbf{E}_{\text{loc}}(\mathbf{r},\omega) = \mathbf{E}_{\text{inc}}(\mathbf{r},\omega) + \mathbf{E}_{\text{int}}(\mathbf{r},\omega) = \mathbf{E}_{\text{inc}}(\mathbf{r},\omega) + \frac{\beta(\omega)}{\varepsilon_0}\mathbf{p}(\mathbf{r},\omega). \tag{2.46}$$

The interaction constant expresses the interaction of the dipoles in the lattice. It can be approximately determined for a plane wave illumination to be [66]

$$\beta(\omega) = \frac{(1 - \mathrm{i}kR_0)^2}{d^2 4 R_0}, \tag{2.47}$$

where $R_0 = d/1.438$. Then, after calculating the average surface currents

$$J(\mathbf{r},\omega) = \frac{-\mathrm{i}\omega|\mathbf{p}(\mathbf{r},\omega)|}{d^2}, \tag{2.48}$$

we can attribute an effective impedance $Z(\omega)$ to the surface. This impedance is generally defined by

$$E_{\perp}(\mathbf{r},\omega) = Z(\omega)J(\mathbf{r},\omega), \tag{2.49}$$

where $E_{\perp}(\mathbf{r},\omega)$ is the field perpendicular to the surface. The impedance of the lattice is given as [67]

$$Z(\omega) = R(\omega) - \mathrm{i}X(\omega) = \mathrm{i}\frac{d^2}{k}\left(\frac{1}{\alpha(\omega)} - \beta(\omega)\right) - \frac{1}{2}, \tag{2.50}$$

where we use an averaged polarizability α. The real part of the impedance is the resistive component $R(\omega)$. The imaginary part corresponds to the effective surface reactance $X(\omega)$

$$X(\omega) = -\frac{d^2}{k}\mathrm{Re}\left[\frac{1}{\alpha(\omega)} - \beta(\omega)\right]. \tag{2.51}$$

If we know the effective surface reactance of the lattice, we can treat it as a homogeneous layer with the appropriate properties. This simplifies the description and calculation of the optical properties of the array.

Polarizability

In order to perform the surface homogenization for the previously described example with ellipsoidal particles, we need to know the polarizabilities of the particles in the array. Let us consider an array of arbitrarily oriented ellipsoids as shown in Fig. 2.4 A. The polarizability of an ellipsoid along the long axis a_1 can be expressed analytically [61]

$$\alpha_1(\omega) = \frac{\varepsilon_{\mathrm{p}}(\omega) - \varepsilon_{\mathrm{b}}(\omega)}{\varepsilon_{\mathrm{b}}(\omega) + N_1(\varepsilon_{\mathrm{p}}(\omega) - \varepsilon_{\mathrm{b}}(\omega))}. \tag{2.52}$$

Here, $\varepsilon_{\mathrm{p}}(\omega)$ is the relative permittivity of the ellipsoid, $\varepsilon_{\mathrm{b}}(\omega) = 1$ is the relative permittivity of the host medium, in our case vacuum, and

$$N_1 = \frac{a_1 a_2^2}{2}\int_0^{\infty} \frac{\mathrm{d}s}{(s+a_1^2)\sqrt{(s+a_1^2)(s+a_2^2)(s+a_3^2)}} \tag{2.53}$$

is the depolarization factor of the ellipsoid along the major axis. Note that it depends on the length of the semi axes and, therefore, implicitly on the aspect ratio $\delta = a_1/a_2$ of the ellipsoid. A similar expression is found for the minor axis a_2. To account for the disorder of the particles, we perform a first order approximation and calculate an average polarizability from the three components α_1 and $\alpha_2 = \alpha_3$. This is reasonable, because ultimately, the layer will not be flat. Thus, all orientations of ellipsoids are possible.

Now that we know the polarizabilities of the constituting particles, we can investigate how the layer will interact with an incident plane wave. This is done by considering the surface reactance as introduced in Eq. 2.51.

Scattering cancellation by a surface

We consider a sphere which is covered with the artificial metasurface. The scattering by a dipolar particle that is covered by a reactive layer can be suppressed if the surface reactance takes specific values.

To minimize the scattering by the object, the first order scattering coefficient needs to be suppressed. This is sufficient, because we are in the dipolar regime, where the scattering by the core sphere is well described by the first order terms. The Mie scattering solution of a coated sphere shows that the following determinant has to be minimized in order to minimize the scattering contribution, corresponding to the spherical harmonic functions with index $n = 1$ [68]

$$\begin{vmatrix} j_n(k_\mathrm{s} r_\mathrm{s}) & j_n(k r_\mathrm{s}) & y_n(k r_\mathrm{s}) & 0 \\ [k_\mathrm{s} r_\mathrm{s} j_n(k_\mathrm{s} r_\mathrm{s})]'/\varepsilon_\mathrm{s} & [k r_\mathrm{s} j_n(k r_\mathrm{s})]' & [k r_\mathrm{s} y_n(k r_\mathrm{s})]' & 0 \\ 0 & j_n(k r_\mathrm{c}) + \frac{[k r_\mathrm{c} j_n(k r_\mathrm{c})]'}{(\mathrm{i}\omega\varepsilon_0 r_\mathrm{c} Z)} & y_n(k r_\mathrm{c}) + \frac{[k r_\mathrm{c} y_n(k r_\mathrm{c})]}{(\mathrm{i}\omega\varepsilon_0 r_\mathrm{c} Z)} & j_n(k r_\mathrm{c}) \\ 0 & [k r_\mathrm{c} j_n(k r_\mathrm{c})]' & [k r_\mathrm{c} y_n(k r_\mathrm{c})]' & [k r_\mathrm{c} j_n(k r_\mathrm{c})]' \end{vmatrix}, \tag{2.54}$$

where r_s is the radius of the core sphere, r_c is the radius of the scattering cancellation mantle, k is the wave number in the surrounding medium, and k_s is the wave number inside the sphere. Note that, even though the modeled layer is infinitely thin, it does not have to reside directly on the surface of the sphere.

It follows that the surface reactance necessary to suppress the scattering response in dipole approximation from a spherical core object has to be

$$X_\mathrm{s}^\mathrm{ideal}(\omega) = \frac{2[2 + \varepsilon_\mathrm{s}(\omega) - \gamma^3(\varepsilon_\mathrm{s}(\omega) - 1)]}{3\frac{\omega_\mathrm{c}}{c} r_\mathrm{s} \gamma^3(\varepsilon_\mathrm{s}(\omega) - 1)}\,, \tag{2.55}$$

where ω_c is the desired operational frequency, $\varepsilon_\mathrm{s}(\omega)$ is the relative permittivity of the core sphere, and $\gamma = r_\mathrm{s}/r_\mathrm{c}$.

As we have seen in Eq. 2.51, the surface reactance strongly depends on the polarizabilities of the constituent particles. This suggests that we can tune the reactance to the value necessary for the condition to reduce the scattering by changing the polarizability of the particles in the shell. This is indeed quite easy to implement, when choosing plasmonic ellipsoids. Their polarizability can be modified just by adjusting the length of the major and minor axes. The polarizability is given according to Eq. 2.52.

To showcase this tunability, we present an example. We consider a dielectric sphere with a nondispersive permittivity of $\varepsilon_\mathrm{s} = 2.1$ and a radius of $r_\mathrm{s} = 61$ nm. We take silver ellipsoids with tabulated experimental material data [69] and different aspect ratios $\delta = a_1/a_2$ $\left(\frac{16\mathrm{nm}}{6\mathrm{nm}}, \frac{23\mathrm{nm}}{5\mathrm{nm}}, \text{ and } \frac{36\mathrm{nm}}{4\mathrm{nm}}\right)$ as the coating building blocks. The ellipsoids are prolate, hence, the component of the polarizability corresponding to the short axes are the same. The ellipsoids are arranged around the core at a radius of $r_\mathrm{c} = 76$ nm, see section 5.1 for more details and numerical simulations.

First, we calculate the ideal surface reactance that is necessary to suppress the scattering by the core sphere at each frequency, as shown in Fig. 2.5. Next, we show

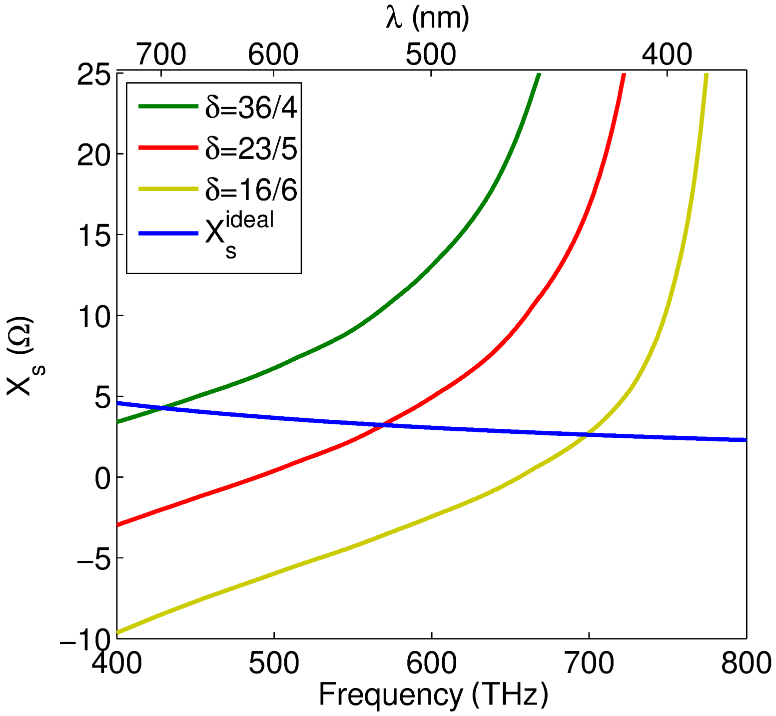

Figure 2.5: Surface reactance for different aspect ratios $\delta = a_z/a_x$ of the constituting ellipsoids and the ideal surface reactance that is required to cancel the scattering. Spectral positions where both surface reactances are equal correspond to the operational frequencies for different aspect ratios.

the effective surface reactance of the layer made of selected ellipsoids and compare it to the desired reactance. We obtain different frequencies, depending on the axis ratio, where the calculated effective reactance matches the ideal reactance. The scattering of the structure will be suppressed at these frequencies. The larger the aspect ratio of the ellipsoids, the further the resonance gets redshifted.

These are promising results, because the operating frequency can be tuned across the entire visible spectrum. This is further investigated in the next section by applying also a volumetric homogenization and in more detail later in section 5.1 with numerical calculations, where the results of the theoretical approach are confirmed.

2.2.2 Volumetric homogenization

Clausius-Mossotti relation

In this section, we consider a three dimensional medium composed of a host material and small inclusions. Such a composite medium shall be described as a bulk homogeneous material and we assign an effective permittivity and permeability to it. The inclusions are again only characterized by their polarizabilities and we describe them in the electric dipole approximation.

We start from the Lorenz-Lorentz formula

$$\mathbf{E}_{\text{loc}}(\mathbf{r},\omega) = \mathbf{E}(\mathbf{r},\omega) + \frac{\mathbf{P}(\mathbf{r},\omega)}{3\varepsilon_0}. \tag{2.56}$$

This equation connects the local field sensed by the particles with the averaged macroscopic field $\mathbf{E}(\mathbf{r},\omega)$ through the polarization $\mathbf{P}(\mathbf{r},\omega)$. Using Eq. 2.45, we can write the average polarization as [66]

$$\mathbf{P}(\mathbf{r},\omega) = \rho\mathbf{p}(\mathbf{r},\omega) = \rho\alpha(\omega)\mathbf{E}_{\text{loc}}(\mathbf{r},\omega) = \frac{\rho\alpha(\omega)}{1-\frac{\rho\alpha(\omega)}{3\varepsilon_0}}\mathbf{E}(\mathbf{r},\omega), \tag{2.57}$$

where $\rho = 1/V$ is the volume concentration of the particles. Using the electric displacement, which is defined as

$$\mathbf{D}(\mathbf{r},\omega) = \varepsilon_0\mathbf{E}(\mathbf{r},\omega) + \mathbf{P}(\mathbf{r},\omega) = \varepsilon_{\text{eff}}(\omega)\mathbf{E}(\mathbf{r},\omega), \tag{2.58}$$

the effective permittivity can be calculated as [66]

$$\varepsilon_{\text{eff}}(\omega) = \varepsilon_0\frac{3+2N\alpha(\omega)}{3-N\alpha(\omega)}. \tag{2.59}$$

This equation is known as the Clausius-Mossotti formula and expresses the effective permittivity of a medium made from polarizable particles with a given concentration. A similar equation can be found analogously for the permeability

$$\mu_{\text{eff}}(\omega) = \mu_0\frac{3+2N\alpha_{\text{m}}(\omega)}{3-N\alpha_{\text{m}}(\omega)}, \tag{2.60}$$

where $\alpha_{\text{m}}(\omega)$ is the magnetic polarization.

Now, we consider again our example with the dielectric core covered by a shell made from metallic ellipsoids. Because the shell actually has a finite thickness, it is reasonable to apply the volumetric homogenization to the shell material. Then, we treat the system as a sphere covered with a shell. We choose the density ρ in the shell corresponding to the distance in the previous section. This density depends on the size of the ellipsoids and the distance d, as introduced in the previous section. The effective permittivity of a material made out of silver ellipsoids with the axes $a_1 = 23$ nm and $a_2 = a_3 = 5$ nm in vacuum shows a strong resonance at 500 THz, as seen in Fig. 2.6. Again, we take the average of the three polarizabilities to account for the random orientation.

As will become clearer in the next paragraph, we are not directly interested in the resonance itself. Actually, we want to operate as far away from it as possible, because the large imaginary part causes strong absorption, which potentially destroys most of the interesting effects.

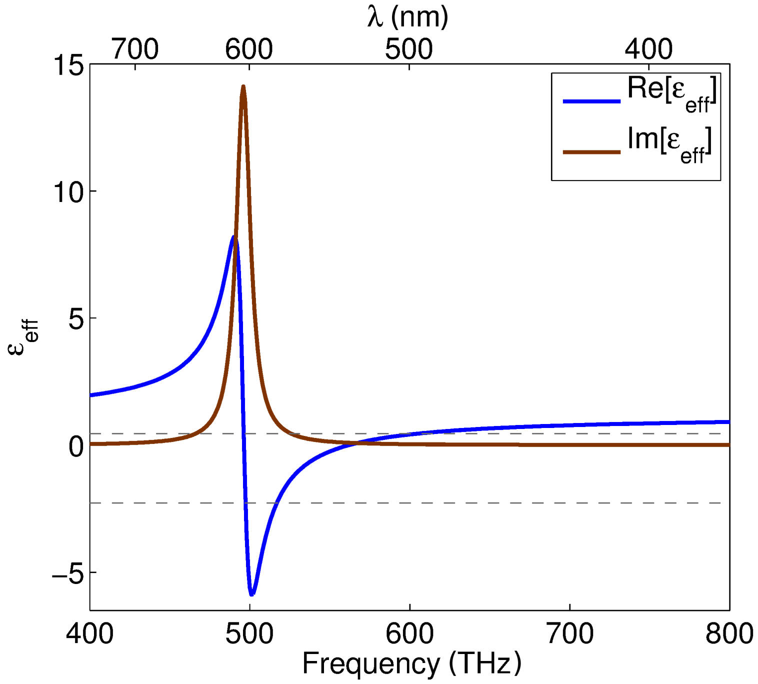

Figure 2.6: Effective relative permittivity of a material made of silver ellipsoids with semi axes $a_1 = 23$ nm and $a_2 = a_3 = 5$ nm. The dashed lines show the solutions of Eq. 2.63.

Scattering suppression of a core-shell particle

Now, we calculate the polarizability of the entire particle analytically, by considering a sphere covered with a shell made out of the homogenized material with effective permittivity. The polarizability of such an object is given by [70]

$$\alpha_{\text{c}}(\omega) = 3\frac{[\varepsilon_{\text{eff}}(\omega) - \varepsilon_{\text{b}}][\varepsilon_{\text{s}} + 2\varepsilon_{\text{eff}}(\omega)] + \gamma^3[2\varepsilon_{\text{eff}}(\omega) + \varepsilon_{\text{b}}][\varepsilon_{\text{s}} - \varepsilon_{\text{eff}}(\omega)]}{[\varepsilon_{\text{eff}}(\omega) + 2\varepsilon_{\text{b}}][\varepsilon_{\text{s}} + 2\varepsilon_{\text{eff}}(\omega)] + 2\gamma^3[\varepsilon_{\text{eff}}(\omega) - \varepsilon_{\text{b}}][\varepsilon_{\text{s}} - \varepsilon_{\text{eff}}(\omega)]} . \tag{2.61}$$

From this polarizability we can also calculate the total scattering cross section [61]

$$C_{\text{sca}}(\omega) = k^4 r_{\text{c}}^6 8\pi |\alpha_{\text{c}}(\omega)|^2 . \tag{2.62}$$

To suppress the scattering response of a sphere with a shell we need to satisfy the following condition [71]

$$\gamma^3 = \frac{[\varepsilon_{\text{eff}}(\omega) - \varepsilon_{\text{b}}][2\varepsilon_{\text{eff}}(\omega) + \varepsilon_{\text{s}}]}{[\varepsilon_{\text{eff}}(\omega) - \varepsilon_{\text{s}}][2\varepsilon_{\text{eff}}(\omega) + \varepsilon_{\text{b}}]} , \tag{2.63}$$

which is obtained by setting the nominator of Eq. 2.61 equal to zero.

We notice that this equation delivers real valued solutions for the effective permittivity of the shell material, if ε_{s} and ε_{b} are real. However, because the shell is composed of metallic particles, or can be completely arbitrary in general, we can also expect complex values. The condition restricts therefore only the real part of $\varepsilon_{\text{eff}}(\omega)$.

For the present case, Eq. 2.63 possesses two solutions, a positive one, $\mathrm{Re}[\varepsilon_{\text{eff}}(\omega_1)] = 0.46$, and a negative one, $\mathrm{Re}[\varepsilon_{\text{eff}}(\omega_2)] = -2.28$, shown as dashed lines in Fig. 2.6. The scattering cross section of the core-shell object will be reduced at the frequencies where the real part of $\varepsilon_{\text{eff}}(\omega)$ takes these values. The remaining imaginary part will introduce absorption and additional scattering losses [72] and, therefore, diminish the anticipated effect.

As expected, the scattering cross section of the core-shell sphere shows multiple local minima (red line in Fig. 2.7). The peak (superimposed with a dip) is caused by the plasmon resonance of the metallic particles. The two minima are attributed to the frequencies where $\varepsilon_{\text{eff}}(\omega)$ attains values that correspond to a solution of the scattering cancellation condition Eq. 2.63. Additional possible minima that would occur close to the resonance frequency of the plasmon resonance are not observed, even though there are more solutions directly at the resonance of $\varepsilon_{\text{eff}}(\omega)$ at 500 THz. This solution close to the resonance is not observed, because the rather large imaginary part of the effective permittivity in the resonance destroys the effect of scattering cancellation. As we see in section 5.1, also the minimum corresponding to the negative solution will be suppressed in numerical calculations due to the high losses.

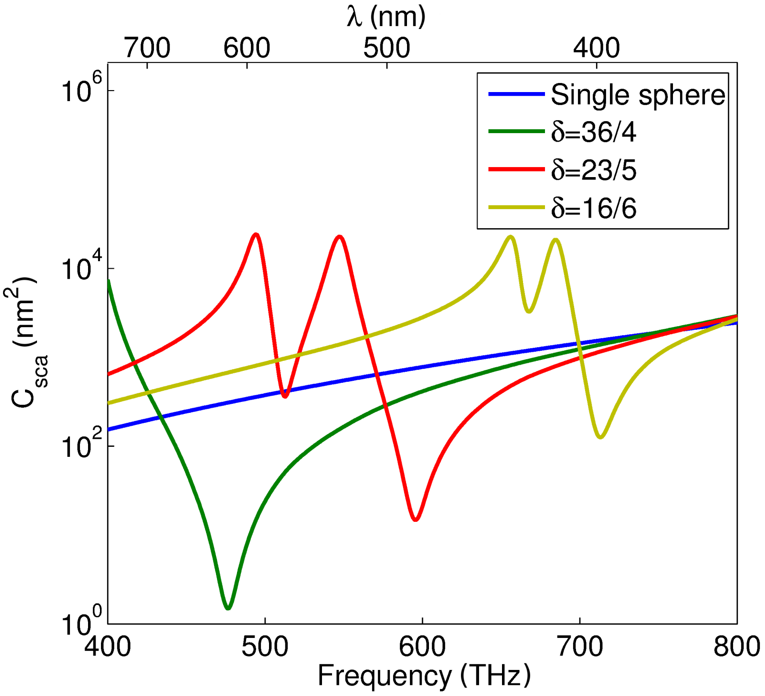

Figure 2.7: Scattering cross section of a single bare dielectric sphere with $\varepsilon_s = 2.1$ (blue) and the same sphere covered with a shell made from a medium that consists of silver ellipsoids with different axis ratios at a fixed density (green, red, and yellow).

We also see in Fig. 2.7 that the spectral position, where the scattering cross section is suppressed, depends again sensitively on the aspect ratio of the constituting ellipsoids. In fact, the operating frequency can be tuned across the visual spectrum by shifting the resonance by tuning the axis ratio. The spectral position is shifted, but the qualitative behavior of the scattering cross section is very similar.

If we compare the frequency where the scattering is maximally reduced to the positions obtained from the surface homogenization technique, we notice an excellent agreement for the respective aspect ratios.

Interestingly, the volumetric homogenization is applicable even though there is only one layer of particles enclosing the core sphere. Clearly, Eq. 2.59 is strictly valid only in extended three dimensional materials. However, it has been shown that the approach is also valid for very thin materials [73]. Additionally, we show numerical simulations for this case in section 5.1 to prove that these considerations are justified.

2.3 Duality and helicity

A very interesting property of artificial materials is chirality. The lack of mirror symmetries of scattering objects causes a different response for right handed and left handed circularly polarized light, respectively. But geometrical symmetry or asymmetry is not the only deciding aspect. The electromagnetic duality of a scatterer is something that is often neglected in recent studies. Here, we introduce the basic concepts of duality symmetry and helicity of light. These concepts are used in chapter 5 to describe electromagnetic chirality of scattering objects.

As we know from Noether's theorem, every invariant property or symmetry comes with a corresponding conserved quantity. It is easy to show that Maxwell's equations in a homogeneous medium are invariant under the transformation [74]

$$\mathbf{E}'(\mathbf{r},\omega) = \cos\theta\,\mathbf{E}(\mathbf{r},\omega) - Z(\omega)\sin\theta\,\mathbf{H}(\mathbf{r},\omega)\;, \tag{2.64}$$

$$\mathbf{H}'(\mathbf{r},\omega) = \cos\theta\,\mathbf{H}(\mathbf{r},\omega) + \frac{\sin\theta}{Z(\omega)}\,\mathbf{E}(\mathbf{r},\omega)\;, \tag{2.65}$$

where $Z(\omega)$ is the impedance and θ is an arbitrary constant angle. Special cases of this transformation, for example $\mathbf{E}'(\mathbf{r},\omega) = -\mathbf{E}(\mathbf{r},\omega)$, $\mathbf{H}'(\mathbf{r},\omega) = -\mathbf{H}(\mathbf{r},\omega)$ for $\theta = \pi$ are well known.

The corresponding conservation law is the conservation of helicity. The quantity of helicity is defined as the projection of the total angular momentum onto the direction of the linear momentum of the wave [75]

$$\Lambda = \frac{\mathbf{J}\cdot\mathbf{P}}{|\mathbf{P}|}. \tag{2.66}$$

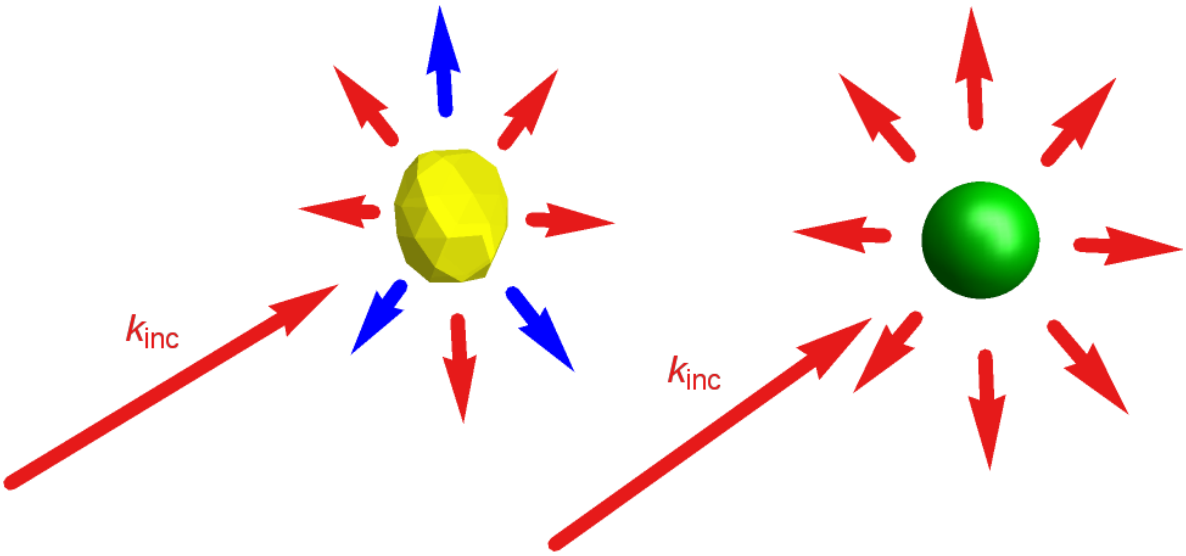

Figure 2.8: Schematic representation of the scattering by a general, non-dual object (yellow) and a dual sphere (green). The red and blue arrows represent waves of specific helicity, respectively. Under illumination with a pure helicity (red), where $\mathbf{k}_{\mathrm{inc}}$ is the incidence wave vector, the dual sphere preserves the helicity, while the other object produces also fields of the opposite helicity (blue).

The operator has the two eigenvalues 1 and -1, and the corresponding eigenstates [76]

$$\mathbf{G}_{\pm}(\mathbf{r},\omega) = \frac{1}{\sqrt{2}}\left[\mathbf{E}(\mathbf{r},\omega) \pm \mathrm{i}Z\mathbf{H}(\mathbf{r},\omega)\right]. \tag{2.67}$$

An intuitive representation of helicity is obtained in Fourier space. A beam is decomposed into plane waves and helicity measures the polarization handedness in all of these waves. If all the plane waves have the same circular polarization with respect to their momentum vector, then the field will have a well defined helicity. Therefore, a single circularly polarized plane wave is an example for a field of pure helicity.

The conservation of helicity can be seen exemplarily in Fig. 2.8. A general, non-dual object, that is illuminated with a wave of pure helicity (red), may scatter waves of the original and the opposite helicity (blue). Meanwhile, a dual object preserves the incident helicity and produces a scattered field of the same helicity.

A scatterer with the material parameters $\varepsilon_{\mathrm{s}}(\omega)$ and $\mu_{\mathrm{s}}(\omega)$ embedded in a host medium with parameters $\varepsilon_{\mathrm{b}}(\omega)$ and $\mu_{\mathrm{b}}(\omega)$ is preserving helicity if and only if [77]

$$\frac{\varepsilon_{\mathrm{s}}(\omega)}{\mu_{\mathrm{s}}(\omega)} = \frac{\varepsilon_{\mathrm{b}}(\omega)}{\mu_{\mathrm{b}}(\omega)}. \tag{2.68}$$

This means, for an object in vacuum, the material parameters should be the same $\varepsilon_{\mathrm{s}}(\omega) = \mu_{\mathrm{s}}(\omega)$. For a small object in dipole approximation, a similar condition can be found from the definition of the polarizability $\boldsymbol{\alpha}(\omega)$ that characterizes the scatterer

$$\begin{bmatrix}\mathbf{p}(\mathbf{r},\omega)\\ \mathbf{m}(\mathbf{r},\omega)\end{bmatrix} = \begin{bmatrix}\alpha_{ee}(\omega) & \alpha_{em}(\omega)\\ \alpha_{me}(\omega) & \alpha_{mm}(\omega)\end{bmatrix}\begin{bmatrix}\mathbf{E}(\mathbf{r},\omega)\\ \mathbf{H}(\mathbf{r},\omega)\end{bmatrix}, \tag{2.69}$$

where $\mathbf{p}(\mathbf{r},\omega)$ and $\mathbf{m}(\mathbf{r},\omega)$ are the induced electric and magnetic dipole moments for a given external illumination, respectively. Then, the conditions of duality read

$$\alpha_{ee}(\omega) = \varepsilon_{\mathrm{b}}(\omega)\alpha_{mm}(\omega), \quad \alpha_{me}(\omega) = \frac{\alpha_{em}(\omega)}{\mu_{\mathrm{b}}(\omega)}. \tag{2.70}$$

When an object that meets this condition is illuminated by a field containing only one helicity, the induced dipole moments have the fixed relation [4]

$$\mathbf{p}(\mathbf{r},\omega) = \pm\frac{\mathrm{i}}{c}\mathbf{m}(\mathbf{r},\omega), \tag{2.71}$$

where the sign depends on the incident helicity. The fields radiated by these dipoles are also of the same pure helicity [78].

These findings can be applied in the scattering analysis of particles. The first Kerker condition states that in order to completely suppress the back scattering by a sphere, the material parameters should be balanced, i.e. $\varepsilon_{\mathrm{s}}(\omega) = \mu_{\mathrm{s}}(\omega)$. Or equivalently, the electric and magnetic Mie coefficients should be equal [79]

$$a_n(\omega) = b_n(\omega) \tag{2.72}$$

for all n.

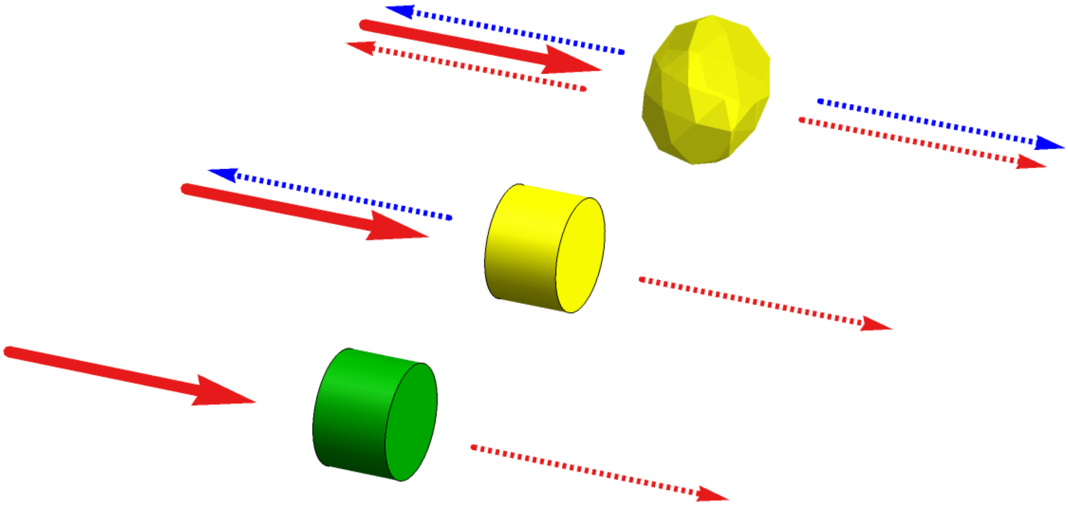

Figure 2.9: Forward and backward scattering by different objects. The thick red arrow represents the incident beam of one helicity. The dashed arrows are scattered fields of the same helicity (red) and of the opposite helicity (blue). Non-dual objects are shown in yellow and the dual object is green. The green object shows no back scattering.

As we see, the Kerker condition is strongly connected to helicity. In fact, it is a special case of duality symmetry and it not only applies to spheres, but also to rotationally symmetric objects.

In Fig. 2.9 we show different cases of illumination with a beam of pure helicity (red). A general object with no special symmetries has mixed contributions in forward and backward scattering. A rotationally symmetric, non-dual object scatters only the incident helicity in forward direction and the opposite one in backward direction. A rotationally and dual symmetric object, however, does not mix helicities. Therefore it shows no back scattering at all, as this would have to be of the opposite helicity [80].

2.4 Summary

In this chapter we presented the theoretical basis of the thesis. We build upon these concepts in the rest of the thesis.

First, we introduced a multiple Mie scattering technique that is capable of simulating the scattering by a cluster of spheres. We expand the incident and scattered fields into vector spherical harmonics with incident and scattering coefficients, respectively. A lot of interesting properties can be calculated from these scattering coefficients such as the multiplolar contributions to the scattering cross section.

We use this technique to a great extent in the next chapter, where we deal with metamaterials built from spherical components. Multiple interesting effects can be observed with these basic building blocks already. We are specifically interested in magnetic dipole resonances at optical frequencies, as they are not observed in natural materials.

Afterwards, we outlined shortly the concept of homogenization. This is of particular importance for self-assembled metamaterials, because we usually end up with bulk materials. Metamaterials are usually composed of building blocks much smaller than the relevant wavelength. Thus, the description of the light propagation does not require to consider all the fine details of the structures from which the material is made. Instead, the medium can be described by effective material properties, which usually greatly simplify the considerations.

Furthermore, we touched the subject of a scattering cancellation device, as an example to demonstrate the homogenization techniques. This is substantiated in chapter 5 with numerical calculations.

Finally, we introduced the duality symmetry of electromagnetic scatterers. This will be very useful in chapter 5, where we investigate approximately dual and maximally chiral objects.

3 Metamaterials with spherical building blocks

In the following chapter, we consider metaatoms and three dimensional metamaterials made of spherical building blocks. We investigate possible designs theoretically and numerically by applying the multiple Mie scattering algorithm that was introduced in the previous chapter. Furthermore, we highlight several experimentally feasible metamaterials with interesting optical properties.

A requirement for many applications in the fields of metamaterials and transformation optics is the availability of bulk materials that possess a strong response to the magnetic field at optical or near-infrared frequencies [54, 57, 81, 82]. While quasi-two-dimensional structures [83, 84], i.e., meta-surfaces exhibiting such a magnetic response, are frequently available, it remains a challenge to fabricate such materials as bulk structures with available top-down technologies. Consequently, bottom-up approaches have been suggested [85–87] which directly provide bulk materials. However, the advancement of this field strongly depends on the identification of metaatoms that provide a suitable optical response *and* that are amenable for a bottom-up fabrication.

The important theoretical step in the description of the interaction of light with an isolated metaatom to a true metamaterial, consisting of many and possibly densely packed metaatoms, is the assignment of effective material parameters. Their unambiguous assignment, however, requires a local response to an external electromagnetic field and thus deep sub-wavelength metaatoms.

Moreover, one important benchmark concerning material properties of metamaterials is the strength of the dispersion in the permeability, ultimately leading to negative values. Although not being strictly necessary to obtain a negative index material, it is usually highly beneficial [88]. A negative permeability is only in reach for a sufficiently strong magnetic resonance. Moreover, having such a strong resonance available, the material may be even operated off-resonant. This entails a reduced absorption while the dispersion remains sufficiently strong, such that all anticipated effects for a negative permeability are less affected by absorption. Thus, if the resonance is stronger it is more likely that it can be used efficiently. One solution to this problem is to incorporate gain material into the unit cells [89]. However, since experimental problems concerning gain materials remain, solutions that only require a modification of the geometry of the metaatom are highly desirable.

In this chapter, we discuss potential solutions to these challenges. Specifically, we present different metaatoms which exhibit a magnetic dipole resonance. These structures are suited for self-assembly fabrication in large volumes, because the metaatoms are built from spherical particles. Moreover, because of the spherical building blocks, we can perform precise and efficient simulations of the optical response of single metaatoms or clusters of several metaatoms as described in the previous chapter 2. These results can be used to perform a volume homogenization to approximate the response of a bulk metamaterial made out of the basic building blocks.

We start by presenting a sophisticated structure theoretically in section 3.1. We design a core-shell system with a large central sphere, decorated with a large number of small metallic particles. Such a metaatom can sustain a magnetic and electric resonance almost at the same frequency. It is, therefore, suitable to build a negative index material. We propose several ways to improve the performance of the suggested metaatom, i.e., how to increase the dispersion of the effective permittivity and permeability of the resulting bulk material.

Afterwards, we consider experimentally realized metamaterials. Here, we strongly collaborate with experimental physicists and chemists from the Friedrich-Schiller-University of Jena to fabricate and characterize the proposed designs. There, we investigate a very simple design that sustains a magnetic dipole resonance: a plasmonic dimer. Hereby we highlight the design, fabrication, and characterization of the metaatom.

Then a more complicated structure is investigated. A large number of small spherical metallic particles is assembled to form a large cluster inside a polymer sphere. The metallic particles are then treated with a seeded growth procedure. As a result, either gold spheres with increasing radii or gold-silver core-shell particles are formed. The combined cluster sustains a magnetic dipole resonance, depending on the filling faction of metal inside the cluster and the choice of the material. Our numerical calculations provide a valuable insight into the underlying physics.

Finally, we present an actively thermally tunable metamaterial in section 3.3. A major flaw of the designs that are usually considered is that the resulting material is static. However, dynamically tunable materials are often needed for state-of-the-art applications. We consider a metamaterial that exhibits epsilon-near-zero properties, which are switchable in the time frame of a few seconds. The material consists of small silver spheres, which are covered with and connected by a liquid crystal. This liquid crystal changes its geometrical structure upon heating or cooling, respectively. Two different phases are reached and the process is completely reversible.

3.1 Negative index material with core shell clusters

As has been shown in numerous recent works, fabrication of metaatoms with a magnetic dipole response with bottom-up techniques is possible [23, 41, 90, 91]. However, typically these magnetic resonances are weak, when compared to the electric dipole resonance. A requirement for many applications and a long-standing

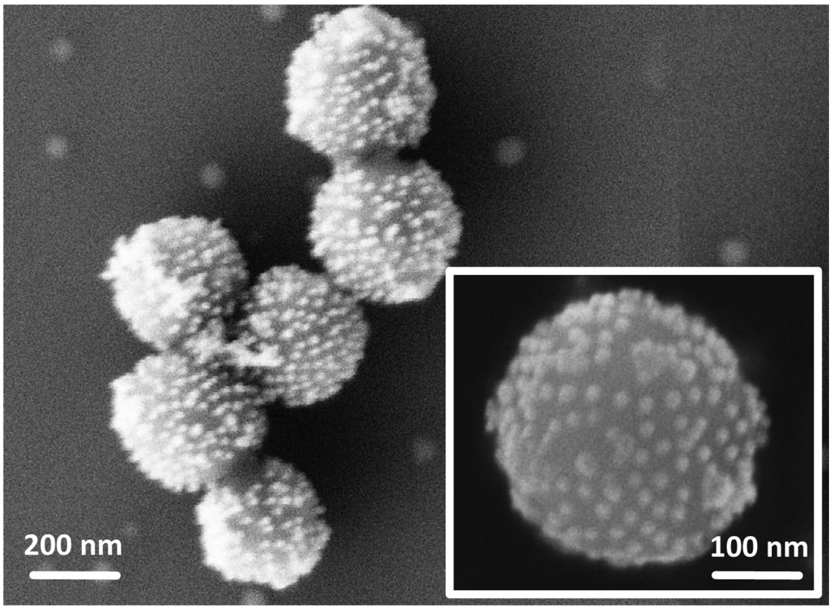

Figure 3.1: Scattering electron microscopy (SEM) picture of self-assembled core-shell clusters. A large number of metallic particles is assembled on the surface of a big dielectric sphere. Image taken from Ref. [23].

vision in optics is the availability of a material with a negative index of refraction, for which a strong magnetic resonance is a prerequisite.

It has been shown that a highly isotropic magnetic response can be sustained by core-shell clusters consisting of a dielectric core sphere surrounded by metallic particles forming a shell [23], as seen in Fig. 3.1. The magnetic resonance can be intuitively understood as a collective plasmonic resonance of all the metallic spheres, where the induced dipole moments are all oriented clockwise or counter clockwise, respectively. At an effective level, this can be considered as a circulating current. This induced ring current causes a scattered field that corresponds to an oscillating magnetic dipole.

An important task in the theoretical description of metamaterials is the proper transition from an isolated metaatom to a bulk metamaterial. This requires to assign effective material properties such as $\varepsilon_{\text{eff}}(\omega)$ and $\mu_{\text{eff}}(\omega)$ to the metamaterial. However, such a description is usually only possible in the dipole approximation, where the particles have to be much smaller than the operating wavelength. To warrant this, one possibility is to shift the resonance to longer wavelengths while preserving the geometrical extension of the metaatom. The feasibility of this concept has been recently shown for sandwich particles that consist of two strongly coupled metal patches [92].

Moreover, to reach a negative index of refraction, the material needs to have a sufficiently dispersive permeability. Therefore, besides the requirement that the metaatom shall be sufficiently small with respect to the wavelength, it is also important that the magnetic response is sufficiently strong. Additionally, the permittivity should be negative in the same spectral region to get a negative index of refraction [88]. A downside of plasmonic materials is the typically high absorption at resonance. This absorption usually denies the clear observation of the dispersive behavior of the material properties. Therefore, if the magnetic response of the material is sufficiently strong, the metamaterial can be operated slightly off resonance, to ensure low absorption while still capitalizing on the dispersive effects.

In this section, we demonstrate how the magnetic resonance of a core-shell cluster is shifted to the near infrared regime while keeping the geometrical extensions constant. To perform such a shift, we replace the solid particles in the shell with hollow spheres. This strongly shifts the resonance of the individual metallic nanoshell, with the strength of the shift depending on the shell thickness. Thereby, the design is notably improved along the lines outlined above. Ultimately, we also present the design of a metaatom that allows for a negative index of refraction. The results presented in this section are largely based on the work published in reference [1].

3.1.1 Nanoshells

The basic building blocks of the metaatom considered here are hollow metallic spheres, called nanoshells, with a fixed outer radius $r_\mathrm{o} = 15$ nm and a variable inner radius r_i. At first, we investigate the resonance behavior of the single nanoshell in water with a nondispersive permittivity $\varepsilon_\mathrm{b} = 1.7$. Figure 3.2 A shows the geometry of the nanoshell. The spectral response of the nanoshell with varying shell thickness was calculated with the Mie scattering method and the resonance frequency was extracted. The solid nanosphere has the localized plasmon polariton resonance frequency at the usual value for silver particles in water, i.e. 770 THz. At this spectral position, a core-shell cluster made out of these solid spheres would hardly be subwavelength ($\lambda = 390$ nm and diameter of the cluster 180 nm). If we increase the inner radius of the nanoshell the resonance will shift to lower frequencies, or longer wavelengths, respectively [93], as is shown in Fig. 3.2 B. This redshift occurs due to the hybridization of the plasmon resonance of the sphere and the resonance of a cavity that can be considered at the outer and inner surface of the nanoshell, respectively.

As can be seen in Fig. 3.2 B, the resonance frequency changes strongly once relatively thin shells are reached. Thus, a shift of about 500 THz is possible, by changing the inner radius from 0 to 14 nm, or, in other words, decreasing the shell thickness from a solid sphere to 1 nm. This is achieved while keeping the outer geometry fixed. Additionally, the resonance amplitude increases, until a maximum between 1 and 2 nm shell thickness is reached as is shown in Fig. 3.2 C. The amplitude increases, because the resonance of the growing cavity effectively contributes to the scattering. At some point, however, the nanoshell is so thin that it can not sustain a resonance anymore.

Even though it is challenging to fabricate such thin shells, it is possible with galvanic replacements methods [94] or by depositing silver ions on electrostatically charged dielectric spheres [95]. However, we should note that for such thin shells, the

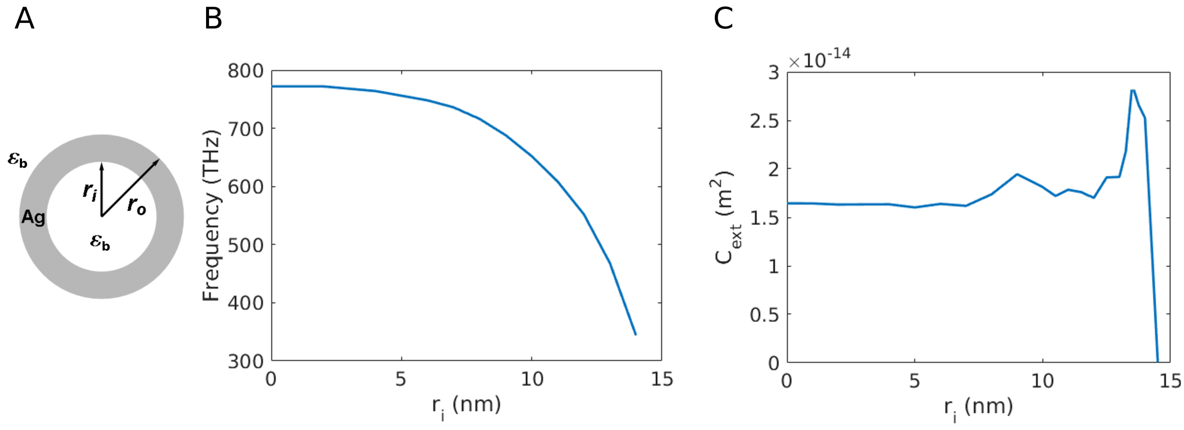

Figure 3.2: (A) Geometry of the nanoshell. Here, ε_b denotes the permittivity of the environment and r_i and r_o are the inner and outer radius, respectively. (B) Simulated resonance frequency of a silver nanoshell as a function of the inner shell radius r_i with a fixed outer radius $r_\mathrm{o} = 15$ nm. (C) Simulated maximum extinction cross section of a nanoshell as a function of the inner shell radius.

effective description with a bulk permittivity is driven to the extreme, because the shell has a thickness of only a few atoms.

During this section we exploit the shown tunability to design deep sub-wavelength core-shell clusters with a strong magnetic response.

3.1.2 Core-shell clusters

Now, we take these nanoshells as building blocks to compose a core-shell cluster.

To compare with our later results of the improved design, we introduce a referential design that is similar to established core-shell clusters with a magnetic dipole resonance [23]. We form a cluster out of 60 solid silver nanospheres with a radius of 15 nm that are surrounding a dielectric core sphere. It has been shown that a reasonably large number of particles (in the order of tens to hundreds) is necessary to support a magnetic resonance [23]. The spheres are arranged in groups of pentamers on the facets of a dodecahedron, as can be seen schematically in Fig. 3.3 A. The core sphere has a radius of 60 nm and a nondispersive permittivity of $\varepsilon_\mathrm{c} = 2.25$. The surrounding material is again water with $\varepsilon_\mathrm{b} = 1.7$. Note that this is just a referential geometry. Randomized realizations also show the desired effects, as we show later in this section.

We can see from Fig. 3.3 B that a magnetic dipole resonance appears at 540 THz. We calculate the polarizability of the cluster with the multiple scattering method outlined in chapter 2. Then, the effective permeability of a material made out of these core shell clusters can be calculated with the Clausius-Mossotti equation 2.60. Even if we use an extremely high filling fraction of 68%, the dispersion of $\mu_\mathrm{eff}(\omega)$ is

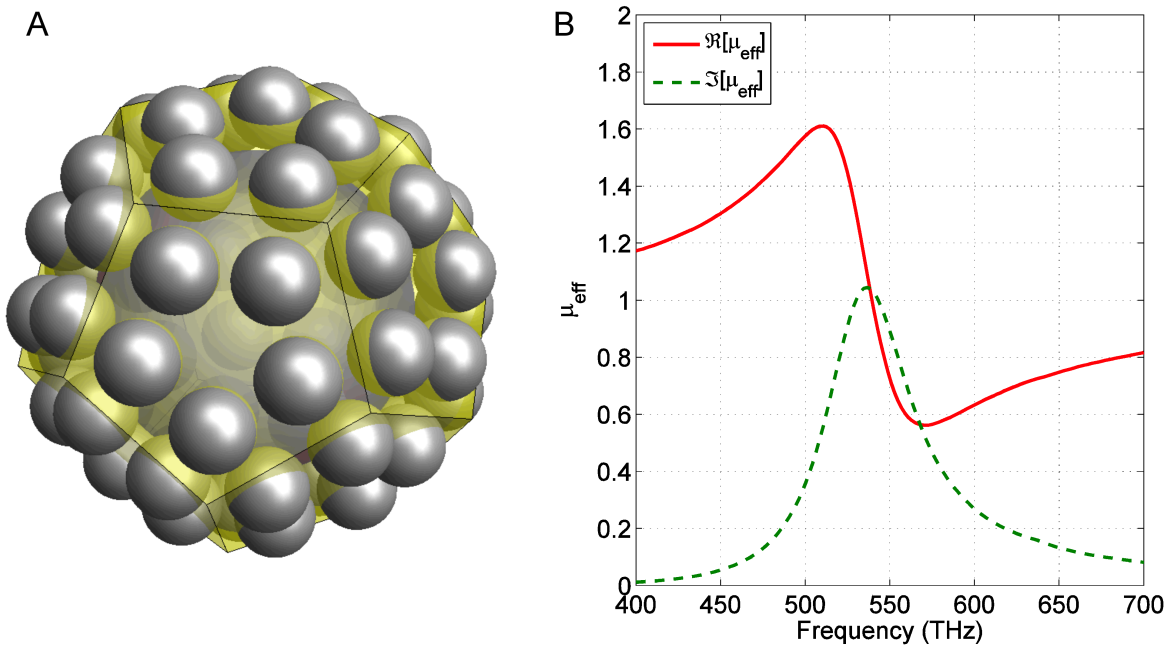

Figure 3.3: (A) Geometry of the core-shell cluster. 60 silver nanospheres (or nanoshells, respectively) are aligned on the faces of a dodecahedron, indicated in yellow. (B) Real and imaginary part of the effective permeability $\varepsilon_{\text{eff}}(\omega)$ of a core-shell cluster made from solid silver nanospheres.

weak and negative values can not be reached. This is typical for designs with solid metal spheres and a negative index material can not be realized with these values.

Now we use the previously shown tunability of the nanoshells to change the resonance position and shape of the magnetic dipole resonance. The outer radius of the nanoshells is kept constant and the inner radius is increased. This fully preserves the geometrical extension and shape of the core-shell cluster. The effect on the magnetic resonance can be observed in Fig. 3.4 A. As expected from the results of the single metallic nanoshell, the resonance shifts to lower frequencies, because it is tied to the plasmon resonance of the shells. Furthermore, the resonance features get much sharper and stronger. This can be explained by the enhanced resonance strength of the nanoshells. However, the thickness should not be too thin, because losses increase again for extremely thin metal shells, due to the shorter mean free path length for the electrons in the shell. A further contribution to the sharper and stronger resonance is the reduction of the radiative losses. These radiative losses are reduced, because the cluster is much smaller compared to the resonance wavelength. Most importantly for our purposes, we observe that the real part of the permeability now attains negative values. This means that an essential requirement for a negative index material is satisfied.

As was outlined before, the homogenization with the Clausius-Mossotti equation is only reasonable if the inclusions can be well described in the dipole approximation. For this reason, we take a look at the multipole decomposition of the scattering cross section in Fig. 3.5. This was calculated with the multiple Mie scattering

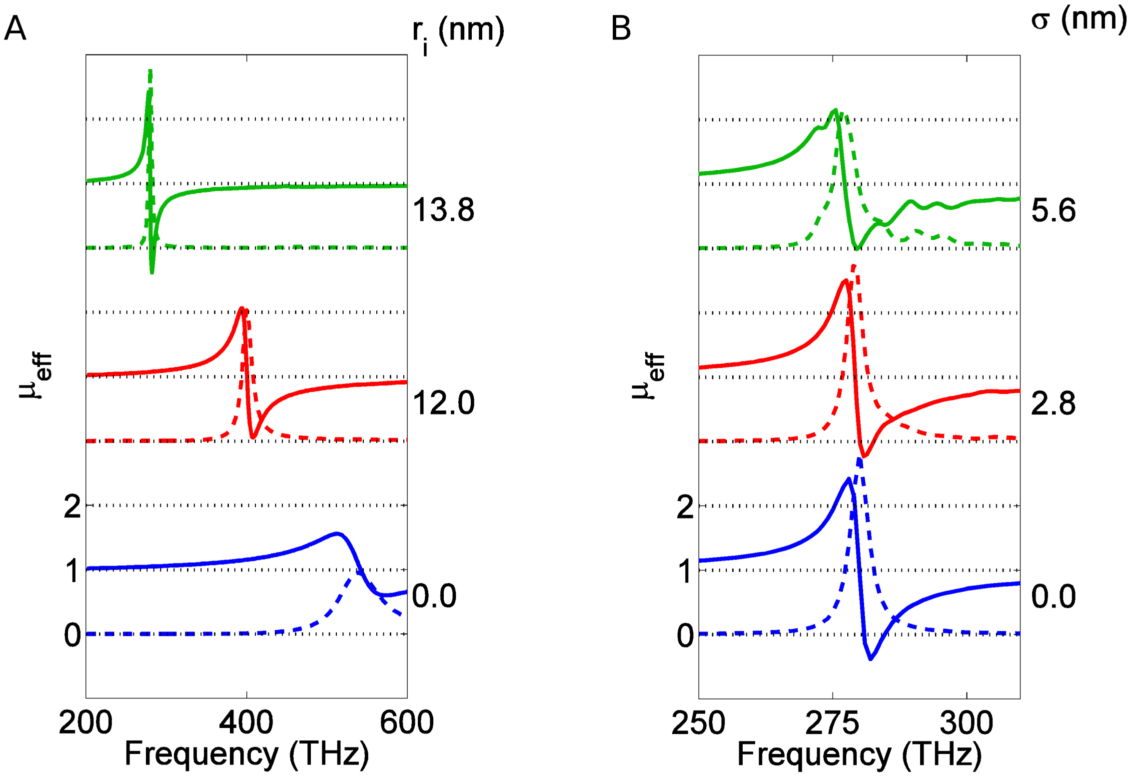

Figure 3.4: (A) Effective permeability of a material made of core-shell clusters with nanoshells with different inner radii r_i. The resonance shifts to lower frequencies and gets sharper with increasing inner radius. (B) Effective permeability for a cluster with spatially disordered nanoshells with $r_\mathrm{i} = 13.8$ nm. The disorder is quantified by an average spatial displacement σ corresponding to a normally distributed shift.

method using fourth order expansion of the fields. We clearly see the contribution of different multipoles for two different realizations, A: the referential design with solid nanospheres and B: the same geometry, but with nanoshells with an inner radius of $r_\mathrm{i} = 13.8$ nm. We recognize that the magnetic dipole resonance (red) for the referential design is partially superimposed with higher order multipole resonances. Thus, the dipole approximation is, strictly speaking, not applicable for the referential design, but it should constitute only as a guideline. On the other hand, we see that the cluster with nanoshells exhibits a much sharper magnetic dipole resonance, which is well isolated from resonances in higher order multipoles. This suggests that the homogenization is feasible, at least in the spectral region where a strong dispersion in the permeability is induced. Furthermore, the resonance is shifted to much lower frequencies (note the different spectral domains in the plots). All these effects cause a sharper and stronger resonance in the effective permeability.

For practical realizations it is very important to study the effects of disorder introduced into the cluster. We show that the design is sufficiently robust against disorder. Thus, a possible fabrication comes in reach.

The deterministic ordering of the particles inside the shell facilitates the excitation of

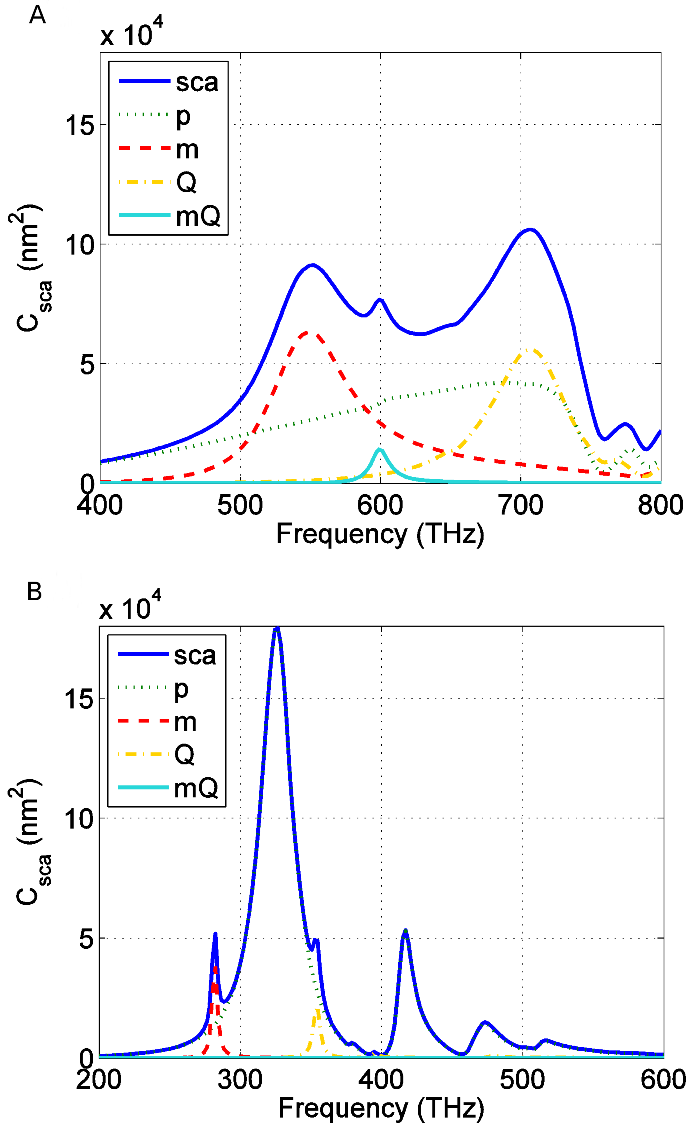

Figure 3.5: Scattering cross section of the core shell cluster. (A) Cluster with bulk silver spheres. (B) Cluster with silver nanoshells with $r_\mathrm{i} = 13.8$ nm. Blue: total scattering cross section. The other curves display the contributions of different multipoles: electric dipole (green dotted), magnetic dipole (red dashed), electric quadrupole (yellow dash-dotted), and magnetic quadrupole (cyan).

the magnetic resonance. We show this by investigating the effects of disorder. Figure 3.4 B shows how a randomized displacement of the nanoshells on the surface of the central sphere affects the magnetic response. The normally distributed displacement is quantified by σ. It shows how much each sphere is displaced from its original position in average. As we see, the resonance is slightly weaker and broader. This can be understood by appreciating that when disorder is introduced, the coupling to the nearest neighbor nanoshell on the surface is slightly and statistically modified. This coupling, however, has an impact on the spectral position of the plasmonic resonance and detunes it. Now the occurring superposition of many resonances that are slightly shifted causes an inhomogeneous broadening of the resonance. This shift directly translates to the observed broadening.

We can state that, if the fabrication precision is kept below approximately 5 nm, only a marginal distortion of the resonance is observed. Thus, a self-assembled fabrication with electrostatic interaction is possible to construct a material with a negative effective permeability. The major cause of distortion of the resonance is a very short distance of the nanoshells on the surface. This can be circumvented experimentally by introducing a dielectric spacer layer on the nanoshells to keep a minimum distance.

3.1.3 Negative index of refraction

We have shown how to shift the resonance of interest to longer wavelengths and, thus, reduced the relative size of the object while keeping the geometrical size constant. In fact, the ratio of size over wavelength is $1/8$ for the best case of nanoshells with an inner radius of 13.8 nm as opposed to $1/4$ for solid spheres. Now we want to show how we can make use of this design to construct a negative index material.

A negative index of refraction can be reached, if the negative permeability is accompanied by a negative effective permittivity at approximately the same frequency. We achieve this by extending the previous design. The dielectric core sphere is replaced with a gold shell. This core particle exhibits a strong electric dipole resonance, which can also be tuned by changing the inner and outer radius of the core shell. So by varying the inner and outer radii of the core and the nanoshells, respectively, we can tailor both resonances almost independently. We can get a negative index if we bring them to a spectral overlap. In Fig. 3.6 we display the effective permittivity, permeability, and refractive index of a material made out of the proposed metaatoms. We use a central gold shell with inner radius $r_\mathrm{i} = 45$ nm and outer radius $r_\mathrm{o} = 52$ nm and silver nanoshells with $r_\mathrm{i} = 13.8$ nm and $r_0 = 15$ nm. The effective refractive index is calculated as

$$n(\omega) = \sqrt{\varepsilon_\mathrm{eff}(\omega)\mu_\mathrm{eff}(\omega)}. \tag{3.1}$$

The effective permittivity now exhibits a double resonance structure. This is because the combined core-shell cluster has one resonance corresponding to the shell, which is composed of nanoshells and, additionally, one resonance corresponding to the core particle. The parameters of the core-shell cluster were optimized to minimize the real part of the effective refractive index of the resulting material. It is crucial to bring the two mentioned resonances spectrally close together. However, the resonances should not coincide, because they negatively affect each other. This is another reason why we need a strong magnetic resonance. The dispersion in the effective permeability can be completely suppressed by the strong electric dipole resonance if the magnetic resonance is too weak.

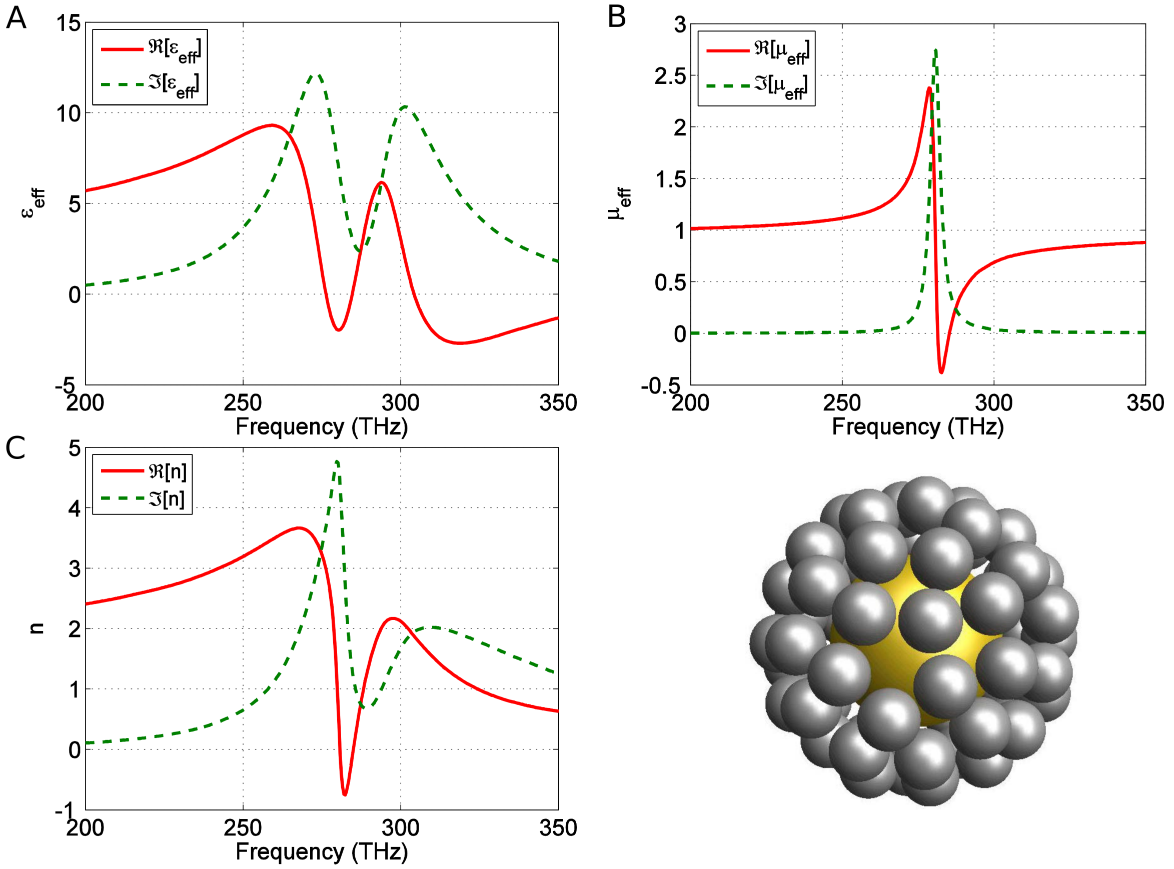

Figure 3.6: Effective permittivity (A), permeability (B), and index of refraction (C) of a core-shell structure with $r_\mathrm{i} = 13.8$ nm and $r_\mathrm{o} = 15$ nm of the silver nanoshells and $r_\mathrm{i} = 45$ nm and $r_\mathrm{o} = 52$ nm of the central gold shell. The real part is depicted in red and the imaginary part in green, respectively. We observe a strong dispersive behavior of both $\varepsilon_\mathrm{eff}(\omega)$ and $\mu_\mathrm{eff}(\omega)$, which leads to a negative refractive index $n(\omega)$.

As we see in Fig. 3.6 C, the advanced material indeed shows a negative index of refraction in a frequency domain of approximately 10 THz with values down to $n = -0.8$. Additionally, the region of negative index can be shifted to some extent by adjusting the inner and outer radii of the core particle and the nanoshells, respectively.

3.1.4 Conclusion

We designed a deep sub-wavelength metaatom with a strong magnetic dipole resonance. It can be used to construct a material with negative effective index of refraction. We started from an ordinary, established core-shell cluster with a magnetic dipole response. By replacing the solid spheres with nanoshells, we can tune the resonance to longer wavelengths to get a sub-wavelength metaatom with a strong resonance.

Introducing an additional metallic shell at the center causes additionally a tunable electric dipole resonance. When both resonances spectrally overlap, a negative index of refraction can be reached in a material made out of these metaatoms.

By investigating the effect of disorder, we have shown that a fabrication by means of self-assembly processes is possible. The magnetic resonance is sufficiently robust.

3.2 Experimental realizations of self-assembled metamaterials

In the previous section we introduced a sophisticated design, which potentially exhibits a strongly dispersive permeability and, ultimately, a negative index of refraction. Now, we want to consider possible experimental realizations of metamaterials with a magnetic response. We have closely collaborated with experimental partners from the Friedrich-Schiller-University Jena, who fabricate and characterize the designs. Even though not directly linked to a magnetic resonance, we describe at first a setup where the fabrication of a dimer was in the focus of interest. This can be considered as the most simple building block that is more complicated than an isolated metallic nanosphere. In section 3.2.2, we describe more recent results on the fabrication of meta-atoms with a spherical geometry and composed out of a dense package of metaatoms. Experimental efforts to realize the metaatoms described in the section above are a part of ongoing research activities. Results are, at the moment of writing this thesis, not yet available. Therefore, even preliminary results are not included here.

3.2.1 Plasmonic dimer

Bringing two or more nanoparticles into close vicinity causes the localized surface plasmons of the individual spheres to couple [96]. Most notably, the coupling causes a strong field enhancement in a confined area in the junction of the nanoparticles. This can be intuitively understood by considering the junction in lowest order approximation as a parallel plate capacitor. The electric field strength for a fixed potential in such capacitance scales inversely proportional to the distance. Small distances, therefore, enhance the field strength enormously. Such strong fields are highly desirable for many applications, for which surface enhanced Raman spectroscopy (SERS) is a referential example. The strong field confinements in such junctions allow to address single molecules [97], which opens unprecedented opportunities for example in sensing [98, 99], medicine [100, 101], or nanobiology [102, 103]. Therefore it is highly desirable to reach sufficiently small separations.

Maybe the most simple implementation of such junctions is a nanoparticle dimer, an object that consists of two identical spheres in close proximity connected by a linker. They are typically fabricated with bottom-up methods, e.g., via complementary DNA [104], click chemistry [105], Diels-Alder [106], and other chemical methods. Another possibility to perform the assembly, is to use functionalized organic molecules. These linker molecules can either be flexible dithiols or rigid molecules [107–109]. However, the exact bonding mechanism of these linkers remains often an open question. For example, a shift of the plasmon resonance over time during the nanoparticle assembly was noted. This indicates a transformation from assemblies of particles with a defined distance to those with shorter or longer distances [110].

The theoretical and numerical considerations in this section are strongly linked to experimental results. We present schematically the self-assembly fabrication of a gold nanosphere dimer with a special designed linker molecule, which was performed by Florian Kretschmer. This molecule allows for a stable connection with a specific distance between the spheres. By changing the concentration of the linker molecule in the solution, the cluster sizes of the resulting product can be controlled. These different clusters can then be separated by density gradient centrifugation, which was done by Igor Perevyazko. Furthermore, surface enhanced Raman spectroscopy was performed by Dana Cialla-May to find individual metaatoms and characterize their response. More detailed information about the experimental aspects can be found in Ref. [5] and the supporting information of this reference, where the results presented in this section were published. These experimental results are motivated and supported throughout this section by numerical calculations performed with the multiple Mie scattering technique.

Self-assembly fabrication

By choosing a special linker molecule, the dimer can be constructed in a self-assembly fabrication. The molecule has a defined length of approximately 2 nm and a rigid form. Therefore, we obtain a defined end-to-end distance of the dimer, see Fig. 3.7 for a schematic representation of the dimer with the molecule in the gap.

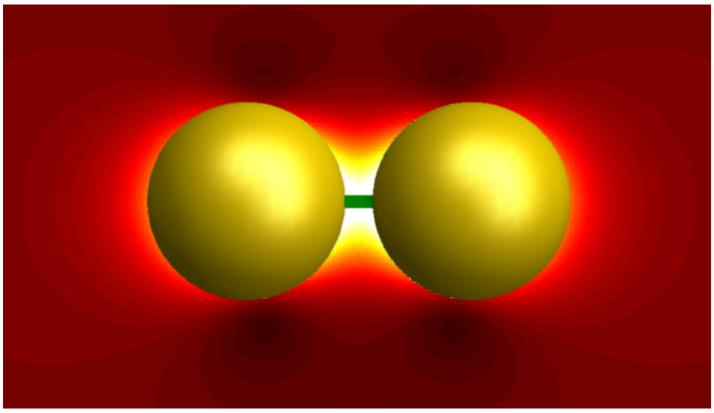

Figure 3.7: Schematic representation of the dimer with the linker molecule between the gold spheres and a strong field enhancement in the gap.

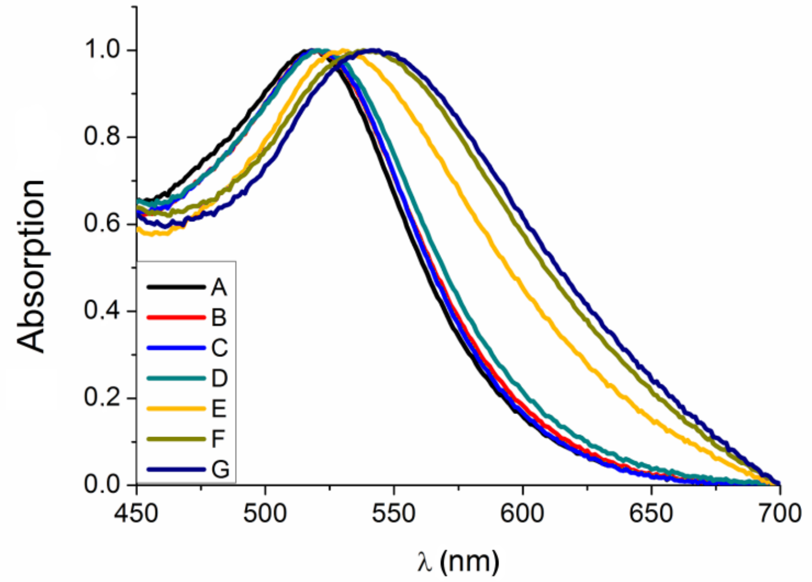

Figure 3.8: Normalized absorption spectra of the solution of gold nanoparticles. The plasmon resonance is clearly seen as the peak in the spectral range of 500 to 560 nm. It shifts to the red part of the spectrum with increasing amounts of linker and DBU.
A: Au nanoparticle solution,
B: Au nanoparticle control solution with only 100 g/mL DBU,
C-G: Au nanoparticle solutions with increasing amounts of the linker and DBU (20, 40, 60, 80, 100 g/mL), respectively.

The gold nanoparticles were prepared with the Turkevich method [111] which yields stabilized nanospheres. The spherical shape and the mean radius of 6.5 nm were confirmed with transmission electron microscopy (TEM) measurements. To form dimers or higher order assemblies, a mixture of the linker molecule and diazabicycloundecene (DBU) was added to the nanospheres. The DBU is necessary to activate the linker [112]. By changing the concentration of the linker molecules in the mixture, the assembly process can be tuned. Low concentrations lead to a small shift of the plasmon peak at 520 nm for single nanoparticles. This can be partially attributed to the change of the refractive index of the liquid due to the different compounds and partially to a few dimers that are being formed. If the concentration of the linker molecule and DBU is increased, we observe a larger red shift and also a broadening of the resonance, due to the formation of more dimers and higher order assemblies, as can be seen in Fig. 3.8.

A control measurement with only DBU added to the spheres is performed to ensure that the assembly of nanoparticles was not caused just by the addition of DBU instead of the linker. Because DBU acts as a base and increases the ionic strength of the solution it could also cause an aggregation [113]. This control measurement shows only a marginally redshifted resonance (red line in Fig. 3.8), especially compared to the mixture with the same amount of DBU and the linker molecules (dark blue

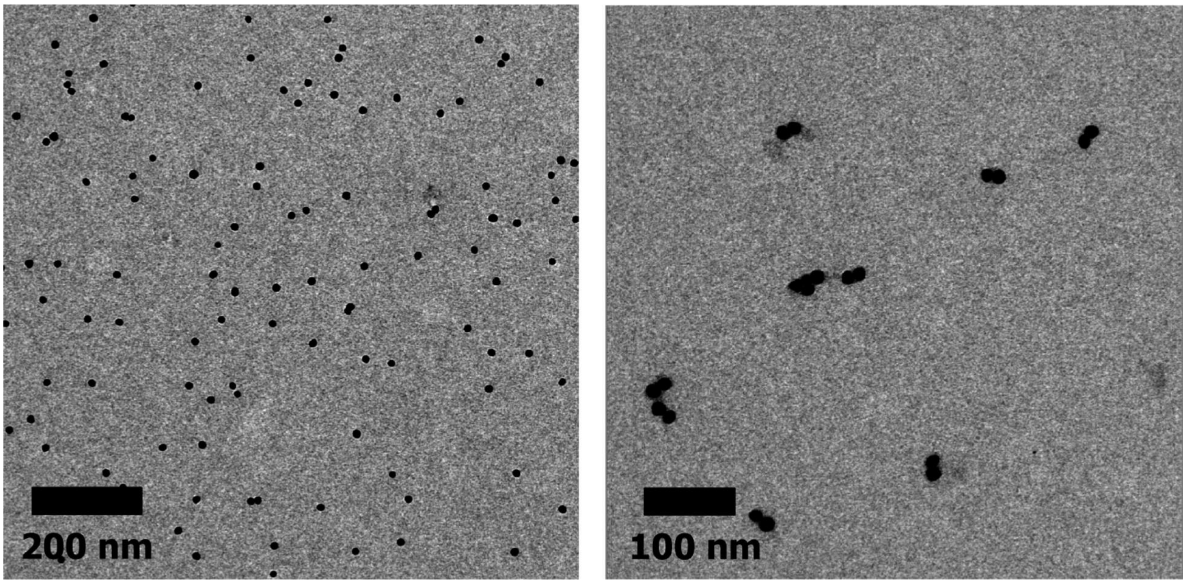

Figure 3.9: TEM images of the top fraction I of the centrifugation process (left) containing single nanoparticles and the bottom fraction II (right) containing almost exclusively dimers and a small number of higher assemblies.

line).

The increase of the linker DBU mixture concentration leads at first to an increased number of formed dimers. But at some point, the small assemblies will link to form very large clusters and eventually all particles will precipitate.

To separate the different nanoparticle assemblies, a density gradient centrifugation technique is used [114, 115]. The dimers have a higher frictional coefficient than single particles due to their increased cross section. However, they have twice the mass of a single particle, which overcompensates the frictional coefficient. In total, higher order assemblies have also higher sedimentation coefficients, meaning that they will be separated on the bottom in a centrifugation process.

We can attribute the upper phase, which we call fraction I, to single particles with different sizes and the lower phase, which we call fraction II, to all higher assemblies, which are formed during the self-assembly step, i.e., almost exclusively the dimers we are interested in. This is confirmed by TEM measurements of fraction I and II, which reveal that they consist indeed almost exclusively out of monomers and dimers, respectively, as can be seen in Fig. 3.9. Fraction II is used for the following analysis of the dimer structure.

Characterization

Now, we want to optically characterize the nanoparticle clusters.

Absorption measurements of the centrifuged fractions I and II were performed and compared to simulations of a single sphere and a dimer in water, respectively. The absorption cross section is calculated numerically with the multiple Mie scattering

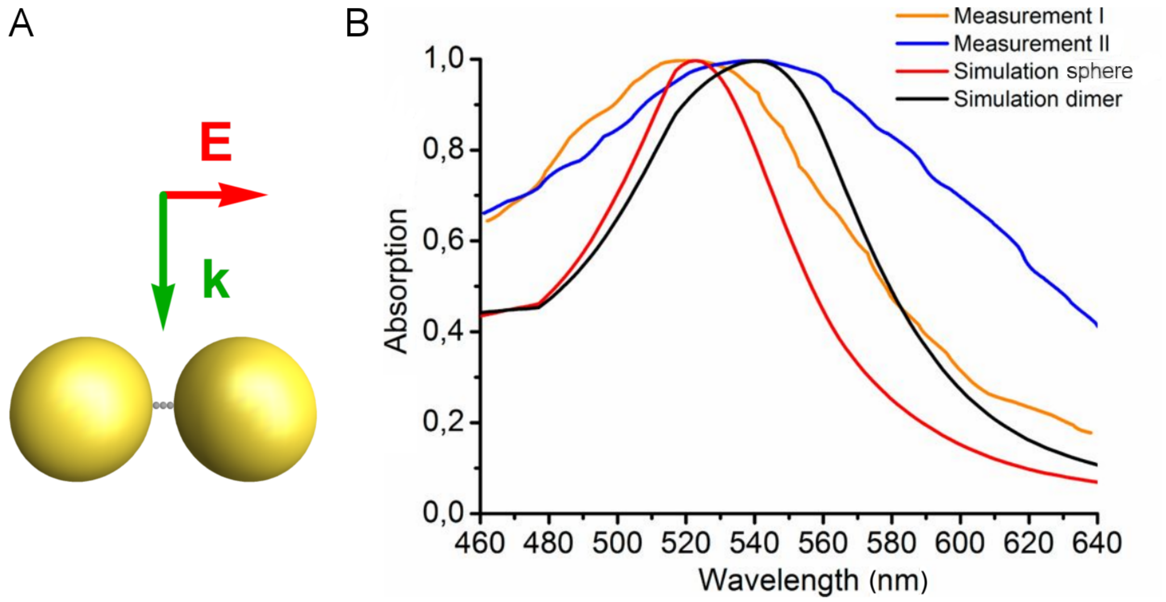

Figure 3.10: (A) The geometry and illumination that is used for the dimer simulations. (B) Normalized measured (orange and blue) absorption spectra of the centrifuged fractions I and II in comparison with simulated (red and black) absorption spectra of a single nanoparticle and a dimer surrounded by water, respectively. The resonance positions agree very well.

algorithm presented in section 2.1.2. Spheres with a radius of 6.5 nm and a separation of 2 nm are assumed, corresponding to the experimental measurements. We use tabulated permittivity data for gold [69] and the surrounding medium is water for which we assume a nondispersive permittivity of $\varepsilon_{\mathrm{b}} = 1.7$. For these simulations we modele the linker molecule as a chain of three small spheres with a radius of $\frac{1}{3}$ nm in the gap between the gold spheres. We assume a refractive index of $n = 1.4$ as a typical value for such molecules. The dimer is illuminated with a plane wave, polarized parallel to the connection line of the particles. The results are shown in Fig. 3.10. We can observe a perfect agreement of the resonance positions. The much higher width of the measured resonances can be attributed to a slight variation of sizes of the particles in the solution. The optical response is very well reproduced by a simulation of a single sphere or dimer, respectively. The reason is the low concentration of nanoparticles in the investigated solution.

The structure of the synthesized dimers is expected to support a strong field enhancement between the spheres as outlined before. This is especially interesting for SERS measurements, which require strong electromagnetic fields at the position of the investigated molecule.

We provide insights into the field excitation in the junction between the spheres of the dimer by performing full wave simulations with the same set up that was used above for the absorption calculation.

In Fig. 3.11 we see the absolute value of the electric field at the wavelength 28.6 μm.

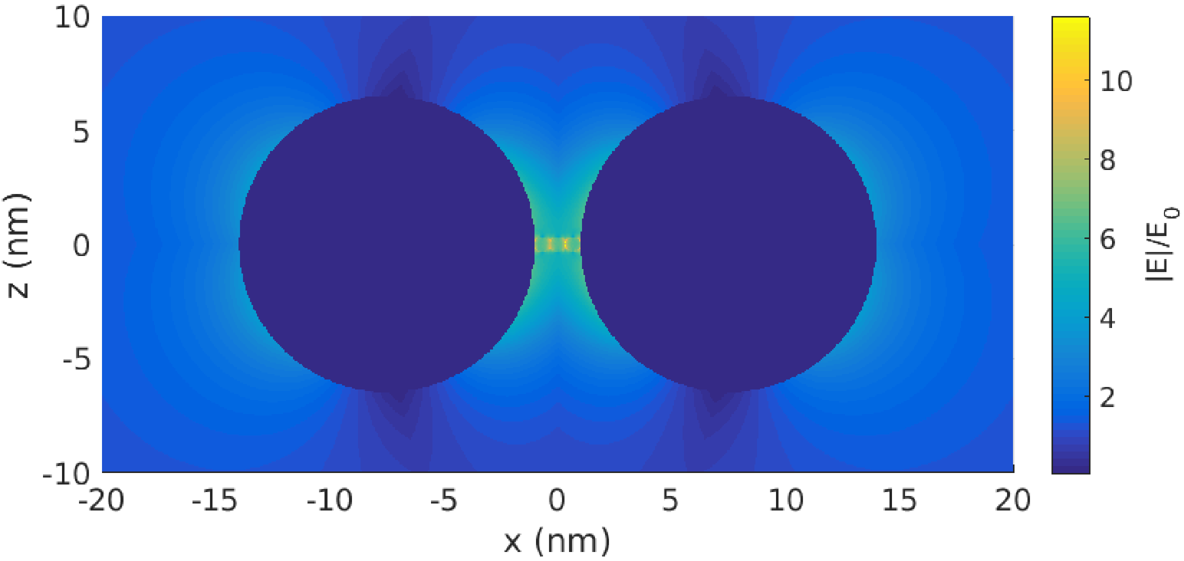

Figure 3.11: Field calculation of the dimer particle. Absolute value of the electric field at the wavelength 28.6 μm. The field is normalized with the amplitude of the incident field $\mathbf{E}_0$.

This wavelength corresponds to the major Raman mode of the linker molecule. The field excitation is localized in the space between the metallic spheres, exactly where the linker molecule is positioned. This shows that we have the strongest fields at the position of the linker, which suggests strong Raman modes in the SERS measurements. In fact, the field is one order of magnitude stronger than the incident field. This implies a SERS enhancement of 10^4, because the field enhancement happens twice (once the incident field is enhanced and once the scattered field of the molecule).

SERS measurements of the pure linker molecule solution were recorded without

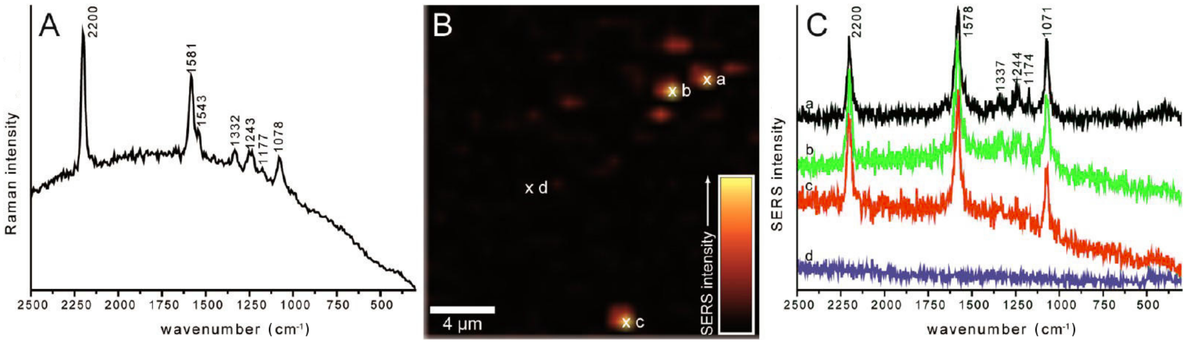

Figure 3.12: SERS-based characterization of gold nanoparticle clusters. (A) Reference Raman spectrum of the linker molecule without nanoparticles. (B) Normalized SERS intensity map. Here, bright spots indicate the presence of nanoparticle clusters. (C) Related SERS spectra (a-c) and background signal of the substrate (d). The spectra were recorded at the spatial positions indicated in B. The measurements were performed with an excitation at a wavelength of 633 nm.

metallic particles as a reference (Fig. 3.12 A). Then a sample of section II (the centrifuged part containing the dimers) was coated on a glass substrate and investigated. Figure 3.12 B shows the intensity map of the bright Raman mode at $2200\ \mathrm{cm}^{-1}$ of the spread out sample. The spectroscopic wavenumber corresponds to a wavelength of $28.6\ \mu$m which was investigated in the field calculation. We can identify the positions of nanoparticle clusters as bright spots and conduct the spectral measurements at these positions. In Fig. 3.12 C we see the Raman spectra of three positions with nanoparticles and one control measurement of a spot with presumably no particles. We can clearly identify the resonances of the linker molecule, while the control spectrum produces only noise. This means we have indeed detected the positions of the clusters and the field excitation between the individual particles increases the signal by a large margin.

Furthermore, not only the presence of the linker can be verified, but also its orientation. The Raman modes can be attributed to specific vibrations and rotations of the molecule. Specifically, the resonances at $2200\ \mathrm{cm}^{-1}$, $1578\ \mathrm{cm}^{-1}$ and $1071\ \mathrm{cm}^{-1}$ are all preferably enhanced and indicate an upright orientation of the molecule on the metal surface [5].

Conclusion

We showed the design, fabrication, and characterization of a dimer particle and the corresponding linker molecule. The self-assembly method that was used is a cheap and efficient way to fabricate large amounts of dimers. Furthermore, we showed that the measurement and simulation results of the absorption spectrum correspond very well. The field calculations demonstrated that the dimer particles can be effectively used in SERS measurements because the structure exhibits a strong field excitation in the gap of the dimer. This was also confirmed by measurements, as showcased for the case of the linker molecule.

3.2.2 Clusters of shells with tunable thickness

The major problem with top-down fabricated metaatoms is typically the high anisotropy. This problem can partially be circumvented with self-assembly methods. But assemblies with a low number of constituents, such as the dimer, usually show an anisotropic response as well. In fact, the optical response to a field excitation along the connection line of the dimer is very different from the response to an excitation perpendicular to the connection line [116].

One way to alleviate this problem is to use spheres aligned in a tetrahedral shape. Then, they exhibit a completely isotropic response, due to their geometric symmetry. However, they can only be fabricated with low yields. Then, a complicated separation from higher and lower order assemblies is necessary.

This problem can be solved when we increase the number of particles in the assembly and force them to form a spherical shape. This way, we get an approximately isotropic response by design. Furthermore, a slightly increased or decreased number of particles has only a negligible influence on the optical response, thus making an expensive sorting technique obsolete.

The optical response of such a globular cluster is highly depending on the nearest neighbor distance of the constituting particles. Thus changing the size and/or filling fraction strongly influences the result.

In the following, we present the fabrication and characterization of spherical clusters consisting of several hundreds of metallic spheres. Furthermore, we show a seeded growth technique to either tune the size of the particles, or turn them into core-shell spheres consisting of two different metals with tunable shell thickness. This fabrication and characterization was performed by Florian Kretschmer and Reinhard Geiss, respectively. The measurements are accompanied and explained by numerical calculations performed with the multiple Mie scattering technique, as explained in chapter 2. For more information about the experimental realization see reference [2], where these results were already published.

Self-assembly fabrication

As shown in Fig. 3.13, large polymer spheres are created by mixing the polymer PEI with the gold salt $HAuCl_4$ and heating the mixture [117]. A high number of several hundred gold particles is formed inside the polymer sphere. The size of the polymer sphere and the gold filling factor can be reliably tuned by changing the concentration of the reactants [2]. An initial gold filling fraction of 2.7% is chosen. There, no effect of the coupling of the gold spheres can be observed, the spectrum is dominated by the response of the single gold particles.

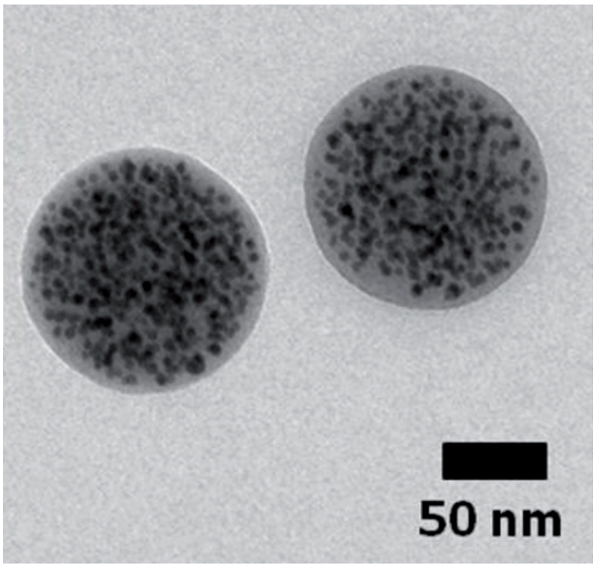

Figure 3.13: TEM image of the polymer-gold clusters prior to the seeded growth process.

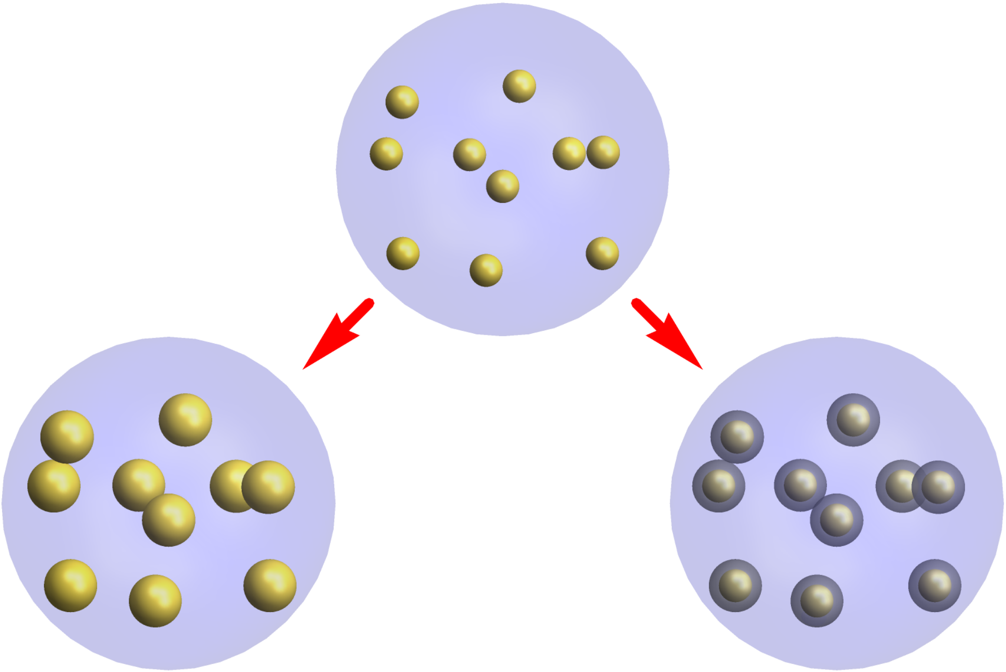

Figure 3.14: Schematic representation of the seeded growth process. Top: initial cluster of gold particles inside the polymer sphere. Left: growth of the gold particles. Right: additional silver layer on top of the gold particles.

Now, a seeded growth method of the encapsulated gold nanoparticles is proposed, in order to increase the filling fraction. We start from polymer spheres with a radius of 60 nm. The sphere contains on average approximately 300 gold particles. The radius of the gold particles was calculated to be 2.7 nm. Several seeded growth methods have been reported already [118–120]. A modified version is used, because the usual reactions would destroy the polymer cluster, or result in a large size distribution of the resulting particles.

The method can be performed with gold salts, to increase the radius of the particles, and, thereby, effectively decreasing the nearest neighbor distance. Alternatively, $AgNO_3$ can be used to cover the gold particles with a silver shell of variable thickness, as shown schematically in Fig. 3.14.

Experimental measurements

In Fig. 3.15 we see the measured spectra corresponding to clusters with different gold particle sizes. The normalized absorption of a solution containing the respective clusters is shown, as well as the scattering response of a single isolated cluster. The response of the original cluster is dominated by the plasmon resonance of the single particles. During the process, the gold particle radii grow from the initial 2.7 nm to 4.0 nm, 4.8 nm, and 5.9 nm, respectively. This amounts to filling fractions of 2.7%, 9.2%, 15.4%, and 28.5%. These values are retrieved from TEM images. As the size of the particles is increased, the coupling between them gets stronger. This causes the

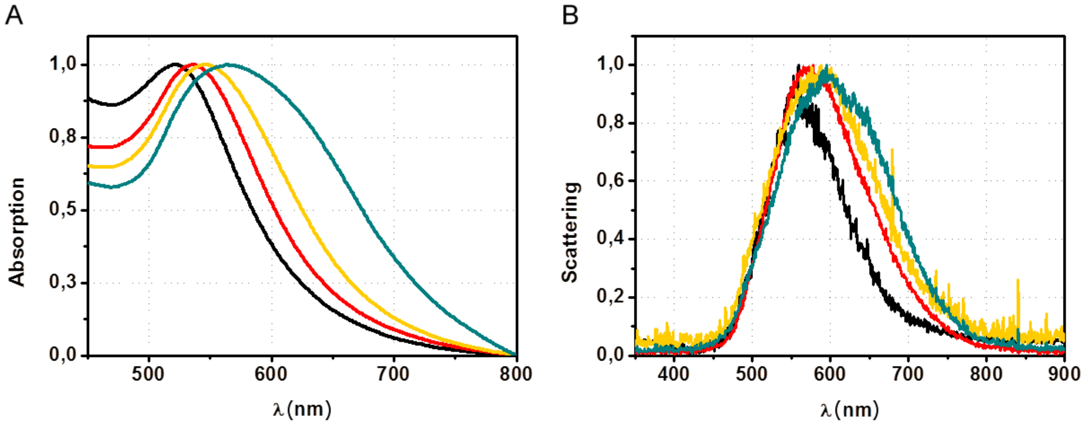

Figure 3.15: (A) Normalized measured absorption spectra of the gold cluster solution and (B) normalized scattering measurements of single clusters. Black: original cluster with particle size 2.7 nm, red: 4.0 nm, yellow: 4.8 nm, and green: 5.9 nm. The single cluster measurements are performed with dark field microscopy.

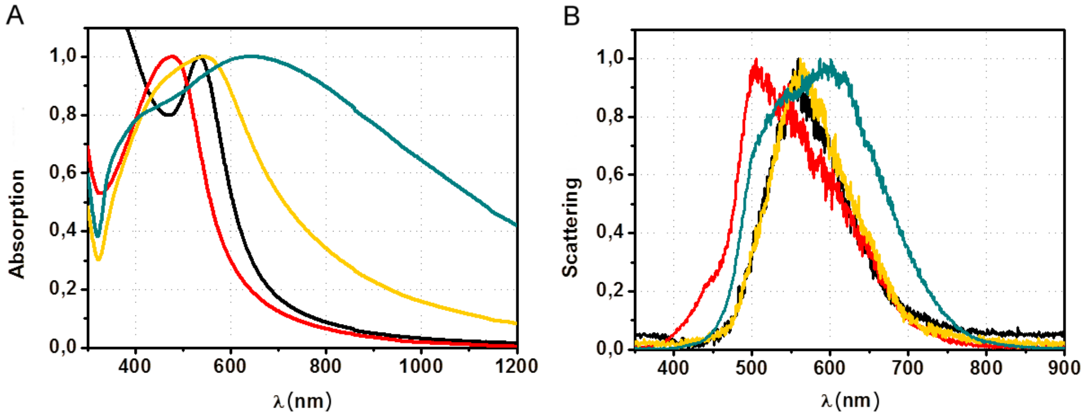

Figure 3.16: (A) Normalized measured absorption spectra of the solution of gold clusters with a silver layer on each gold particle and (B) normalized scattering measurements of single clusters thereof. Black: original cluster with particle size 2.7 nm, red: silver shell with 2.2 nm thickness, yellow: 3.3 nm thickness, and green: 4.7 nm. Note the different behavior, when compared to Fig. 3.15.

resonance position to shift to longer wavelengths. Additionally, we observe a slight broadening of the peak, which can be attributed to a slightly larger size distribution of the particles after the seeded growth procedure. At high filling fractions we observe a shoulder above 600 nm. This is explained by numerical simulations, which we show later.

The alternative way of using the growth process is to incorporate a different material into the cluster. The plasmonic properties can be changed significantly, if a silver layer is introduced on top of the gold particles to form core-shell particles. Again, the growth process can be controlled by altering the concentrations of the reagents.

Thus the silver shell thickness can be varied from 0 nm to 2.2 nm, 3.3 nm, and 4.7 nm, respectively. This amounts to filling fractions of 2.7%, 16.3%, 29.3%, and 56.3%.

In Fig. 3.16 the scattering and absorption of the gold-silver clusters are shown. At low filling fractions, the introduction of silver decreases the resonance wavelength, due to the different plasma frequency of silver. Upon further growth of the shell, we observe again an increase of the resonance wavelength and a strong broadening. The broadening may also arise due to merging of several particles inside the cluster. This can be expected because of the high filling fraction of more than 50%. We also observe that a second resonance appears. We can now conduct Mie simulations to analyze the optical response of the clusters in terms of the contributing multipoles to better understand the underlying cause.

Multipole decomposition

As we have seen in chapter 2, the multipole decomposition can be very helpful to understand the nature of an electromagnetic response. The experimental measurements clearly show the resonance position, but the underlying physics are not easily revealed.

We simulate a cluster of spheres with the multiple scattering method. A maximal multipole order of $N = 2$ is chosen, because the particles are very small compared to the wavelength. The surrounding medium is assumed to have the nondispersive permittivity $\varepsilon_\mathrm{b} = 1.7$. For the metallic particles we use established experimental data [69] with a size correction of the imaginary part. According to the fabrication results, we consider a cluster with a fixed radius of 60 nm, filled with 300 particles. The sizes are varied according to the experimental results.

As we can see in Fig. 3.17, the scattering response of the original cluster with particles with $r = 2.7$ nm is indeed dominated by the resonance of the individual particles, indicated by the black vertical line. As we increase the radius of the gold particles, the interaction gets stronger and, therefore, the resonance shifts to higher wavelengths. This is exactly the same behavior as observed in the experimental measurements.

In the case of the gold clusters, we observe a weaker broadening in the simulations when compared to the measurements. The resonance positions, however, agree very well. For these simulations, we assume the same size for all particles at a given growth stadium. Therefore, we do not observe the stronger broadening of the resonances. Furthermore, we can see that a small magnetic dipole resonance arises for the cluster with stronger coupled particles. This contributes to the shoulder we observed in the experimental measurements.

For the gold-silver core-shell particle cluster, the qualitative behavior reproduces the experimental results very well. The resonance shifts strongly to shorter wavelengths as silver is introduced. This is due to the fact that the resonance of a single silver sphere appears also at shorter wavelengths due to the higher plasma frequency. The response of the gold cores is almost completely suppressed, because the silver shell

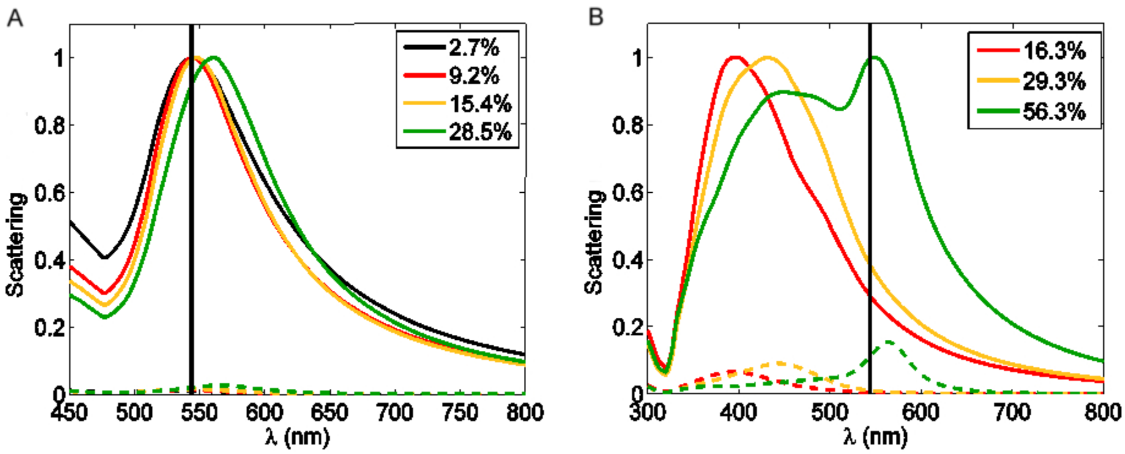

Figure 3.17: (A) Simulated normalized scattering cross section of a cluster of gold nanoparticles of different sizes and (B) for a cluster of gold-silver core-shell particles with varying shell thickness. The black vertical line indicates the position of the plasmon resonance of a single gold particle. The dashed lines show the magnetic dipole contribution to the scattering cross section. The results are in good correspondence to the experimental measurements.

shields the electromagnetic field. For a continuously increasing thickness of the silver shell the peak gradually shifts to the red spectral region, as also seen in the measurements. Most importantly, we also see two distinct resonances, as was also observed in the experimental results.

Now, we use the strength of the multiple Mie method and perform a multipole decomposition of the scattering cross section, as introduced in Eq. 2.28, in the previous chapter. This helps to understand the underlying cause of the additional resonance. All the other peaks are caused by a usual electric dipole resonance. This can be understood easily, because a single metallic sphere can be well approximated by an electric dipole. The peak at longer wavelengths, however, is caused by a collective magnetic dipole resonance of the cluster. The exact position of the resonances deviates slightly from the measurement results. This is likely due to uncertainties in particle sizes and shapes or incomplete silver covering. It is also possible that some particles merged during the seeded growth process. However, the important features are well reproduced.

Conclusion

In summary, we showed a viable method to fabricate metallic nanoparticle clusters with controllable particle sizes. Furthermore, it was shown that gold-silver core-shell particles can be synthesized inside the polymer spheres. With our powerful numerical method at hand, we investigated the scattering response of such clusters and found good agreement with experimental measurements. Most importantly, we could prove that a magnetic dipole resonance occurs. This is much stronger for the core-shell particles, due to the lower absorption and higher metal filling fraction. The presented polymer-metal clusters can serve as building blocks for metamaterials with interesting optical parameters, due to the magnetic response.

3.3 Dynamically tunable metamaterial

For the development of future applied metamaterial technologies, tunability is a crucial requirement [121, 122]. In this section, we want to show the design, fabrication, and characterization of a thermally tunable metamaterial that is fabricated with self-assembly techniques. The proposed material is composed of small silver nanospheres which are covered with and connected by a liquid crystal. This liquid crystal has a strong thermal response, which makes it possible to actively control the arrangement of the silver spheres depending on the temperature. The geometrical change significantly influences the optical response of the material in the optical region.

State-of-the-art self-assembly processes inherently provide isotropic bulk metamaterials. However, they usually end up in a static material, or, even worse, in unwanted changes such as precipitation, clustering, or decay. Here we show the design of a nanoparticle based metamaterial that possesses a tunable optical response in the visible regime [123]. Furthermore, we show that experimental measurements performed by Wiktor Lewandowski and Józef Mieczkowski are in excellent agreement and fully support our numerical calculations, as can be found in Ref. [3], where the results presented in this section were published.

3.3.1 Design and fabrication

The idea of the suggested metamaterial is to have metallic nanoparticles embedded in a liquid crystal matrix that changes its structure reversibly depending on the temperature. This structural change in the liquid crystal material translates to a structural rearrangement of the silver nanoparticles. This rearrangement affects the optical response of the material. At lower temperatures (30 °C), the compound material forms a lamellar structure which we abbreviate as Lm. Here, the nanoparticles are arranged in rectangular layers with well defined inter-layer distance and well defined in-layer distance of the particles inside the layers. At higher temperatures (above 120 °C), however, the material will slightly expand, increasing the particle distance. Furthermore, the ordered distribution of the nanoparticles will break down, resulting in a generally disordered and isotropic distribution, with a different interparticle distance. We abbreviate this isotropic phase as Iso, see Fig. 3.18 for visualizations of these two different phases.

The design is experimentally realized by fabricating coated silver nanoparticles with a radius of 2.35 nm with a modified Wang procedure [124, 125]. Then, a ligand exchange reaction was performed to introduce the liquid crystal molecules into the nanoparticle surface.

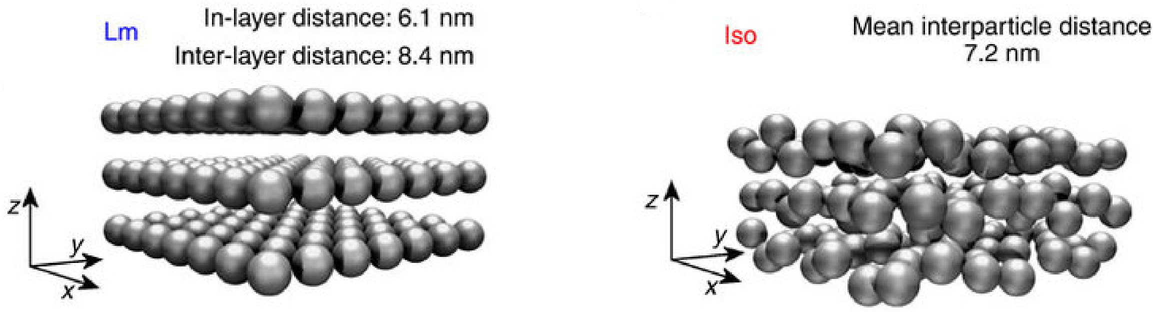

Figure 3.18: Investigated nanoparticle structures. The lamelar structure (Lm) found at lower temperatures is shown on the left side, the right side shows the isotropic structure (Iso) found at high temperatures.

3.3.2 Results

The structure of the self-assembled material is revealed by small angle X-ray diffraction measurements. The results are summarized in Fig. 3.19 A. At high temperatures (120 °C), a diffuse signal is observed, corresponding to an average interparticle distance of 7.2 nm, evidencing an unordered distribution of the nanoparticles. At lower temperatures (30 °C), however, we see multiple sharper rings, suggesting the formation of a long range order. Here, the metal spheres form layers with inter-layer distance of approximately 8.4 nm and a nearest neighbor distance of 6.1 nm within the layer. These findings are confirmed by TEM images (Fig. 3.19 B).

To reveal and understand the properties of such tunable metamaterial from a theoretical perspective, we perform multiscattering simulations with the previously presented Mie algorithm. We model the nanoparticle structures as finite, but sufficiently large patches consisting of small silver spheres with a radius of 2.35 nm. The Lm phase is modeled as a stack of three layers each consisting of 17×17 silver [69] nanoparticles, arranged in a square lattice. We switch to the isotropic structure by slightly increasing the distance of the nanoparticles and shift each particle in a random direction by a random amount, on average 4 nm. This way the effects of heating the structure are represented in a realistic manner. The different geometries are visualized in Fig. 3.18. The number of particles considered, as well as the maximum multipole order in the calculations, are verified to be sufficient to model the material, by checking the convergence of the relevant properties. The liquid crystal in the vicinity of the particles is treated as a homogeneous surrounding medium with a refractive index of $n = 1.6$, an intermediate value for liquid crystal molecules in the solution.

Absorption spectra of the nanoparticle assemblies are simulated using the multisphere scattering algorithm. As can be seen in Fig. 3.20 A, we obtain a single extinction peak, which can be attributed to a collective surface plasmon resonance of the spheres. If we compare the results of the two distinct phases, we observe a significant blue shift when going from the Lm to the Iso phase. The shift amounts to 20 nm, or 30 THz, respectively. The results of the numerical calculations and experimental measurements show very good agreement in the size of the shift

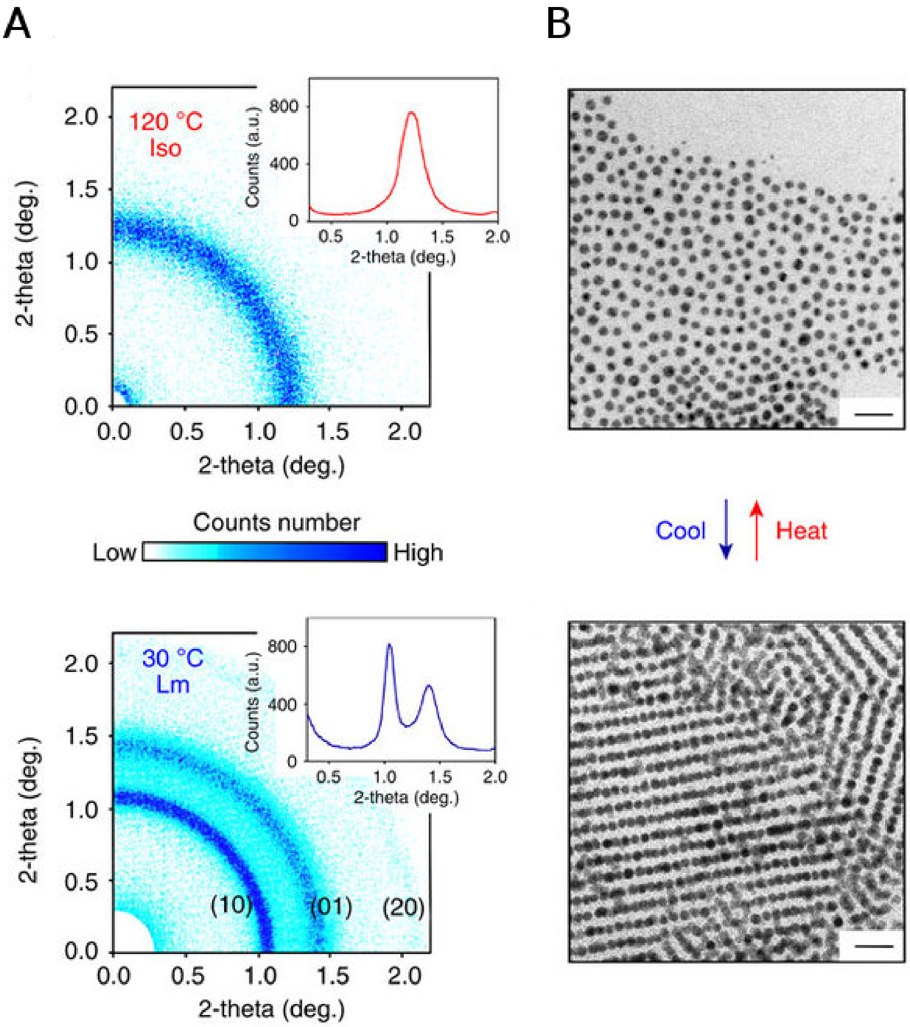

Figure 3.19: Investigated nanoparticle structures. The top row shows the Iso structure found at high temperatures and the bottom row shows the Lm structure found at lower temperatures.
(A) Small angle X-ray diffraction measurements, revealing the geometric structure of the phases. The single broad ring for the Iso phase suggests an isotropic ordering with an average nearest neighbor distance of 7.2 nm. This distance can be deduced from the radius of the ring. The sharper rings corresponding to the Lm phase hint at an ordered geometry. Here, we can deduce the in-layer and inter-layer distances from the radius of the rings to be 6.1 nm and 8.4 nm respectively.
(B) TEM images of the experimental realization. The Iso phase is indeed isotropic while the Lm phase consists of patches with local ordering. The scale bar indicates 20 nm.

and position of the resonances. However, the experimental measurements show a broader resonance. This can be attributed to a slight size distribution of the silver particles. The fabrication and subsequent treatment with the liquid crystal causes an uncertainty of approximately ± 0.3 nm in the particle radius.

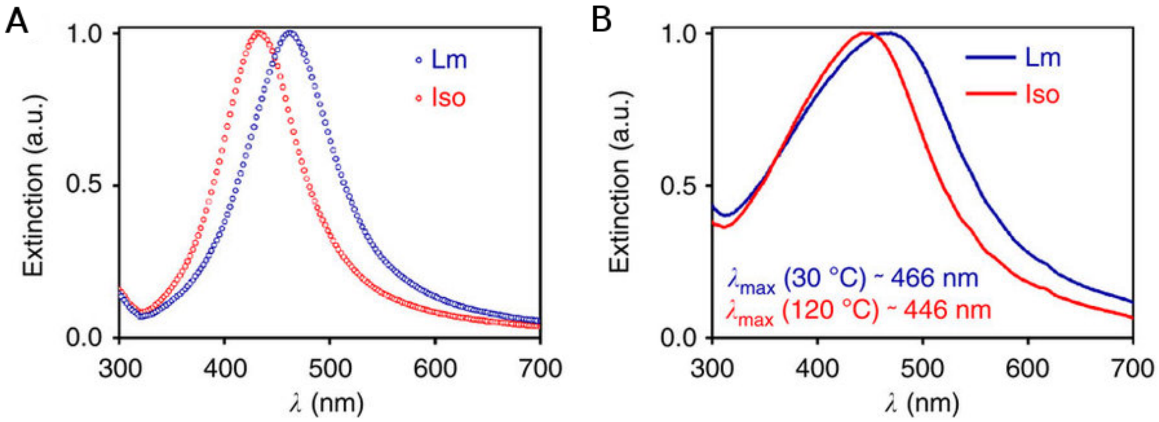

Figure 3.20: Normalized extinction spectra of the numerical calculations (A) and the experimental measurement (B) of the Iso and Lm structures. The low temperature phase Lm is shown in blue and the Iso phase in red. We see a significant resonance shift and a very good agreement in the resonance positions of the measurements and simulations, respectively.

As a reference, we also simulate spectra of an ordered distribution with mean interparticle distance corresponding to the Iso structure (7.2 nm). This results in an optical response almost identical to the unordered Iso geometry. This suggests that the resonance position is dominated by the interparticle distance, rather than just the ordering of the spheres. Vice versa, simulations of a random and an ordered arrangement of spheres with a nearest neighbor distance of 6.1 nm yields also almost identical results, further confirming the hypothesis. However, the interparticle distance changes mainly due to the geometrical reconfiguration, instead of just the thermal expansion. This conclusion is further supported with a control experiment: no shift of the plasmonic resonance position was observed for a heated sample of silver nanoparticles without the liquid crystal coating, for which no structural reconfiguration is observed within the given temperature limit.

It is confirmed by temperature dependent small angle X-ray diffraction measurements that the shift of the plasmon resonance is indeed caused by a reconfiguration of the nanoparticles (Fig. 3.21 A and B). At low temperatures, only the lamellar phase is present, with marginally varying interparticle distance. Then, from 70 °C up to 95 °C the phase change takes place, resulting in a rapid change of the resonance wavelength. At higher temperatures, we observe the expected broad distribution corresponding to the disordered geometry. After this phase transition the resonance wavelength is almost independent of the temperature.

The most interesting aspect of this design is the fact that the transition from Lm to Iso is reversible. This is very important for many dynamically tunable applications. The duration of the full transition lasts a few minutes, but the process can also be sped up to a few seconds. Then, the phase transition is not fully complete, because the material can not react instantaneously to the temperature change. However, a significant resonance shift can be observed as is evident from Fig. 3.21 C, where the resonance shift is shown for an experimental measurement where the temperature

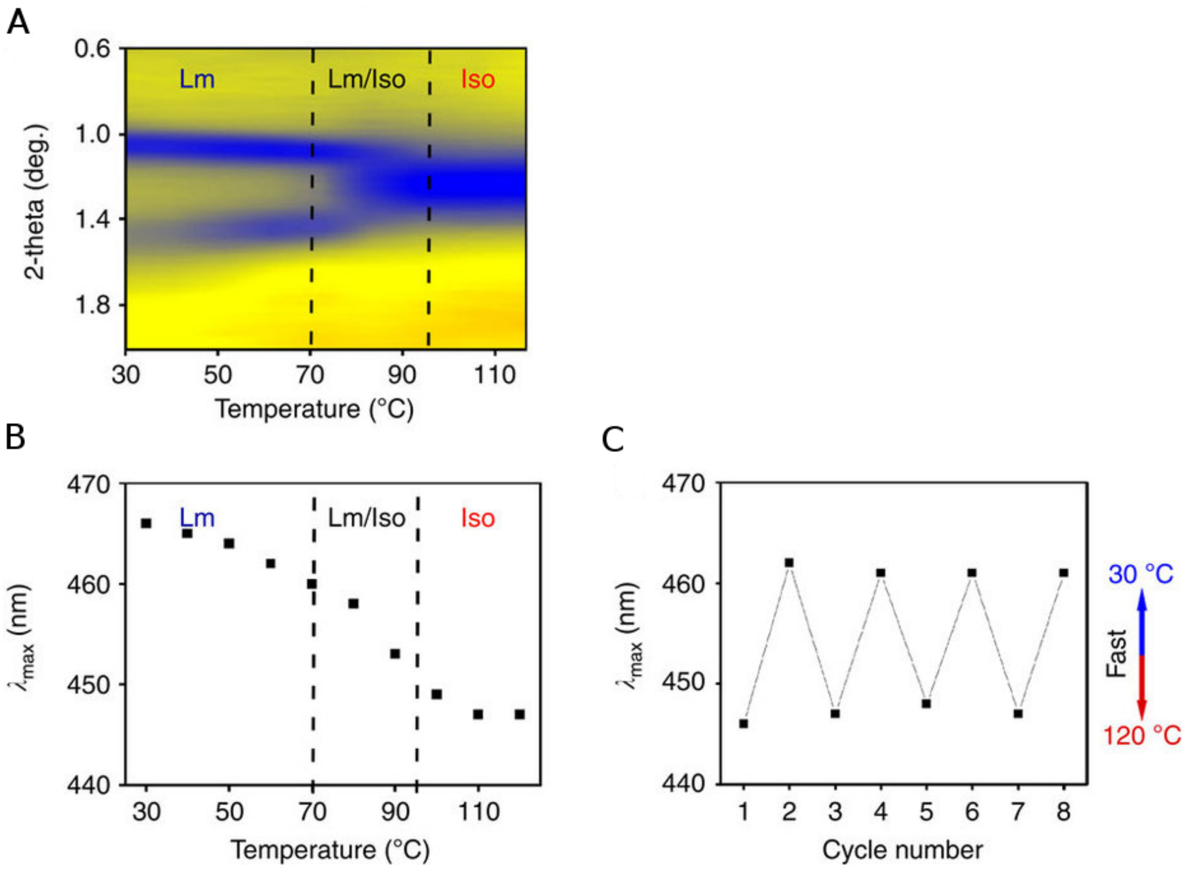

Figure 3.21: Switching behavior of the metamaterial.
(A) Temperature dependent small angle X-ray diffraction measurement showing the phase transition from the ordered Lm phase to the isotropic Iso phase around $80\ ^\circ$C.
(B) Temperature dependent shift of the plasmon resonance position.
(C) Reversible shifting of the resonance position over multiple fast cycles in the order of a few seconds.

was changed in the time frame of a few seconds.

3.3.3 Epsilon-near-zero behavior

Because of the high metal filling fraction in the material we can expect a resonant behavior in the effective permittivity. We calculate the effective permittivity of the two structures with the Clausius-Mossotti relation, Eq. 2.59. Thereby, the polarizability of a single isolated silver sphere is used with the appropriate metal filling fraction. As evidenced in Fig. 3.22, the material shows a Lorentzian resonance in the real part of $\varepsilon_{\text{eff}}(\omega)$, resulting in an epsilon-near-zero behavior in a finite spectral region. The change from Lm to Iso causes a decrease of the filling fraction, because the distances of the spheres increase. This is also reflected in the resonance position of $\varepsilon_{\text{eff}}(\omega)$. Thus, the material has actively tunable optical properties.

In order to verify these results, we use a complementary method to obtain the effective permittivity of the material. The complex reflection $r(\omega)$ and transmission $t(\omega) = t'(\omega)\mathrm{e}^{-\mathrm{i}kd}$ coefficients of an infinitely extended layer with finite thickness d, composed of nanospheres are calculated. Here, we use the finite element solver JCMsuite [126]. From the reflection and transmission coefficients we can retrieve the effective permittivity as [127]

$$n_{\text{eff}}(\omega) = \pm \frac{\arccos\left(\frac{1}{2t'(\omega)}[1 - r^2(\omega) + t'^2(\omega)]\right)}{kd} + \frac{2\pi m}{kd}, \tag{3.2}$$

$$Z_{\text{eff}}(\omega) = \pm \sqrt{\frac{[1 - r(\omega)]^2 - t'^2(\omega)}{[1 - r(\omega)]^2 - t'^2(\omega)}}, \tag{3.3}$$

$$\varepsilon_{\text{eff}}(\omega) = \frac{n_{\text{eff}}(\omega)}{Z_{\text{eff}}(\omega)}, \tag{3.4}$$

where m is an integer, corresponding to the respective branch of the effective refractive index $n_{\text{eff}}(\omega)$. We need to take care on the sign of the effective refractive index

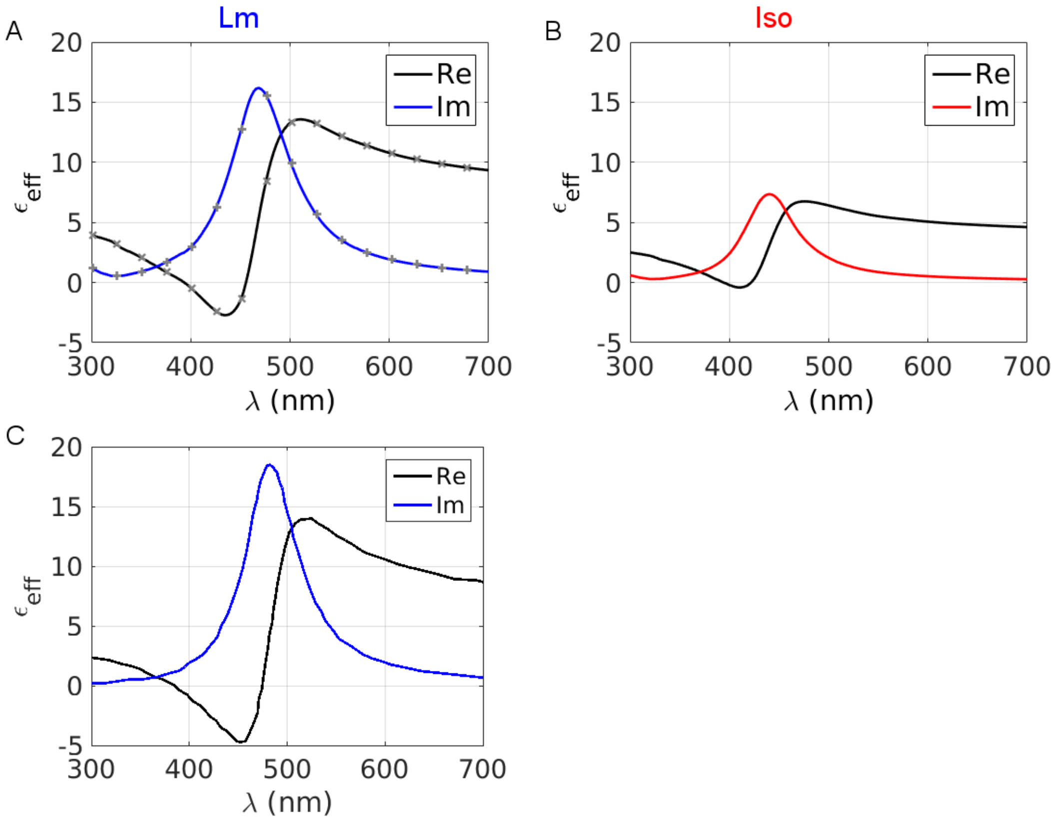

Figure 3.22: Wavelength dependent effective permittivity of the material. (A) $\varepsilon_{\text{eff}}(\omega)$ of the Lm structure obtained from the Clausius-Mossotti relation. The crosses depict the solution as obtained from the reflection and transmission coefficients. (B) $\varepsilon_{\text{eff}}(\omega)$ of the Iso structure obtained from the Clausius-Mossotti relation. (C) Experimental result obtained via ellipsometry.

and the impedance $Z_{\text{eff}}(\omega)$. We choose the sign in order to ensure a positive solution for the imaginary part of $\varepsilon_{\text{eff}}(\omega)$.

We assume three layers of rectangular lattices with the distances corresponding to the measurement results. The Lm phase is modeled with a in-layer distance of 6.1 nm and an interlayer distance of 8.4 nm (like it is shown in Fig. 3.18).

The results of the two complementary techniques agree extremely well, as can be seen in Fig. 3.22 A. Additionally, there is excellent agreement between calculated data and experimental measurements retrieved with ellipsometry, shown in Fig. 3.22 C. More details on the ellipsometric measurements can be found in the supporting information of Ref. [3].

Because we are exploiting the resonant behavior of the material, the dispersion of the real part of $\varepsilon_{\text{eff}}(\omega)$ is accompanied by a large imaginary part, potentially causing strong absorption. A reasonable figure of merit to quantify this absorption is [128]

$$FOM(\omega) = \frac{\mathrm{R}e[n_{\text{eff}}(\omega)]}{2\,\mathrm{I}m[n_{\text{eff}}(\omega)]}. \tag{3.5}$$

$FOM(\omega)$ expresses the propagation length of light in the material in units of wavelengths. Values ranging from $FOM = 0.4$ to $FOM = 1.2$ are retrieved for the window $-1 \leq \mathrm{R}e[\varepsilon_{\text{eff}}(\omega)] \leq 1$. This confirms that light propagation in this epsilon-near-zero regime is possible.

3.3.4 Conclusion

We presented the design of a material with significant tunability of its optical properties through thermal manipulation. Notably, the resonances lie within the optical part of the spectrum. Furthermore, the high metal filling fraction results in interesting metamaterial properties in the form of epsilon-near-zero behavior.

We created an actively tunable epsilon-near-zero metamaterial in the optical regime via dynamic self-assembly and underpinned the viability by demonstrating a very good agreement between experimental results and numerical calculations.

An important feature for possible applications is the robust reversibility of the active tuning within short time frames.

A possible route to improve this design is to further minimize the interparticle distances. This can be achieved by novel ligands, forming the liquid crystal, with smaller geometric extensions of the metal particles, or by decreasing the relative gap size by increasing the metallic nanoparticles to several tens of nanometers.

4 T-matrix formalism for arbitrarily shaped particles

In chapter 2 we established a framework for the calculation of the scattering coefficients of single spheres and clusters of spheres. We showed in chapter 3 that there are many interesting applications that consider artificial materials composed of particles with spherical shape. The discussion and consideration of such particles constitutes an active field of research. However, in order to achieve strong resonances and high tunability, we often need to consider more complexly shaped particles, like split ring resonators or particles made of coupled nanopatches [83]. Furthermore, some unique interesting effects can only be realized with very sophisticated objects such as helices [7]. To study the properties of such materials, computational tools need to be available that allow exploring the interaction of light with an ensemble of such complexly shaped particles.

In this chapter, we present a T-matrix algorithm, suitable to calculate the scattering by clusters of arbitrarily shaped particles. Such a computation requires as an initial step the calculation of the actual T-matrix of the object under consideration.

First, we demonstrate how to derive the T-matrix of a cluster of spheres. The chosen method is based on the multiple scattering algorithm for spheres that was presented in chapter 2. Afterwards, a more general approach to calculate the T-matrix is presented. In this approach, general objects with an arbitrary geometry and composed from arbitrary materials can be considered. The object is illuminated by several plane waves and the scattered field is calculated with established finite element solvers [126]. We can calculate the scattering coefficients for each incident plane wave from the scattered fields. Once we combine the outcome from all these computations, we can obtain the T-matrix as a final result.

Afterwards, we provide two numerical examples in the form of interesting objects whose T-matrix is calculated to demonstrate the validity and usefulness of the method. The main purpose of these examples is to investigate the convergence of the T-matrix calculation method. Furthermore, we show that knowing the T-matrix is not only important for scattering calculations, it provides also valuable information about other properties and symmetries of the considered object.

Finally, we present a multi scattering algorithm, which is suitable for the simulation of the scattering by multiple arbitrary objects with known T-matrix. The method is an extension to the multi scattering formalism for spheres, which was described in chapter 2. Now, instead of the analytically known Mie coefficients of the spheres, we need the full T-matrix of the objects. The T-matrix of the constituting objects needs to be calculated beforehand with the methods shown in this chapter. This constitutes a powerful tool to calculate the optical response of an arbitrary, but finite distribution of general objects. We build upon this foundation in the following chapter 5, where we use the formalism to investigate complicated metaatoms.

As already indicated in section 2.1.2, the T-matrix of a single sphere is given by the Mie coefficients on the diagonal. For arbitrary objects, however, the T-matrix is generally dense. The T-matrix is the link between scattering and illumination coefficients according to the relation

$$\begin{pmatrix}\mathbf{a}(\omega)\\ \mathbf{b}(\omega)\end{pmatrix} = \mathbf{T}(\omega)\cdot\begin{pmatrix}\mathbf{p}(\omega)\\ \mathbf{q}(\omega)\end{pmatrix}. \tag{4.1}$$

Here, $\mathbf{a}(\omega)$ and $\mathbf{b}(\omega)$ are concatenated vectors that contain the coefficients used to expand the scattered field and $\mathbf{p}(\omega)$ and $\mathbf{q}(\omega)$ are concatenated vectors containing the coefficients of the incident field. The coefficients are introduced in Eqs. 2.17 and 2.19 in chapter 2.

The T-matrix consists of the following submatrices

$$\mathbf{T}(\omega) = \begin{pmatrix}\mathbf{T}^{\mathrm{ee}}(\omega) & \mathbf{T}^{\mathrm{em}}(\omega)\\ \mathbf{T}^{\mathrm{me}}(\omega) & \mathbf{T}^{\mathrm{mm}}(\omega)\end{pmatrix}, \tag{4.2}$$

where $\mathbf{T}_{\mathrm{ee}}(\omega)$ describes coupling of electric incident modes to electric scattered modes, $\mathbf{T}_{\mathrm{mm}}(\omega)$ describes the magnetic coupling, and the other submatrices express coupling of electric and magnetic modes, respectively. In a similar way, these individual entries of the T-matrix can be ordered to highlight the coupling among the multipolar modes

$$\mathbf{T}^{\mathrm{ee}}(\omega) = \begin{pmatrix}\mathbf{T}^{\mathrm{ee}}_{11}(\omega) & \mathbf{T}^{\mathrm{ee}}_{12}(\omega) & \cdots\\ \mathbf{T}^{\mathrm{ee}}_{21}(\omega) & \mathbf{T}^{\mathrm{ee}}_{22}(\omega) & \\ \vdots & & \ddots\end{pmatrix}, \tag{4.3}$$

here, $\mathbf{T}^{\mathrm{ee}}_{n\nu}(\omega)$ is the submatrix that represents the coupling of order ν of the incident field to the order n of the scattered field. For a sphere, $\mathbf{T}^{\mathrm{ee}}_{11}(\omega)$ would contain the first Mie coefficient $a_1(\omega)$ on the diagonal, $\mathbf{T}_{22}(\omega)$ the second and so on, to reproduce Eq. 2.21. As we see from Eq. 4.3 the T-matrix requires to be infinitely large to describe an object correctly. Similarly to the multiple Mie scattering formalism in chapter 2, we truncate the T-matrix at a finite size, corresponding to a maximum multipolar order N, which we take into account. This is justified as long as it can be assumed that higher orders do not have a notable contribution to the scattering response.

4.1 T-matrix of clusters of spheres

Now, we show a method to calculate the T-matrix of a cluster of spheres. By doing so, we can potentially save a lot of computational resources. If we want to simulate an arrangement of multiple equal clusters, we only need to calculate the T-matrix of the single structure once and use the same T-matrix for each object. This concept is shown in detail in section 4.4.

For the purpose of calculating the T-matix of a cluster of spheres, let us reconsider the main equation of section 2.1.2 to calculate the scattering coefficients of a cluster of spheres

$$\begin{aligned} a^j_{nm}(\omega) &= a^j_n(\omega)\left\{p^{j,j}_{nm}(\omega) - \sum_{l\neq j}\sum_{\nu=1}^{\infty}\sum_{\mu=-\nu}^{\nu}\left[a^l_{\nu\mu}(\omega)A^{\nu\mu}_{nm}(\mathbf{d}_{lj},\omega) + b^l_{\nu\mu}(\omega)B^{\nu\mu}_{nm}(\mathbf{d}_{lj},\omega)\right]\right\}, \\ b^j_{nm}(\omega) &= b^j_n(\omega)\left\{q^{j,j}_{nm}(\omega) - \sum_{l\neq j}\sum_{\nu=1}^{\infty}\sum_{\mu=-\nu}^{\nu}\left[a^l_{\nu\mu}(\omega)B^{\nu\mu}_{nm}(\mathbf{d}_{lj},\omega) + b^l_{\nu\mu}(\omega)A^{\nu\mu}_{nm}(\mathbf{d}_{lj},\omega)\right]\right\}. \end{aligned} \tag{4.4}$$

We can write this system of equations in a more elegant matrix formulation

$$\begin{pmatrix} \begin{pmatrix}\mathbf{a}(\omega)\\ \mathbf{b}(\omega)\end{pmatrix}^{(1)} \\ \vdots \\ \begin{pmatrix}\mathbf{a}(\omega)\\ \mathbf{b}(\omega)\end{pmatrix}^{(j)} \\ \vdots \\ \begin{pmatrix}\mathbf{a}(\omega)\\ \mathbf{b}(\omega)\end{pmatrix}^{(J)} \end{pmatrix} = \mathbf{M}(\omega)\cdot \begin{pmatrix} \begin{pmatrix}\mathbf{p}(\omega)\\ \mathbf{q}(\omega)\end{pmatrix}^{(1)} \\ \vdots \\ \begin{pmatrix}\mathbf{p}(\omega)\\ \mathbf{q}(\omega)\end{pmatrix}^{(j)} \\ \vdots \\ \begin{pmatrix}\mathbf{p}(\omega)\\ \mathbf{q}(\omega)\end{pmatrix}^{(J)} \end{pmatrix}. \tag{4.5}$$

Here, $\begin{pmatrix}\mathbf{a}(\omega)\\ \mathbf{b}(\omega)\end{pmatrix}^{(j)}$ and $\begin{pmatrix}\mathbf{p}(\omega)\\ \mathbf{q}(\omega)\end{pmatrix}^{(j)}$ are vectors of coefficients, corresponding to the individual sphere j of the cluster. The matrix $\mathbf{M}(\omega)$ contains the Mie coefficients, $a^j_n(\omega)$ and $b^j_n(\omega)$ of each sphere and translation coefficients, $A^{\nu\mu}_{nm}(\mathbf{d}_{lj},\omega)$ and $B^{\nu\mu}_{nm}(\mathbf{d}_{lj},\omega)$, corresponding to the position of the respective sphere. We notice already a strong resemblance to the T-matrix equation 4.1, but one last step is still missing. The coefficients need to provide an expansion with respect to the central coordinates instead of individual coordinate systems for each sphere. At the end the T-matrix shall describe the response of the entire object with respect to its central coordinate and not the individual contributions. For this purpose, we need to transform the coefficients with suitably chosen translation matrices $\mathbf{U}(\omega)$ for the scattering coefficients and $\mathbf{V}(\omega)$ for the illumination coefficients, such that

$$\mathbf{U}(\omega)\cdot \begin{pmatrix} \begin{pmatrix}\mathbf{a}(\omega)\\ \mathbf{b}(\omega)\end{pmatrix}^{(1)} \\ \vdots \\ \begin{pmatrix}\mathbf{a}(\omega)\\ \mathbf{b}(\omega)\end{pmatrix}^{(j)} \\ \vdots \\ \begin{pmatrix}\mathbf{a}(\omega)\\ \mathbf{b}(\omega)\end{pmatrix}^{(J)} \end{pmatrix} = \begin{pmatrix}\mathbf{a}(\omega)\\ \mathbf{b}(\omega)\end{pmatrix} \quad \text{and} \quad \mathbf{V}(\omega)\cdot \begin{pmatrix} \begin{pmatrix}\mathbf{p}(\omega)\\ \mathbf{q}(\omega)\end{pmatrix}^{(1)} \\ \vdots \\ \begin{pmatrix}\mathbf{p}(\omega)\\ \mathbf{q}(\omega)\end{pmatrix}^{(j)} \\ \vdots \\ \begin{pmatrix}\mathbf{p}(\omega)\\ \mathbf{q}(\omega)\end{pmatrix}^{(J)} \end{pmatrix} = \begin{pmatrix}\mathbf{p}(\omega)\\ \mathbf{q}(\omega)\end{pmatrix}. \tag{4.6}$$

These rectangular translation matrices contain the translation coefficients. Their entries can be derived from Eq. 2.40. If we insert the identities $\mathbf{U}^{-1}(\omega)\cdot\mathbf{U}(\omega)$ and $\mathbf{V}^{-1}(\omega)\cdot\mathbf{V}(\omega)$ into Eq. 4.5, we arrive at Eq. 4.1, i.e., the T-matrix of the whole cluster

$$\begin{aligned}
\mathbf{U}^{-1}(\omega)\cdot\mathbf{U}(\omega)\cdot\begin{pmatrix}\begin{pmatrix}\mathbf{a}(\omega)\\\mathbf{b}(\omega)\end{pmatrix}^{(1)}\\ \vdots \\ \begin{pmatrix}\mathbf{a}(\omega)\\\mathbf{b}(\omega)\end{pmatrix}^{(j)}\\ \vdots \\ \begin{pmatrix}\mathbf{a}(\omega)\\\mathbf{b}(\omega)\end{pmatrix}^{(J)}\end{pmatrix} &= \mathbf{M}(\omega)\cdot\mathbf{V}^{-1}(\omega)\cdot\mathbf{V}(\omega)\cdot\begin{pmatrix}\begin{pmatrix}\mathbf{p}(\omega)\\\mathbf{q}(\omega)\end{pmatrix}^{(1)}\\ \vdots \\ \begin{pmatrix}\mathbf{p}(\omega)\\\mathbf{q}(\omega)\end{pmatrix}^{(j)}\\ \vdots \\ \begin{pmatrix}\mathbf{p}(\omega)\\\mathbf{q}(\omega)\end{pmatrix}^{(J)}\end{pmatrix} \qquad (4.7)\\
\begin{pmatrix}\mathbf{a}(\omega)\\\mathbf{b}(\omega)\end{pmatrix} &= \mathbf{U}(\omega)\cdot\mathbf{M}(\omega)\cdot\mathbf{V}^{-1}(\omega)\cdot\begin{pmatrix}\mathbf{p}(\omega)\\\mathbf{q}(\omega)\end{pmatrix} \qquad (4.8)\\
\begin{pmatrix}\mathbf{a}(\omega)\\\mathbf{b}(\omega)\end{pmatrix} &= \mathbf{T}(\omega)\cdot\begin{pmatrix}\mathbf{p}(\omega)\\\mathbf{q}(\omega)\end{pmatrix}.
\end{aligned}$$

The inverse matrices $\mathbf{U}^{-1}(\omega)$ and $\mathbf{V}^{-1}(\omega)$ can be obtained by considering the inverse translation (from the central coordinate system to the individual systems). Thus, we can calculate the T-matrix using only the Mie coefficients of the constituting spheres and translation coefficients to get

$$\mathbf{T}(\omega)=\mathbf{U}(\omega)\cdot\mathbf{M}(\omega)\cdot\mathbf{V}^{-1}(\omega). \qquad (4.9)$$

Note that this is a semi-analytic solution. We use the analytically known Mie coefficients of each sphere and the translation coefficients to account for their respective position. Note also that, in order to perform simulations, we need to truncate the T-matrix at a finite multipole order N. Then, even though the Mie coefficients for a single sphere are exact up to the considered multipole order, the resulting T-matrix has some additional inaccuracies, introduced by the translation coefficients with finite order N.

4.2 T-matrix of an arbitrarily shaped particle

To perform simulations and to analyze a given object with complicated geometry, we need to calculate its T-matrix numerically. Several established methods to calculate the T-matrix have been reported. The first method is the extended boundary condition method, originally introduced by Waterman [65, 129, 130]. However, only homogeneous particles can be considered and the method is quite time and resource consuming. An extension to this method is the point matching method [131, 132]. There, the coefficients of the incident, scattered, and internal fields are related, but without the expensive surface integrations needed for the extended boundary condition method. Another strategy to compute the T-matrix of an arbitrary object is to excite it with pure vector spherical harmonic functions to extract exactly one line of the T-matrix per illumination [133]. In this latter reference, the fields were calculated with an integral equation solver. That method has the advantage that the incident field can be expressed in an exact way with a single incident coefficient. But the actual implementation of such an illumination with available tools is cumbersome.

Here, we present a method that is easy to implement numerically and, depending on the applied Maxwell solver, potentially very efficient. The work presented in this section has already been presented in reference [10]. This manuscript is currently in the referee process.

In the analysis, the object is considered to be illuminated with several different plane waves in individual simulations. From each simulation the expansion coefficients of the scattered field are extracted by projecting it onto vector spherical harmonic functions $\mathbf{N}^{(l)}_{nm}(\mathbf{r},\omega)$ and $\mathbf{M}^{(l)}_{nm}(\mathbf{r},\omega)$. To get the scattered field of the object for every plane wave, however, we need an additional tool that solves Maxwell's equations for an arbitrary object under plane wave illumination. Such tools are widely available. We chose here the finite element solver JCMsuite [126], because it is especially fast for the simulation of several different illuminations of an object at the same frequency.

The scattering coefficients can be obtained from the numerically calculated scattered fields $\mathbf{E}_{\text{sca}}(\mathbf{r},\omega)$ by

$$\begin{aligned} a_{nm}(\omega) &= \frac{\int_0^{2\pi}\int_0^{\pi}\mathbf{E}_{\text{sca}}(|\mathbf{r}|=R,\omega)\,\left[\mathbf{N}^{(3)}_{nm}(|\mathbf{r}|=R,\omega)\right]^*\sin\theta\,\mathrm{d}\theta\mathrm{d}\phi}{\int_0^{2\pi}\int_0^{\pi}|\mathbf{N}^{(3)}_{nm}(|\mathbf{r}|=R,\omega)|^2\sin\theta\,\mathrm{d}\theta\mathrm{d}\phi}\,, \\ b_{nm}(\omega) &= \frac{\int_0^{2\pi}\int_0^{\pi}\mathbf{E}_{\text{sca}}(|\mathbf{r}|=R,\omega)\,\left[\mathbf{M}^{(3)}_{nm}(|\mathbf{r}|=R,\omega)\right]^*\sin\theta\,\mathrm{d}\theta\mathrm{d}\phi}{\int_0^{2\pi}\int_0^{\pi}|\mathbf{M}^{(3)}_{nm}(|\mathbf{r}|=R,\omega)|^2\sin\theta\,\mathrm{d}\theta\mathrm{d}\phi}\,, \end{aligned} \tag{4.10}$$

and similarly the incident coefficients

$$\begin{aligned} p_{nm}(\omega) &= \frac{\int_0^{2\pi}\int_0^{\pi}\mathbf{E}_{\text{inc}}(|\mathbf{r}|=R,\omega)\,\left[\mathbf{N}^{(1)}_{nm}(|\mathbf{r}|=R,\omega)\right]^*\sin\theta\,\mathrm{d}\theta\mathrm{d}\phi}{\int_0^{2\pi}\int_0^{\pi}|\mathbf{N}^{(1)}_{nm}(|\mathbf{r}|=R,\omega)|^2\sin\theta\,\mathrm{d}\theta\mathrm{d}\phi}\,, \\ q_{nm}(\omega) &= \frac{\int_0^{2\pi}\int_0^{\pi}\mathbf{E}_{\text{inc}}(|\mathbf{r}|=R,\omega)\,\left[\mathbf{M}^{(1)}_{nm}(|\mathbf{r}|=R,\omega)\right]^*\sin\theta\,\mathrm{d}\theta\mathrm{d}\phi}{\int_0^{2\pi}\int_0^{\pi}|\mathbf{M}^{(1)}_{nm}(|\mathbf{r}|=R,\omega)|^2\sin\theta\,\mathrm{d}\theta\mathrm{d}\phi}\,. \end{aligned} \tag{4.11}$$

Note, that the fields are evaluated at a virtual sphere of fixed radius R that completely encloses the object. Analytically, the chosen radius has no influence on the result. In numerical realizations, however, the choice could effect the result, due to the finite sampling. It is advisable to use a small R, to keep the computational domain small, without touching the actual object.

For an illumination with a plane wave, however, the coefficients can be calculated analytically as shown in section 2.1 and a numerical evaluation of the integrals 4.11 is not necessary.

Now, we can calculate a set of $\begin{pmatrix}\mathbf{p}(\omega)\\ \mathbf{q}(\omega)\end{pmatrix}^k$ and corresponding $\begin{pmatrix}\mathbf{a}(\omega)\\ \mathbf{b}(\omega)\end{pmatrix}^k$ for each illumination k. Then, we construct a system of equations to calculate the T-matrix $\mathbf{T}_K$ numerically with K illuminations

$$\left(\begin{pmatrix}\mathbf{a}(\omega)\\ \mathbf{b}(\omega)\end{pmatrix}^1 \begin{pmatrix}\mathbf{a}(\omega)\\ \mathbf{b}(\omega)\end{pmatrix}^2 \cdots \begin{pmatrix}\mathbf{a}(\omega)\\ \mathbf{b}(\omega)\end{pmatrix}^K\right) = \mathbf{T}_K(\omega)\cdot\left(\begin{pmatrix}\mathbf{p}(\omega)\\ \mathbf{q}(\omega)\end{pmatrix}^1 \begin{pmatrix}\mathbf{p}(\omega)\\ \mathbf{q}(\omega)\end{pmatrix}^2 \cdots \begin{pmatrix}\mathbf{p}(\omega)\\ \mathbf{q}(\omega)\end{pmatrix}^K\right). \tag{4.12}$$

We invert this system to find the T-matrix according to

$$\mathbf{T}_K(\omega) = \left(\begin{pmatrix}\mathbf{a}(\omega)\\ \mathbf{b}(\omega)\end{pmatrix}^1 \begin{pmatrix}\mathbf{a}(\omega)\\ \mathbf{b}(\omega)\end{pmatrix}^2 \cdots \begin{pmatrix}\mathbf{a}(\omega)\\ \mathbf{b}(\omega)\end{pmatrix}^K\right)\cdot\left(\begin{pmatrix}\mathbf{p}(\omega)\\ \mathbf{q}(\omega)\end{pmatrix}^1 \begin{pmatrix}\mathbf{p}(\omega)\\ \mathbf{q}(\omega)\end{pmatrix}^2 \cdots \begin{pmatrix}\mathbf{p}(\omega)\\ \mathbf{q}(\omega)\end{pmatrix}^K\right)^{-1}. \tag{4.13}$$

In order to get an invertible matrix, we need to calculate the response from K illuminations, where K is equal to or greater than the rank d of the T-matrix. This rank depends on the multipole order N we take into account

$$K \geq d = 2N(N+2). \tag{4.14}$$

Using more illuminations is not strictly necessary, but will improve the accuracy of the result, as we see in the following examples. Even though we get more equations, the system is not overdetermined. The additional equations are in principle linear combinations of known equations, thus, they help in reducing the numerical noise. The inversion of the rectangular matrix can be performed for example with QR decomposition [134]. Note that the resulting T-matrix is always a square matrix in our formalism.

4.3 Numerical examples

In this section, we show that the method delivers reliable results, by investigating two simple example objects. We show that the T-matrix gives further insights into the scattering mechanisms of these objects.

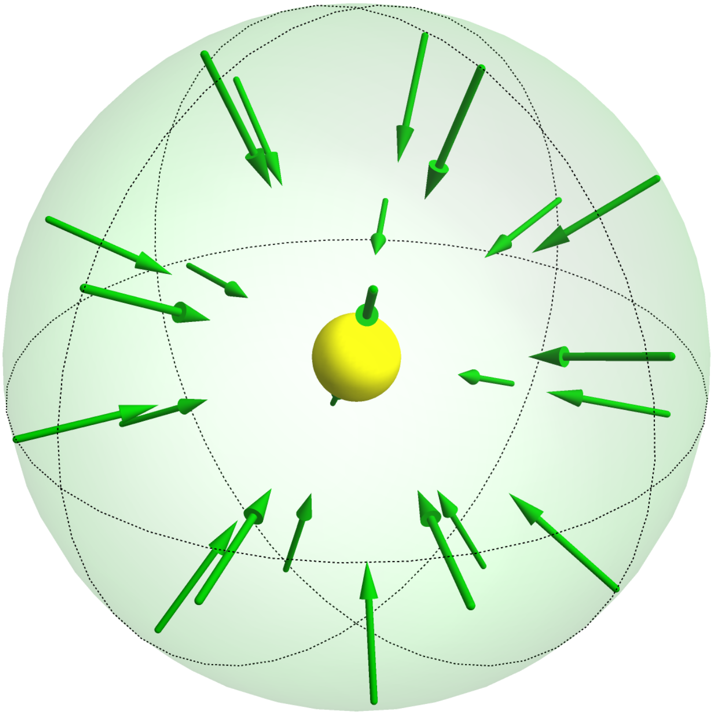

Figure 4.1: Single sphere with multiple plane wave illuminations, depicted with their wave vectors in green. The green spherical region illustrates that the waves are incident isotropically.

4.3.1 Single sphere

As a first check to prove that the method delivers correct results, we investigate the most simple object: a single isolated sphere. The example is chosen, because we have the correct analytical solution for a single sphere available. The T-matrix has only the analytically known Mie-coefficients on the diagonal and all other entries are zero.

Let us consider a dielectric sphere with a radius of 100 nm and a relative permittivity of 16 in vacuum. The Mie-coefficients of this sphere for the first two orders are non-negligible at 600 THz, as can be confirmed by Eq. 2.24. Such a high permittivity sphere is of interest since it sustains a notable electric and magnetic dipole moment in the visible spectrum without absorption, which is usually tied to plasmonic objects.

We illuminate the sphere with the appropriate number of plane waves K to calculate the T-matrix numerically. The wave vectors are chosen, such that they are evenly distributed in all directions. They can intuitively be considered as normal vectors of the surface of an imaginary sphere. They are distributed with the equal nearest neighbor distance to cover all directions, as is shown in Fig. 4.1. The polarization of the electric field is then chosen randomly for each wave.

To check the convergence of our method, we increase the number of illuminations used to calculate the T-matrix and investigate the behavior of the numerical error.

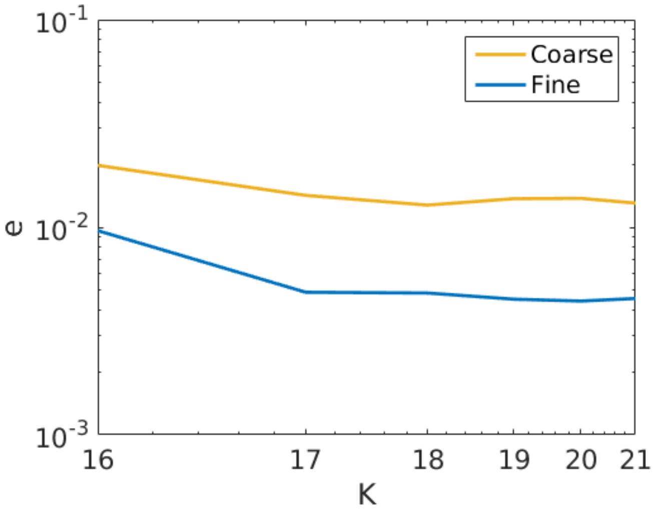

Figure 4.2: Convergence of the T-matrix calculation with the increase of the number of plane wave illuminations K. The minimum number of illuminations to solve for all the unknown entries of the T-matrix for the multipole order $N = 2$ is 16. The error e is shown for two different calculations, where the fine one has two times finer meshing.

We introduce

$$e(K) = \sqrt{\frac{\sum_i |\mathbf{T}_{\text{Mie}}(i) - \mathbf{T}_K(i)|^2}{\sum_i |\mathbf{T}_{\text{Mie}}(i)|^2 + |\mathbf{T}_K(i)|^2}} \tag{4.15}$$

as a measure for the deviation of the T-matrix from the analytically known solution. Here, (i) is an index that runs over all matrix components. This quantity is visualized in Fig. 4.2 in a logarithmic plot.

We observe that the analytic T-matrix can be reproduced with reasonably sufficient precision. The deviation drops for an increasing number of illuminations until a plateau is reached. The remaining deviation can be explained by numerical errors introduced by the finite meshing of the sphere in the Maxwell solver. This is confirmed by considering a second calculation with a finer mesh. The result shows the same characteristic behavior, but a better precision can be reached. Hence, we can basically reach an arbitrary precision by choosing the appropriate number of illuminations and meshing of the finite element solver.

4.3.2 Dimer

We now consider a slightly more complex object to further investigate the convergence of the proposed method. The dimer, similar to the one investigated in section 3.2.1, is a suitable example, because we can calculate the T-matrix semi-analytically as a reference. We get the T-matrix of the single spheres directly from the Mie coefficients and construct the total T-matrix by translating the coefficients

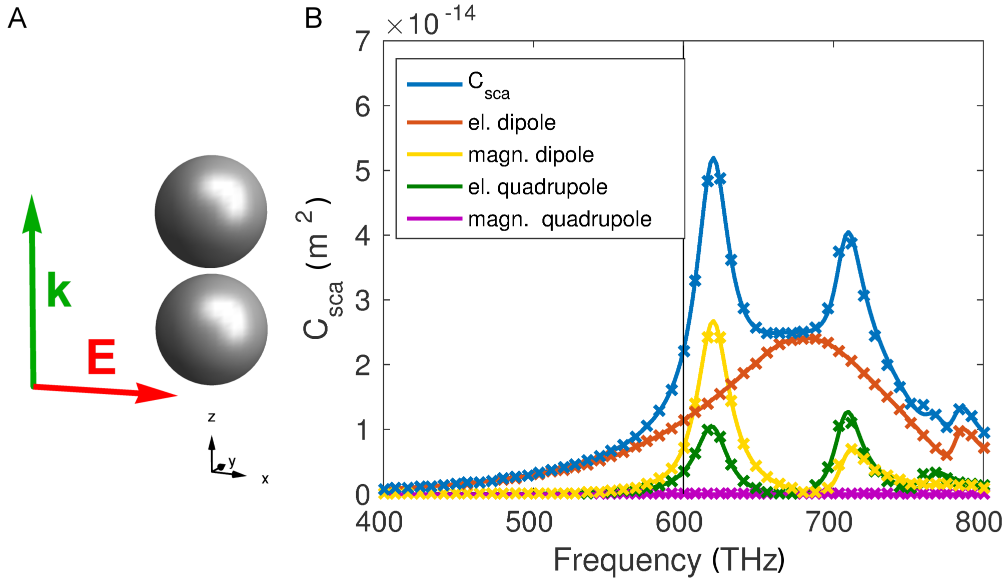

Figure 4.3: (A) Geometry and illumination direction of the dimer setup. (B) Total scattering cross section (blue) of the dimer and the contributions of different multipoles. The solid lines correspond to the semi-analytical calculation based on the Mie coefficients of the spheres and the crosses correspond to the calculation with the FEM solver. We observe an excellent visual agreement. The black vertical line shows the spectral position that is used for further calculations to show the T-matrix entries. 10 additional plane wave illuminations were used for the numerical T-matrix calculation.

with addition theorems as outlined in section 4.1. Additionally, we calculate the T-matrix from the illumination with plane waves with the proposed method, according to Eq. 4.13, and compare the results.

The object we investigate consists of two strongly coupled silver spheres with radius $r = 30$ nm and a center to center distance of $d = 63$ nm embedded in glass with a nondispersive permittivity $\varepsilon_b = 2.25$ [116]. We take established experimental data for the dispersive permittivity of silver [69]. Such objects can be fabricated in large quantities by self-assembly methods, for example by connecting commercially available metal nanospheres with a linker molecule, as shown in section 3.2.1 [5].

We set $N = 2$, because the higher multipole orders do not have a notable contribution. As depicted in Fig. 4.3, scattering cross sections obtained from the different T-matrix methods agree very well. The multipole contributions are calculated according to Eq. 2.28. We can clearly identify three different resonances: a broad electric dipole resonance at 680 THz, and two resonances with mixed magnetic dipole and electric quadrupole contributions at 620 and 710 THz, respectively. While the broad resonance is connected to the eigenmode of the single sphere, the two sharper peaks can be explained by a hybridization caused by the coupling of the two spheres and coupling of higher order multipole modes, respectively [116].

We can obtain additional insights into the scattering behavior by looking at the

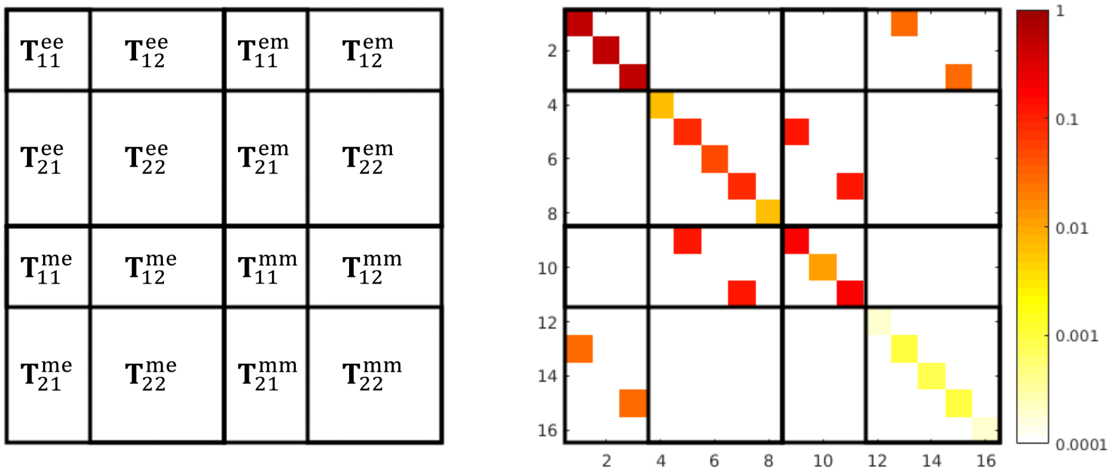

Figure 4.4: The left picture shows the general form of the T-matrix, as described in the previous section. For example $\mathbf{T}_{11}^{\mathrm{ee}}(\omega)$ represents the electric dipole coupling. In the following we always present the T-matrix in this way. On the right hand side we see the absolute values of the T-matrix entries for the dimer on a logarithmic scale at 600 THz. This matrix was calculated semi-analytically with the Mie coefficients of the single spheres.

entries of the T-matrix in Fig. 4.4 at a discrete frequency. The way the T-matrix is presented in that figure is adopted in all the following figures showing the T-matrix. Note that the entries are complexly valued and we always display the absolute values. At first we notice that the dominant entries are connected to the electric dipole $\mathbf{T}_{11}^{\mathrm{ee}}(\omega)$ and, to a lesser extent, to the magnetic dipole $\mathbf{T}_{11}^{\mathrm{mm}}(\omega)$ and electric quadrupole components $\mathbf{T}_{22}^{\mathrm{ee}}(\omega)$. Additionally, we see the aforementioned cross coupling between magnetic dipole and electric quadrupole $\mathbf{T}_{12}^{\mathrm{me}}(\omega)$ (and the other combinations with mixed contributions). This is the explanation for the mixed magnetic dipole and electric quadrupole resonance in the scattering cross section that was mentioned earlier.

Now, we investigate again the behavior of the T-matrix when we increase the number of illuminations K in the numerical calculation. We consider the T-matrix with $N = 4$ at the frequency 600 THz, where several multipole orders contribute to the total scattering. The spectral position is indicated by the vertical black line in Fig. 4.3. As a reference, we take the calculation based on Mie coefficients. In Fig. 4.5 we can observe the expected behavior of the error, the deviation decreases exponentially as we increase the number of plane wave illuminations. The more complicated structure actually benefits much more from a higher number of illuminations than the single sphere. In Fig. 4.6 we see the T-matrix entries of two different numbers of illuminations and the difference to the semi-analytically calculated T-matrix. We clearly see that the numerical inaccuracy is going down significantly when we increase the number of illuminations.

Additionally, we can deduce the preferential orientation of the induced multipoles from the pattern of the T-matrix. Let us investigate the electric dipolar part further

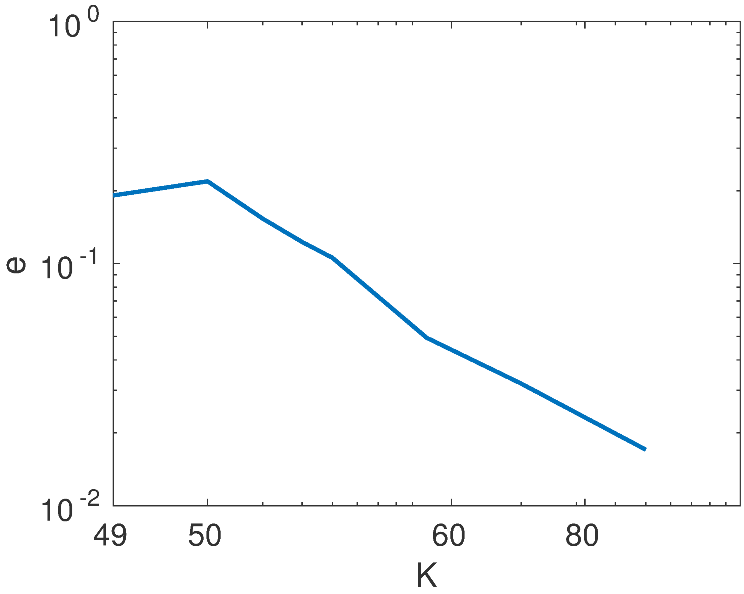

Figure 4.5: Convergence of the T-matrix calculation with the increase of the number of plane wave illuminations. The minimum number of illuminations necessary to solve for all the unknown entries of the T-matrix for the multipole order $N = 4$ is 48.

and call the entries

$$\mathbf{T}^{\mathrm{ee}}_{11}(\omega) = \begin{pmatrix} T^{\mathrm{ee}}_{\text{-1-1}}(\omega) & T^{\mathrm{ee}}_{\text{-10}}(\omega) & T^{\mathrm{ee}}_{\text{-11}}(\omega) \\ T^{\mathrm{ee}}_{\text{0-1}}(\omega) & T^{\mathrm{ee}}_{00}(\omega) & T^{\mathrm{ee}}_{01}(\omega) \\ T^{\mathrm{ee}}_{\text{1-1}}(\omega) & T^{\mathrm{ee}}_{10}(\omega) & T^{\mathrm{ee}}_{11}(\omega) \end{pmatrix}. \tag{4.16}$$

Now, the element $T^{\mathrm{ee}}_{\mathrm{ij}}(\omega)$ connects the incident coefficient $p_{1\mathrm{j}}(\omega)$ to the scattering coefficient $a_{1\mathrm{i}}(\omega)$. The same is true for all the other parts of the T-matrix, with adjustments for the higher order parts. The entry $T^{\mathrm{ee}}_{00}(\omega)$ is special, because it is connected to the z-axis. The z-axis is distinguished in the definition of the vector spherical harmonic functions. From this fact follows that if this particular entry has a large absolute value, the corresponding object will exhibit a strong electric dipole in z-direction. Conversely, the entries with ± 1 indices are connected to dipole moments in the x-y-plane. This consideration also translates directly to the magnetic part of the T-matrix. Considering this, we investigate again the entries of the T-matrix. We see in Fig. 4.6 that the electric dipole is almost isotropic. This becomes clear when we compare the T-matrix to that of a sphere. As stated above, we would get $T^{\mathrm{ee}}_{\text{-1-1}}(\omega) = T^{\mathrm{ee}}_{00}(\omega) = T^{\mathrm{ee}}_{11}(\omega) = a_1(\omega)$ and the elements with different indices would be equal to zero in this completely isotropic case. The magnetic dipole, however, is much weaker in the z-direction, because of the geometry of the investigated object with the gap. Hence, the magnetic dipole can be preferentially excited in the x-y-plane.

In conclusion, we can state that the presented method delivers accurate results and that it is highly beneficial to use a few illuminations more than absolutely necessary.

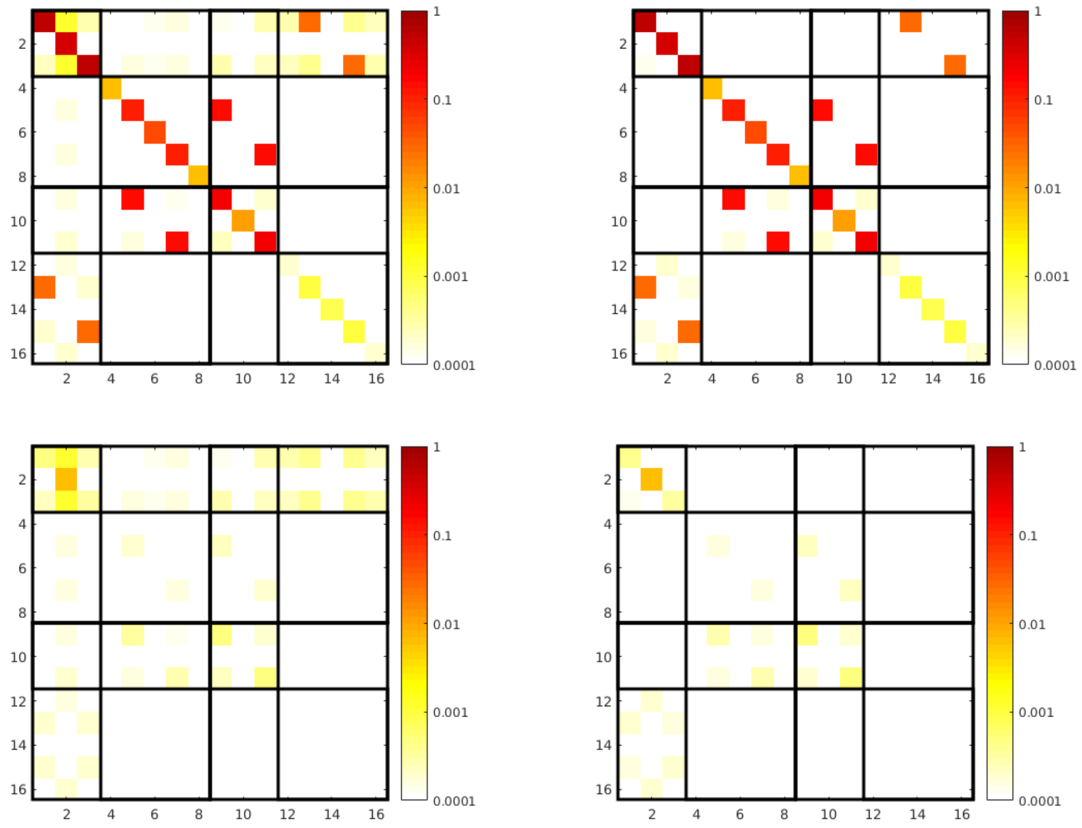

Figure 4.6: T-matrix entries of the dimer, calculated with the presented method at 600 THz. For the sake of clarity we show only the parts connected to the lowest two multipole contributions. On the left hand side we see the matrix with the minimum number of plane wave illuminations 48, on the right hand side with 50 extra illuminations. The bottom row shows the absolute difference to the semi-analytic solution $|\mathbf{T}_{\text{Mie}} - \mathbf{T}_K|$.

We demonstrated that obtaining the T-matrix entries of an object is quite advantageous. If we design an object with certain desired optical properties, we need to consider the corresponding part of the T-matrix. For example if we want to create an object with a strong magnetic dipole resonance excited in z-direction, we optimize the geometric parameters to maximize the corresponding T-matrix entry $T_{00}^{\text{mm}}(\omega)$.

Further useful applications of the method are presented in the following chapter 5.

4.4 Multiple scattering by arbitrary objects

Now, we present an extension to the multi scattering algorithm outlined in chapter 2. The aim is to calculate the scattering by an arbitrary but finite distribution of objects, e.g. clusters of spheres or helices, as depicted in Fig. 4.7. Up to now, we could only calculate the multiple scattering by several spheres from their Mie coefficients. On the other hand, we can calculate the T-matrix of a cluster of spheres or an arbitrary

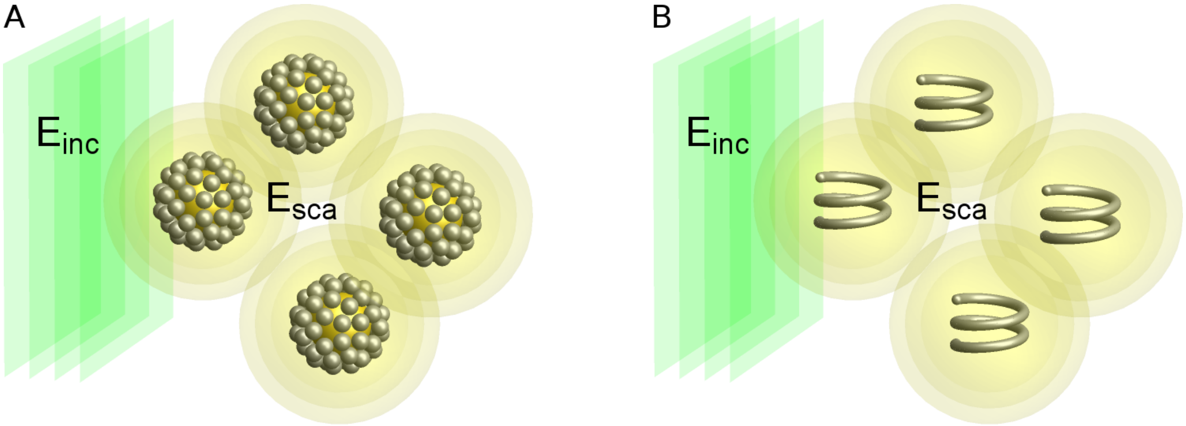

Figure 4.7: Schematic representation of the scattering by a distribution of clusters consisting of spheres (A) or helices (B), respectively.

object. As stated before, the Mie coefficients of a single isolated sphere are equivalent to its T-matrix. Therefore, we can extend the multi scattering algorithm to arbitrary objects, intuitively speaking, just by replacing the Mie coefficients with the full T-matrix.

We consider again the multiscattering system of equations, Eq. 4.4. By inserting the T-matrix, instead of the Mie coefficients and writing it in matrix notation, we arrive at

$$\begin{pmatrix} \mathbf{a}^j(\omega) \\ \mathbf{b}^j(\omega) \end{pmatrix} = \mathbf{T}^j(\omega) \cdot \left(\begin{pmatrix} \mathbf{p}^j(\omega) \\ \mathbf{q}^j(\omega) \end{pmatrix} - \sum_{l \neq j} \begin{pmatrix} \mathbf{A}(\omega) & \mathbf{B}(\omega) \end{pmatrix}(l,j) \cdot \begin{pmatrix} \mathbf{a}^l(\omega) \\ \mathbf{b}^l(\omega) \end{pmatrix} \right). \tag{4.17}$$

Here, $\mathbf{T}^j(\omega)$ is the T-matrix of the individual scatterer j and $\mathbf{A}(\omega)$ and $\mathbf{B}(\omega)$ form a matrix of the previously described translation coefficients corresponding to the respective positions of the objects.

The T-matrix contains the whole near and far field information on how a specific object interacts with any illumination. It depends on the geometry and material composition of the structure in question.

If we consider some distribution of randomly arranged, identical objects, we can take the same matrix for each object. This approach will speed up the calculation by a considerable amount, because we need to do the potentially time consuming T-matrix calculation only once. Then, we can use it to represent several identical objects. Furthermore, it can be used to simulate a multitude of different geometrical representations in a relatively short time.

However, in contrast to spheres, the objects are generally not spherically symmetric. Thus, we need to consider their respective orientation. The rotation of the particle can be represented by applying a rotation to the T-matrix [135]

$$\mathbf{T}^j(\omega) = \left(\mathbf{D}^j(\alpha, \beta, \gamma)\right)^* \cdot \mathbf{T}(\omega) \cdot \mathbf{D}^j(\alpha, \beta, \gamma). \tag{4.18}$$

Here, $\mathbf{D}(\alpha,\beta,\gamma)$ is the Wigner D-matrix

$$D^n_{ml}(\alpha,\beta,\gamma) = e^{-\mathrm{i}m\alpha} d^n_{m\mu}(\beta) e^{-\mathrm{i}\mu\gamma} \tag{4.19}$$

of the Euler angles α,β,γ corresponding to the desired rotation and the Wigner d-function $d^n_{m\mu}$ was given in Eq. 2.37 in section 2.1.

Note that we can apply the same scheme as outlined in section 4.1 to calculate the T-matrix of a cluster of arbitrary objects. This allows to build a hierarchy of objects in order to analyze the optical properties of the cluster and save computational resources in simulations of large structures.

We demonstrate the efficiency of the presented method by the following numerical example. Let us consider the scattering cancellation structure, which we introduced as an example in section 2.2. It consists of a dielectric core sphere surrounded by a larger number of metallic ellipsoids. The ellipsoids have the semi-axes $a_1 = 23$ nm and $a_2 = 5$ nm. The calculation of the T-matrix of a single ellipsoid with the method presented in section 4.2 takes approximately 90 s for a reasonable precision on a regular PC. We take dipole and quadrupole contributions into account, which is completely sufficient for the small ellipsoids. The subsequent multi scattering calculation of the whole structure with the central sphere and 24 ellipsoids is quite fast, the simulation of one distribution takes only 5 s. On the other hand, a finite element simulation of the scattering by the total structure does not even fit into the memory of a standard desktop machine.

4.5 Conclusion

We demonstrated an algorithm to calculate the T-matrix of clusters of spheres and a different one for arbitrary objects. We showcased numerical examples by calculating the T-matrix of several objects, thereby investigating the convergence of the presented method.

The T-matrix of arbitrary objects was calculated with the help of widely available and well established tools to calculate the scattered fields upon plane wave illumination. The T-matrix contains the electromagnetic scattering information independent of the illumination. By investigating the matrix, we get valuable information about the multipolar composition of possible resonances that are excited by certain illuminations. This is extremely useful to understand the nature of a given response as we show with several applications in the following chapter.

Furthermore, the T-matrix can be used in an extended multiscattering formalism to calculate the response of a whole cluster of objects efficiently. This algorithm, which we call *multiple T-matrix scattering method*, will speed up calculations by a large amount and prove to be very useful in the following chapter.

5 Metamaterials with arbitrarily shaped building blocks

Metamaterials have developed to be at the focus of extensive inovative research with several practical applications.

As pointed out in the introduction, nearly arbitrarily shaped metaatoms can be realized with top-down nanofabrication techniques. However, the main limitation of conventional techniques is their restriction to two dimensional distributions of metaatoms. Even though a stacking might alleviate the problem [83], eventually a restriction to thin films always persists. This is insufficient for multiple applications. Instead, truly three dimensional, i.e. bulk, metamaterials are required. To mitigate this problem, self-assembly and bottom-up strategies have been suggested, e.g. based on chemical processes. There, spherical nanoparticles are assembled directly in solution and can be made available as three dimensional material as shown in chapter 3. An alternative, slightly more sophisticated possibility to create three dimensional materials is to lift complicated metaatoms fabricated with top-down techniques from the substrate to have them suspended in a solution. We call such a marterial a metaliquid. By additional drying steps, the material can be sufficiently concentrated. Such approaches promise the combination of the advantages of both the top-down and the bottom-up approach. However, exploring such materials requires the correct prediction of their interaction with light.

The aim in this chapter is to characterize complex metaatoms by numerical means. The metaatoms should be more complex in the sense that they are not composed of spherical nanoparticles, but with a geometry beyond that of a sphere. The main task is to design objects with strong scattering properties, which have reasonable geometries and are suitable for fabrication. Furthermore, not only the response of the isolated object is considered, but ultimately the response of an ensemble of strongly interacting objects. This is done by computing the T-matrix of the single metaatom, which contains the complete scattering information. The T-matrix can then be used in the multiple T-matrix scattering algorithm to calculate, for example, the scattering cross section and the scattered fields of the full three dimensional ensemble. Such an approach makes it possible to study the field propagation in such a metaliquid.

Ultimately, the effective optical properties of a bulk, isotropic, three dimensional material shall be linked to the scattering properties of the single constituting metaatom, allowing to design various desirable characteristics of the metaliquid.

In this chapter, three contributions in that context are described. Firstly, we investigate in detail a scattering cancellation structure. The object under consideration is made of a dielectric core, whose scattering shall be suppressed by a layer of plasmonic particles. Contrary to previous designs, we propose the use of metallic ellipsoids instead of spheres. This allows to tune the operating frequency of the device within the visible spectrum.

Afterwards, we consider chirality in the context of electromagnetic scattering. We introduce a new definition of electromagnetic chirality. With this definition it is possible to assign an absolute value to scattering objects. As an example, we use this definition to design a metallic helix. The object is optimized to exhibit a strong electromagnetic chirality.

Finally, an approach to realize a three dimensional metamaterial with complicated building blocks is presented. The material is made out of plasmonic sandwich particles, which exhibit a magnetic and electric dipolar response. We perform a homogenization of the metamaterial and compare it to full wave simulations of the actual material made out of a large number of sandwich particles.

5.1 Scattering cancellation with tunable operating frequency

The possibility to conceal an object at a specific frequency for an external observer was simultaneously proposed by Ulf Leonhardt and Sir John Pendry and coworkers [29, 30]. They suggested different techniques for a coordinate transformation to design an enclosing structure, made from materials with complicated properties, to guide an incident electromagnetic field around a predefined spatial region [31]. With this approach, it is possible to hide an arbitrary object from an observer if the object is placed inside the transformed region. Additionally, carpet cloaks were explored that hide an object that resides on a planar surface, for example a metal mirror [32, 136–138] with a similar technique.

A completely different strategy to hide small particles from detection, developed by Andrea Alù and coworkers, was also proposed almost simultaneously [71] It led to the development of the scattering cancellation technique [139–142]. There, the scattering response of an electrically small object to a given illumination is reduced by encapsulating it with a shell. The shell is designed such that the illumination induces an electric dipole moment of the same magnitude as the one in the core object. The dipole moment is designed to oscillate with a phase difference of π with respect to the dipole moment of the core object, with the effect that the emerging destructive interference will cancel the scattered field [143]. This renders the object undetectable at the operating frequency in techniques that use the scattered light to detect the presence of an object.

Examples for possible applications are the suppression of the perturbation of the field to be detected by a tip in a scanning near-field optical microscope operated in scattering mode [144], or the manipulation of optical forces [145]. To realize these applications, it is important to be able to tune the operational frequency at which the scattering response is reduced.

For an operational frequency in the radio or microwave part of the spectrum, several metasurfaces have been suggested for the implementation of the scattering cancellation technique [68]. The functionality of such mantle cloaks has already been verified in experiments [146]. However, for optical frequencies, thus far only the feasibility of the concept was demonstrated, but not yet the ability to tune the operational frequency. First experiments employed a shell made from metallic nanospheres to cover the object from which the scattering response should be suppressed [147, 148]. This object, usually a dielectric sphere, has to be sufficiently small, such that the scattering response is dominated by the electric dipole moment. However, the restriction to metallic nanospheres as building blocks of the shell eventually fixes the operational frequency, because the resonance frequency of the nanospheres depends only marginally on the radius.

To mitigate this problem of low tunability, we suggest and study in this section the use of metallic ellipsoidal nanoparticles as the building blocks of the shell. Changing the aspect ratio changes the resonance frequency of the nanoparticles and with that the operational frequency across an extended spectral domain. Since the shell is usually fabricated by means of self-assembly techniques, an important question is whether the scattering reduction can be sustained for a random arrangement and orientation of the ellipsoids on top of the core object. Then, only a fraction of the ellipsoidal nanoparticles will effectively interact with the linearly polarized external illumination. The results presented in this section are based on reference [8].

We already studied theoretically the basic design of a scattering cancellation device in section 2.2 with two complementary analytical techniques. The purpose of these considerations was to demonstrate the underlying principle that causes the ability to tune the operational frequency and to provide a glimpse on the possible performance. The eventual functionality of the design is now demonstrated by full wave numerical simulations performed with the multiple T-matrix scattering method introduced in chapter 4.

5.1.1 Design

As introduced in section 2.2, we consider a central dielectric sphere with a radius of $r_\mathrm{s} = 61$ nm and made from a material with a nondispersive permittivity $\varepsilon_\mathrm{s} = 2.1$. The central sphere is covered with 24 metallic ellipsoids. The dispersive permittivity of the silver particles is obtained from established tabulated data [69].

The structure constitutes a challenge, since it consists of a larger number of resonant objects with fine details. We are not able to take advantage of any periodicity or symmetry, since the elliptical nanoparticles shall eventually be considered with a random orientation on top of the core object. We investigate this case, because we suggest bottom-up approaches to implement such scattering cancellation device. To

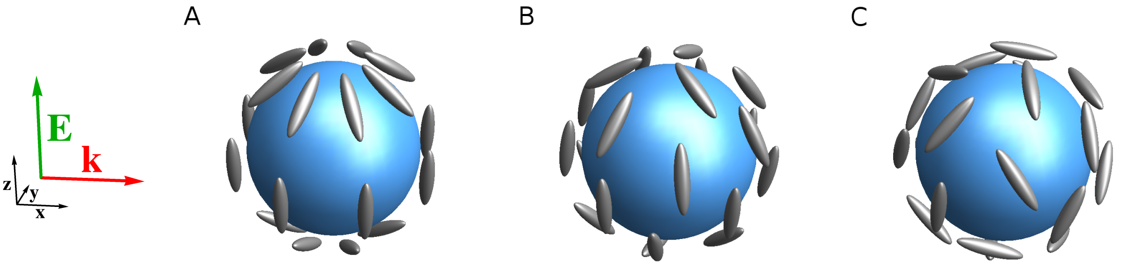

Figure 5.1: Different distributions and orientations of silver ellipsoids on a dielectric sphere. The illumination direction and polarization are depicted on the left hand side. We consider different scenarios for the placement of the ellipsoids: (A) Completely ordered and aligned, (B) Random distribution, but deterministic alignment, (C) Random distribution and random alignment.

cope with these challenges, we rely on the previously introduced multiple T-matrix scattering algorithm.

With the proposed T-matrix algorithm it is possible to calculate the scattering response from different distributions and orientations of the silver ellipsoids on the central sphere in short time and with high precision. To solve the problem numerically, we truncate the infinite sums of the multipole expansion of the electromagnetic fields at $N = 3$. This limits the size of the T-matrix of an isolated ellipsoid and renders the problem numerically feasible. However, already the quadrupole contribution ($n = 2$) is almost negligible due to the small size of the structure of about 140 nm compared to the operational wavelength $\lambda \approx 500$ nm.

We investigate three different configurations of ellipsoids on top of the core object, shown in Fig. 5.1. Figure 5.1 A shows a completely deterministic ordering of the ellipsoids, which is in principle based on a design presented in Ref. [149]. The ellipsoids have well-defined distances and are oriented to be tangential to the surface of the core (without touching it) sphere with an orientation that maximizes the projection of the major axis onto the polarization direction of the incident field. This is done to enhance the polarizability of the particles the shell is made of. However, when such a nanostructure is fabricated with self-assembly techniques, we have usually no direct control over the exact position of the ellipsoids. To reflect this uncertainty, we show in Fig. 5.1 B a random distribution of nanoparticles on the surface of the core sphere. Only a minimal distance to each other is kept to ensure that the ellipsoids are not in contact with each other. The particles are, however, still aligned with respect to the incident field polarization like in geometry A. Such an assembly could be realized for example by applying a static external field during the self-assembly process to force the particles to align [150]. Finally, Fig. 5.1 C shows the same random distribution additionally with random orientation of the ellipsoids on the surface of the sphere. If no specific measure is put in place, this would be the most likely distribution of the ellipsoids on top of the core object.

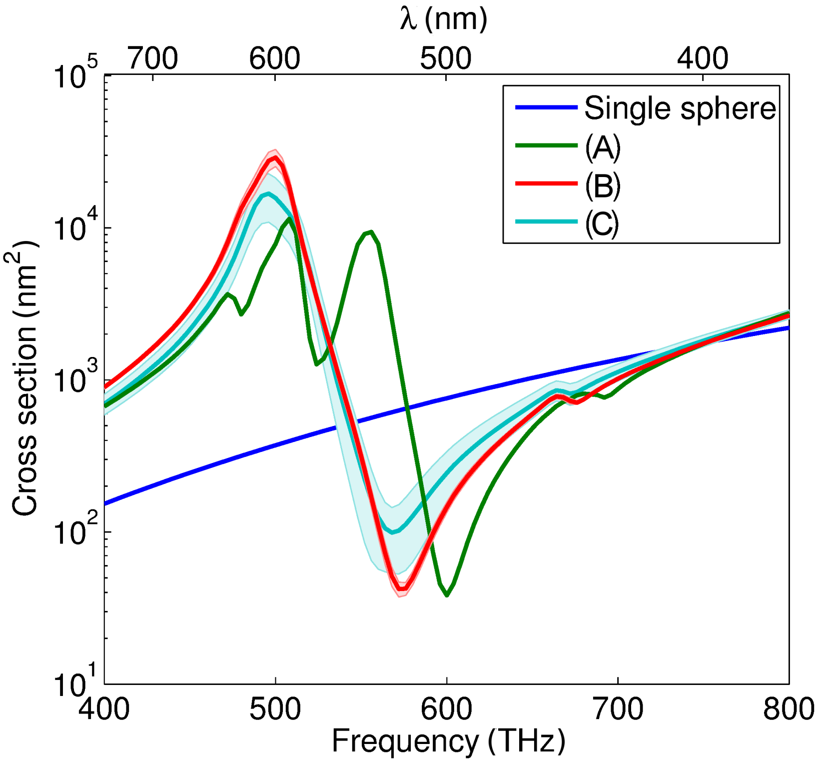

Figure 5.2: Numerically obtained scattering cross sections of different structures corresponding to the geometries shown in Fig. 5.1, A: Completely ordered and aligned, B: random distribution, but deterministic alignment, C: random distribution and random alignment. For B and C we display the averaged cross section of 100 simulations with different realizations of the random geometry. The shaded region shows the standard deviation. The ellipsoids have semi axes of $a_1 = 23$ nm and $a_2 = a_3 = 5$ nm.

5.1.2 Results

As shown in Fig. 5.2, the three different geometries possess in a similar qualitative optical response. The scattering cross section is reduced by almost one order of magnitude around the desired frequency of 600 THz as predicted by the analytic calculations in section 2.2.

There are a few notable observations. Firstly, as was expected, the scattering cancellation is weaker for randomly oriented particles (geometry C). This is because less ellipsoids are aligned along the polarization of the electric field with their large semi axis a_1. Furthermore, the second dip of the scattering cross section at approximately 530 THz, which was predicted by analytical considerations, is observed for the geometry with ordered ellipsoids (A). However, the minimum vanishes if we introduce disorder. This can be attributed to the fact that the effective permittivity of the shell shows a weaker dispersion, i.e. the strength of the Lorentzian-like dispersion is reduced. The effective permittivity of the disordered shell material no longer attains values corresponding to the negative solution of the scattering cancellation

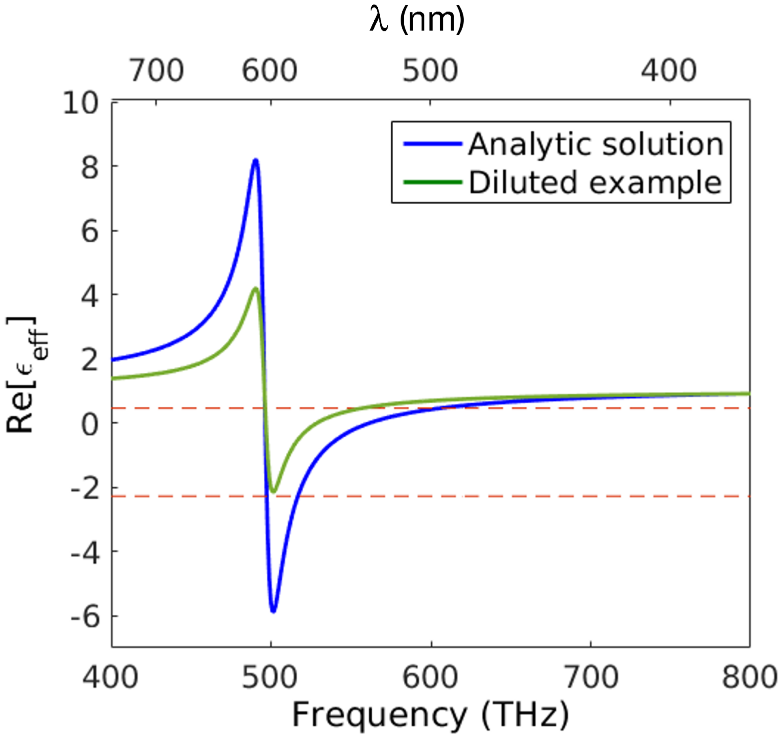

Figure 5.3: Analytically obtained effective relative permittivity of a material made of silver ellipsoids with semi axes $a_1 = 23$ nm and $a_2 = a_3 = 5$ nm (blue). The dashed lines show the solutions of the condition for scattering reduction, Eq. 2.63. The green line shows exemplarily the effective permittivity with a weaker dispersion. There, the negative solution is not attained and the positive solution is met at a lower frequency.

condition, Eq. 2.63. Therefore, only the positive solution persists. Finally, the frequency of minimal scattering is shifted towards the red part of the spectrum when we introduce disorder. This can likewise be explained with a lower dispersion of $\varepsilon_{\text{eff}}(\omega)$ of the shell, because the value of the positive solution of Eq. 2.63 is attained at a lower frequency. This can be understood intuitively by imagining a weaker dispersive $\varepsilon_{\text{eff}}(\omega)$, as shown in Fig. 5.3.

However, because of the qualitative similarity of the results with only slightly shifted target frequency, we can state that the design is rather robust against uncertainties, which may arise during self-assembly fabrication. We stress that different implementations of nominally identical geometries have nearly identical scattering responses. This is evidenced by the small red-shaded area in Fig. 5.2, which shows the standard deviation for different random positions of the ellipsoids. The exact details of the implementation of a specific disordered structure are not important. The variation of the relative orientation of the ellipsoids has a larger impact on the scattering reduction, as demonstrated by the cyan-shaded area. But the scattering cross section is still significantly reduced. Note that this means that the behavior of the disordered geometry C is generally independent of the direction and polarization of the incident plane wave illumination. Thus, the scattering cancellation structure

C is approximately isotropic.

As shown in chapter 2, the desired operating frequency can be tuned across a large fraction of the visible electromagnetic spectrum. This tunability is achieved by changing the aspect ratio δ of the metallic ellipsoids, while keeping the volume constant. Now, we perform full wave calculations with the multiple T-matrix scattering method established in chapter 4 to prove the prediction of the analytic calculations. As can be seen in Fig. 5.4, the operating frequency ranges from 430 THz to 700 THz if we modify the aspect ratio. An important point to consider is that the aspect ratios do not attain extreme values and are entirely in the range of what is possible to fabricate experimentally [151]. We show results of simulations with the completely disordered and isotropic geometry C.

The scattering reduction is slightly distorted in the case of the high aspect ratio ellipsoids with $\delta = \frac{a_1}{a_2} = \frac{36\text{ nm}}{4\text{ nm}}$. The distortion can be attributed to the fact that the particles are very long and are almost touching. Thereby, strong coupling is caused, which is completely excluded from the analytic considerations. However, the scattering cross section is still significantly reduced.

Finally, we explicitly compare the different methods that can be used to describe the functionality of the device. As shown in chapter 2, the object can be described as a homogeneous shell with an effective permittivity $\varepsilon_{\text{eff}}(\omega)$. Now, we do not only want to perform this homogenization analytically by considering the analytic expression for the polarizability of an ellipsoid, but we wish to back it up numerically. For this purpose, we calculate the average polarizability

$$\alpha(\omega) = \frac{\alpha_x(\omega) + \alpha_y(\omega) + \alpha_z(\omega)}{3} \tag{5.1}$$

of a single ellipsoid numerically, by using the T-matrix of an ellipsoid. The polarizability can be obtained from the scattering coefficients of the first order [116]. For example, for an illumination with z-polarized light the polarizability is given as

$$\alpha_{\text{z}}(\omega) = -\sqrt{12\pi} i Z_0 k \cdot a_{10}(\omega) \; . \tag{5.2}$$

Then, we use the Clausius-Mossotti relation, Eq. 2.59 to obtain the effective permittivity of the homogenized shell and conduct a full wave simulation of a sphere covered with the effective dispersive material.

As shown in Fig. 5.5, the functional behavior of the analytical calculation with volume homogenization and the numerical simulation are qualitatively very similar. However, the scattering reduction is weaker in the case of the numerical homogenization. This can be attributed to the lower dispersion in the effective permittivity. The dispersion is weaker, because additionally radiative losses are automatically included in the full wave solutions. In contrast, in the analytical discussion of the polarizability of the ellipsoid (Eq. 2.52) this has not been considered. The equation remains only strictly valid in the quasi-static regime. Additionally, the negative solution of Eq. 2.63 appears at higher frequencies. This is due to a shift in the resonance of $\varepsilon_{\text{eff}}(\omega)$ and also the aforementioned weaker dispersion.

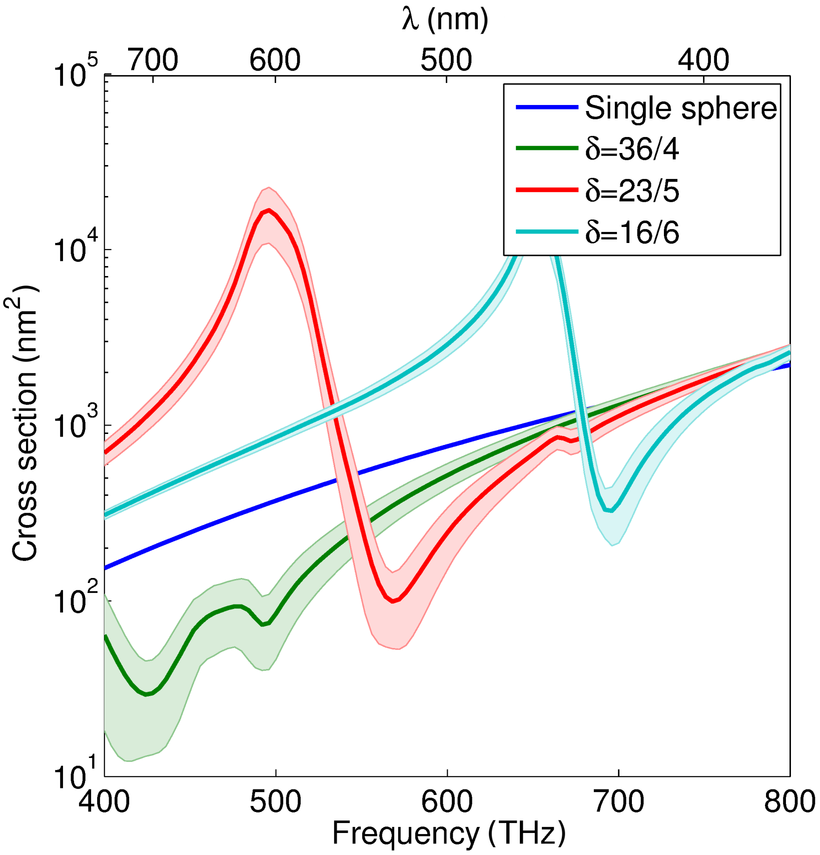

Figure 5.4: Numerically obtained scattering cross sections of spheres decorated with ellipsoids with different aspect ratios (green, red, cyan) and a bare sphere without scattering reduction (blue). The scattering reduction structures have the same disordered geometry that was shown in Fig. 5.1 C. The thick lines show the average of 100 different random realizations of the geometry and the shaded region visualizes the standard deviation.

In summary, we can state that we get very good agreement in the operating frequency predicted by the different numerical and analytic methods.

5.1.3 Conclusion

We introduced a new design for a scattering cancellation device. Instead of the established strategy to use plasmonic spheres or complicated metasurfaces, we decorate the dielectric core sphere with silver ellipsoids. The main advantage is the high tunability that allows to shift the operating frequency across the optical domain by changing the aspect ratio of the ellipsoids. Additionally, the design is feasible for a fabrication with self-assembly techniques, because the particles can be fabricated with chemical techniques and the design is quite robust to changes of the distribution. There, it is in principle also possible to avoid touching of the metallic

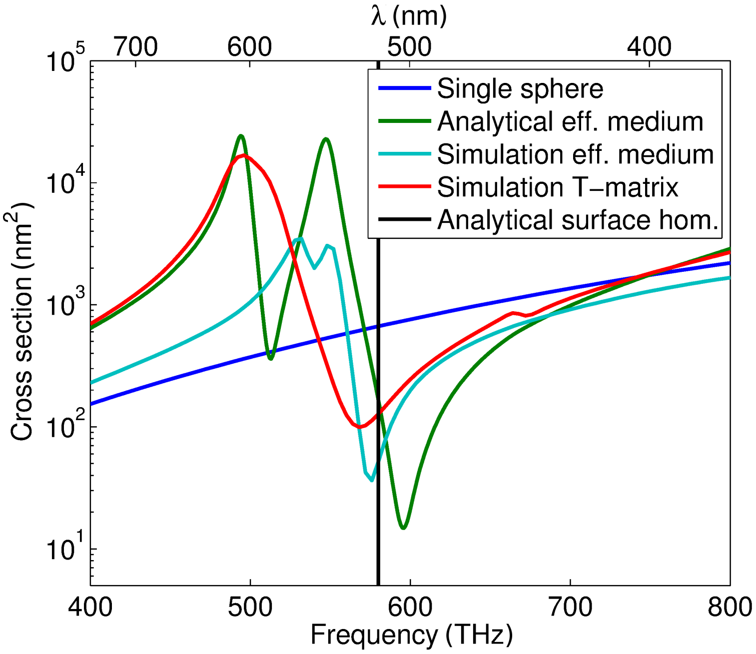

Figure 5.5: Scattering cross section of the single sphere (blue), analytically obtained effective medium coating (green), the numerical calculation of the effective shell (cyan), the complete full wave simulation of geometry C (red), and the predicted operating frequency from the surface homogenization (black).

particles, by enclosing them in a dielectric shell. This robustness was confirmed by performing a large number of simulations with varying random positions and orientations. All results show the same qualitative behavior.

We calculated the scattering by three different geometries of the principle design. This was done to validate two different approaches to describe the scattering cancellation device analytically. We showed that all methods have a very good agreement, especially in predicting the operating frequency. The response of the ellipsoids that were used in the shell is very well tunable by changing the aspect ratio. This allows for scattering cancellation at a desired frequency in the entire visible spectrum. Furthermore, we showed that an isotropic realization of the scattering cancellation device is possible and that it also significantly reduces the scattering by the core object.

5.2 Dual and chiral objects

In this section we investigate objects within the context of duality symmetry, which we introduced in chapter 2. We present a definition of electromagnetic chirality. It can be shown that this definition has an upper bound, which is achieved for reciprocal scatterers if and only if the object is transparent to fields of one electromagnetic helicity. This work was published in reference [7] and the theoretical considerations were largely conducted by Ivan Fernandez-Corbaton.

The geometric definition of chirality states that an object is considered to be chiral if it cannot be superimposed onto its mirror image (by rotations and translations). However, it is not clear how to measure chirality quantitatively and is not trivial to say which one out of two objects is more chiral. There are scalar measures of chirality, but they do not provide a way to establish a general ordering of chiral objects nor do they state what a maximally chiral object is [152–154].

Instead of a geometrical definition, we introduce a definition based on the interaction of the object with electromagnetic radiation [155]. More specifically, how the object interacts with fields of different polarization handedness, or helicity. Intuitively speaking, our definition can be formulated as: an object is chiral if the information obtained from illuminating the object with one helicity cannot be obtained from an illumination with the opposite helicity.

We show that all objects that are transparent to fields of one helicity, attain an upper bound of electromagnetic chirality. The reverse statement is also true for reciprocal objects: all reciprocal objects that are maximally chiral are necessarily transparent to all fields of one helicity. Furthermore, we show that an object which is reciprocal and maximally chiral must have duality symmetry. Then, we derive specific constraints on the T-matrix of a scatterer. These constraints are requirements on the design of a maximally chiral object.

But first we highlight two remarkable benefits of using helicity to describe the polarization of electromagnetic fields.

First, helicity commutes with translations and rotations. In other words: an object that is helicity preserving remains such after rotations and shifts. This is not necessarily the case if other descriptions are used. For example, a sphere has parity inversion symmetry. It preserves the parity of the incident field, when placed at the origin of coordinates. However, when it is shifted, the multipoles of different parity will mix upon interaction.

Second, helicity preservation and transparency to fields of one helicity do not depend on whether we consider the near-, intermediate-, or far-field zones. This is true because for a field of pure helicity, either $\mathbf{G}_{+}(\mathbf{r}, \omega)$ or $\mathbf{G}_{-}(\mathbf{r}, \omega)$ are equal to zero at all points in space and time. It has been shown in numerical simulations of a dual object illuminated with fields of helicity $+1$ that the fields of helicity -1 in very close proximity to the object have zero intensity [77].

5.2.1 Electromagnetic chirality

We consider a scattering object with an incident and scattered electromagnetic field. The fields around the object can be described with the helicity eigenstates introduced in Eq. 2.67 $[\mathbf{E}(\mathbf{r},\omega),\mathbf{H}(\mathbf{r},\omega)] \to [\mathbf{G}_+(\mathbf{r},\omega),\mathbf{G}_-(\mathbf{r},\omega)]$. The following quantity denotes the difference between the intensities of the two helicity eigenvectors

$$\kappa(\mathbf{r},\omega) = |\mathbf{G}_+(\mathbf{r},\omega)|^2 - |\mathbf{G}_-(\mathbf{r},\omega)|^2. \tag{5.3}$$

This quantity is directly related to the chirality density $Ch(\mathbf{r},\omega)$ which is widely employed to quantify the chiral character of fields surrounding scatterers [76,156]

$$\begin{aligned} Ch(\mathbf{r},\omega) &= -\frac{\varepsilon(\mathbf{r},\omega)\omega}{2}\mathrm{Im}[\mathbf{E}(\mathbf{r},\omega)^* \cdot \mathbf{B}(\mathbf{r},\omega)] \\ &= \frac{\varepsilon(\mathbf{r},\omega)\omega}{4c}\kappa(\mathbf{r},\omega). \end{aligned} \tag{5.4}$$

Here c is the speed of light and the asterisk denotes the complex conjugate. The connection between the quantities $\kappa(\mathbf{r},\omega)$ and $Ch(\mathbf{r},\omega)$ demonstrates the suitability of the helicity formalism to describe chirality of scattering objects.

For further considerations it is highly beneficial to represent the T-matrix of an object in the helicity basis. This is done with the transformation matrix $\mathbf{C}$ given as

$$\mathbf{C} = \frac{1}{\sqrt{2}}\begin{pmatrix} 1 & 1 \\ 1 & -1 \end{pmatrix}. \tag{5.5}$$

Then we get

$$\mathbf{T}^{\mathrm{h}} = \begin{pmatrix} \mathbf{T}^{\mathrm{h}}_{++}(\omega) & \mathbf{T}^{\mathrm{h}}_{+-}(\omega) \\ \mathbf{T}^{\mathrm{h}}_{-+}(\omega) & \mathbf{T}^{\mathrm{h}}_{--}(\omega) \end{pmatrix} = \mathbf{C} \cdot \begin{pmatrix} \mathbf{T}_{\mathrm{ee}}(\omega) & \mathbf{T}_{\mathrm{em}}(\omega) \\ \mathbf{T}_{\mathrm{me}}(\omega) & \mathbf{T}_{\mathrm{mm}}(\omega) \end{pmatrix} \cdot \mathbf{C}^{-1}, \tag{5.6}$$

where the submatrix $\mathbf{T}^{\mathrm{h}}_{\lambda\lambda'}(\omega)$ acts on input states of helicity $\lambda' \in [1,-1]$ and produces output states of helicity $\lambda \in [1,-1]$.

We define a scattering object to be electromagnetically achiral, if there exist four unitary matrices $\mathbf{U}_1$, $\mathbf{U}_2$, $\mathbf{V}_1$, and $\mathbf{V}_2$ that are helicity preserving and satisfy

$$\begin{aligned} \mathbf{T}^{\mathrm{h}}_{++}(\omega) &= \mathbf{U}_1\, \mathbf{T}^{\mathrm{h}}_{--}(\omega)\, \mathbf{V}_1, \\ \mathbf{T}^{\mathrm{h}}_{-+}(\omega) &= \mathbf{U}_2\, \mathbf{T}^{\mathrm{h}}_{+-}(\omega)\, \mathbf{V}_2. \end{aligned} \tag{5.7}$$

Hence, we call the object electromagnetically chiral, if there are no unitary matrices $\mathbf{U}_{1/2}$ and $\mathbf{V}_{1/2}$ that satisfy Eq. 5.7. Examples for unitary transformations with corresponding matrices are boosts, rotations, translations, and time inversions. Note that spatial inversion, parity, mirror reflections, and rotation reflections are examples of transformations that do *not* preserve helicity.

Equation 5.7 shows that, for an electromagnetically achiral object, all information that can be obtained with illuminations of fields of one helicity can also be obtained by illuminating it with fields of the opposite helicity. This is not true for electromagnetically chiral objects.

The common geometrical definition of chirality is included in our new definition as a special case. The geometric definition of achirality states that the mirror object can be superimposed onto the original object by a combination of rotations $\mathbf{R}$ and translations $\mathbf{S}$. This leads to the following condition

$$\mathbf{M}\,\mathbf{T}^{\mathrm{h}}(\omega)\,\mathbf{M}^{-1} = (\mathbf{S}\mathbf{R})\mathbf{T}^{\mathrm{h}}(\omega)(\mathbf{S}\mathbf{R})^{-1} \tag{5.8}$$

$$\mathbf{T}^{\mathrm{h}}(\omega) = \mathbf{M}^{-1}(\mathbf{S}\mathbf{R})\mathbf{T}^{\mathrm{h}}(\omega)(\mathbf{S}\mathbf{R})^{-1}\mathbf{M}, \tag{5.9}$$

where $\mathbf{M}$ is the mirror operator. This expression can be rearranged to get a special case of Eq. 5.7 as shown in Ref. [7]. But the definition of electromagnetic chirality allows also for more general transformations represented by $\mathbf{U}_i$ and $\mathbf{V}_i$. Specifically, boosts are possible, which makes our definition relativistically invariant.

Scalar electromagnetic chirality measure

The proposed definition allows to define scalar measures of how electromagnetically chiral an object is. This is done with the help of singular value decomposition. The singular value decomposition can always be performed with a complex matrix $\mathbf{A}$ as

$$\mathbf{A} = \mathbf{L}\mathbf{D}\mathbf{U}^{\dagger}, \tag{5.10}$$

where $\mathbf{L}$ is a lower triangular unitary matrix, $\mathbf{U}$ is an upper triangular unitary matrix, and $\mathbf{D}$ is a diagonal matrix containing the real valued singular values of $\mathbf{A}$. We denote the vector that contains these singular values in a nonincreasing order as $\boldsymbol{\sigma}(\mathbf{A})$. Then, we define two vectors, which contain the singular values of the submatrices corresponding to the different input helicities

$$\mathbf{v}_+(\omega) = \begin{bmatrix} \boldsymbol{\sigma}(\mathbf{T}^{\mathrm{h}}_{++}(\omega)) \\ \boldsymbol{\sigma}(\mathbf{T}^{\mathrm{h}}_{-+}(\omega)) \end{bmatrix}, \qquad \mathbf{v}_-(\omega) = \begin{bmatrix} \boldsymbol{\sigma}(\mathbf{T}^{\mathrm{h}}_{+-}(\omega)) \\ \boldsymbol{\sigma}(\mathbf{T}^{\mathrm{h}}_{--}(\omega)) \end{bmatrix}. \tag{5.11}$$

Equation 5.7 implies $\mathbf{v}_+(\omega) = \mathbf{v}_-(\omega)$ for achiral objects. This means that we can define a measure of electromagnetic chirality $\chi(\omega)$ based on the Euclidean norm of the difference of $\mathbf{v}_+(\omega)$ and $\mathbf{v}_-(\omega)$

$$\chi(\omega) = 2|\mathbf{v}_+(\omega) - \mathbf{v}_-(\omega)|. \tag{5.12}$$

We consider the quantity $C(\omega)$, which represents the total interaction cross section of the object (including scattering and absorption) with electromagnetic fields

$$C(\omega) = C_+(\omega) + C_-(\omega), \tag{5.13}$$

$$C_+(\omega) = 4|\mathbf{v}_+(\omega)|^2, \tag{5.14}$$

$$C_-(\omega) = 4|\mathbf{v}_-(\omega)|^2. \tag{5.15}$$

It can be understood as the sum of the interaction cross sections of the object regarding each input helicity $C_+(\omega)$ and $C_-(\omega)$, respectively.

We note that the total interaction cross section is the sum of the squared Euclidean norms of $\mathbf{v}_+(\omega)$ and $\mathbf{v}_-(\omega)$.

With the chosen definition in Eq. 5.12 the electromagnetic chirality has an upper bound. We demonstrate this by considering the following quantity

$$\frac{\chi^2(\omega)}{C} = 4\frac{|\mathbf{v}_+(\omega)|^2 + |\mathbf{v}_-(\omega)|^2 - 2\,\mathbf{v}_+(\omega)\cdot\mathbf{v}_-(\omega)}{C(\omega)} \tag{5.16}$$

$$= 1 - 2\frac{\mathbf{v}_+(\omega)\cdot\mathbf{v}_-(\omega)}{C(\omega)} \tag{5.17}$$

for $C(\omega) \neq 0$. Since the singular values that form the vectors $\mathbf{v}_\lambda(\omega)$ are real and greater than or equal to zero, the term $\mathbf{v}_+(\omega)\cdot\mathbf{v}_-(\omega)$ is also greater than or equal to zero. Therefore, the upper bound of $\chi(\omega)$ is given by $\sqrt{C(\omega)}$:

$$\chi(\omega) \in \left[0, \sqrt{C(\omega)}\right]. \tag{5.18}$$

Furthermore, we notice that this upper bound is attained only if $\mathbf{v}_+(\omega)\cdot\mathbf{v}_-(\omega) = 0$. This translates to the condition

$$\boldsymbol{\sigma}(\mathbf{T}^{\mathrm{h}}_{++}(\omega))\cdot\boldsymbol{\sigma}(\mathbf{T}^{\mathrm{h}}_{--}(\omega)) + \boldsymbol{\sigma}(\mathbf{T}^{\mathrm{h}}_{-+}(\omega))\cdot\boldsymbol{\sigma}(\mathbf{T}^{\mathrm{h}}_{+-}(\omega)) = 0. \tag{5.19}$$

Based on this result, we can show that the upper bound of electromagnetic chirality is achieved, if the object is transparent to one helicity. The object is transparent to helicity $+1$, if

$$\mathbf{T}^{\mathrm{h}}_{++}(\omega) = \mathbf{T}^{\mathrm{h}}_{-+}(\omega) = 0 \tag{5.20}$$

and transparent to helicity -1, if

$$\mathbf{T}^{\mathrm{h}}_{--}(\omega) = \mathbf{T}^{\mathrm{h}}_{+-}(\omega) = 0. \tag{5.21}$$

We immediately see that such objects satisfy Eq. 5.19 and are, therefore, maximally chiral.

The only other possibilities to satisfy Eq. 5.19 would be the combination of

$$\mathbf{T}^{\mathrm{h}}_{++}(\omega) = 0,\ \mathbf{T}^{\mathrm{h}}_{-+}(\omega) \neq 0,\ \mathbf{T}^{\mathrm{h}}_{--}(\omega) \neq 0,\ \mathbf{T}^{\mathrm{h}}_{+-}(\omega) = 0 \tag{5.22}$$

or

$$\mathbf{T}^{\mathrm{h}}_{++}(\omega) \neq 0,\ \mathbf{T}^{\mathrm{h}}_{-+}(\omega) = 0,\ \mathbf{T}^{\mathrm{h}}_{--}(\omega) = 0,\ \mathbf{T}^{\mathrm{h}}_{+-}(\omega) \neq 0. \tag{5.23}$$

These cases would not be transparent to one helicity. However, reciprocity imposes the following condition on the T-matrix of a scatterer [7]

$$\mathbf{T}^{\mathrm{h}}_{-+}(\omega) = 0 \iff \mathbf{T}^{\mathrm{h}}_{+-}(\omega) = 0. \tag{5.24}$$

Therefore, the additional cases shown in Eqs. 5.22 and 5.23 are violating reciprocity and are not of interest for our considerations.

Finally, we observe that reciprocal objects, which are transparent to one helicity must meet the requirement

$$\mathbf{T}^{\mathrm{h}}_{-+}(\omega) = \mathbf{T}^{\mathrm{h}}_{+-}(\omega) = 0. \tag{5.25}$$

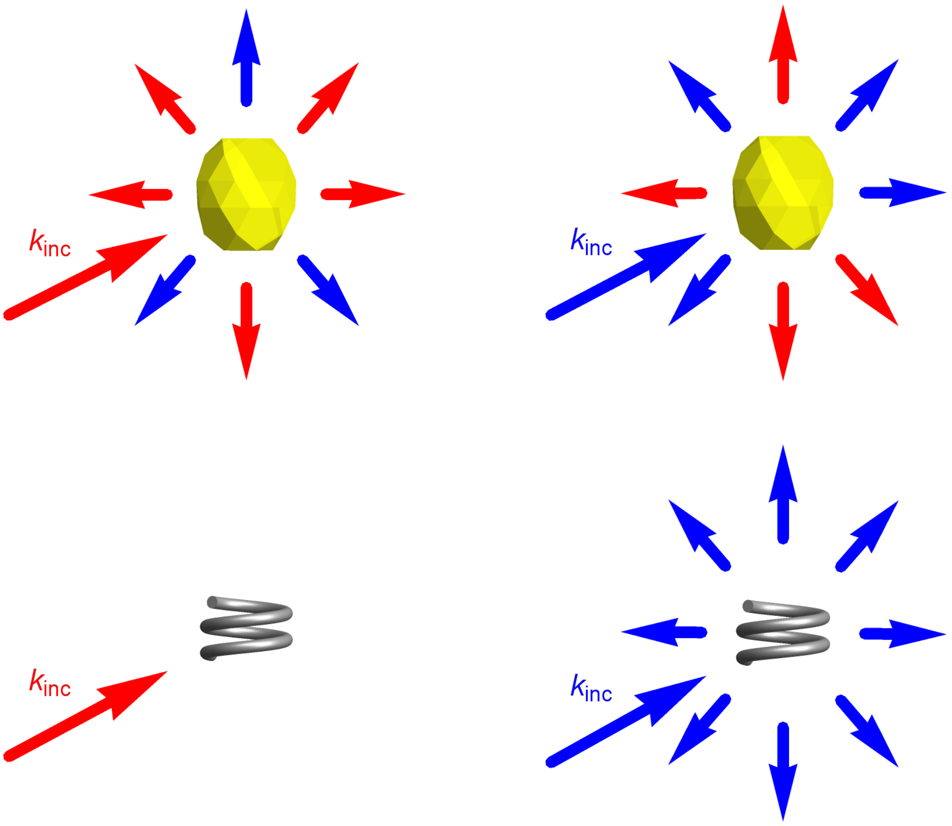

Figure 5.6: Interaction of a general object (top row) and a maximally chiral object (bottom row) with fields of pure helicity (red and blue, respectively). The general object interacts with both helicities and mixes them upon interaction. The reciprocal maximally electromagnetically chiral object interacts only with one helicity and does not produce fields of a different helicity.

This is the definition of helicity preservation (illumination with one helicity never produces a field of the other helicity). Thus, objects that satisfy this condition sustain electromagnetic duality symmetry and, vice versa, electromagnetic duality symmetry is a necessary condition for objects to reach maximal electromagnetic chirality. These findings are visualized in Fig. 5.6, where we show the interaction of light with general and maximally electromagnetically chiral reciprocal objects, respectively.

A possible application of this concept is helicity filtering glass, suitable for stereoscopic three dimensional vision. We consider two slabs made of randomly distributed and randomly oriented particles. These particles are reciprocal, maximally electromagnetically chiral, and lossy. Then, if the absorption is high enough, the slab will filter all fields of one helicity, while fields of the opposite helicity will be transmitted. The filtering is independent of the incidence direction, because of the behavior of helicity preservation and transparency. If we build two slabs with particles of opposite handedness, we get filters for each helicity, as depicted in Fig. 5.7. These slabs make suitable glasses for stereoscopic three dimensional vision, where the images for each eye are encoded in different circular polarizations.

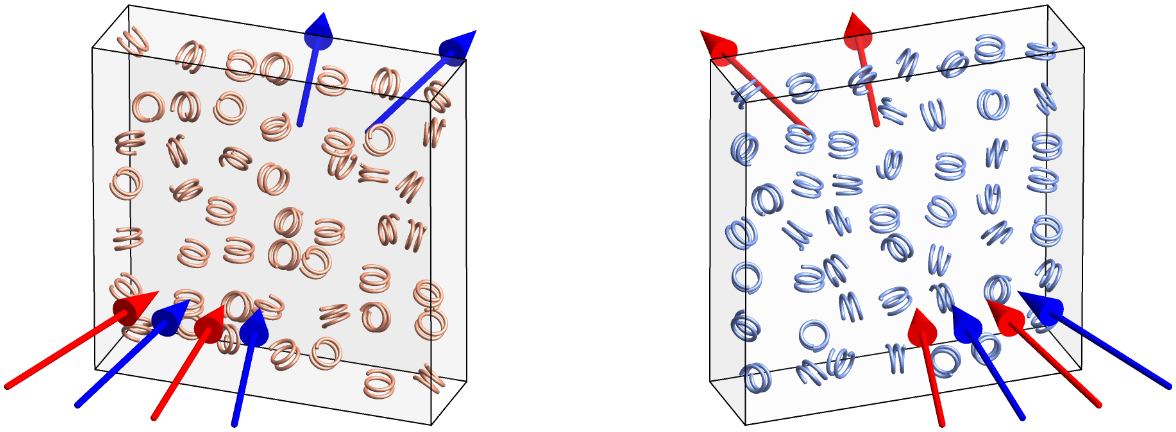

Figure 5.7: Two glass plates containing lossy maximally electromagnetically chiral objects of opposite handedness. Each slab filters out the fields of one helicity (red or blue) by absorption, the other pass through. This is independent of the angle of incidence.

In contrast to ordinary filtering glasses, based on quarter wave plates and linear filters, the filtering is independent on the orientation towards the illumination.

5.2.2 Numerical study

Now, we can utilize the biggest advantage of the method proposed in the previous chapter, namely that we can calculate the T-matrix of an arbitrarily complex object, to design the object towards high electromagnetic chirality. We show that a realistic object can approach the maximum electromagnetic chirality. Thereby, we exemplary show two important ideas. Large electromagnetic chirality is possible in the presence of material absorption and that we need duality symmetry to achieve maximal chirality. To showcase this, we compute the T-matrix of a metal helix with two windings. In this case, we can not make use of inherent symmetries of the object *a priori* and have no (semi-)analytic solution for the T-matrix available.

The choice of the geometrical structure is motivated by a helical antenna optimized for circular polarization [157, 158]. Under some assumptions, like perfect electric conductivity, the helix meets the dipolar duality condition at the resonance. With our powerful T-matrix method at hand, we are able to obtain the full scattering and absorption properties of a realistic helix made of silver [69].

Calculating the T-matrix is particularly interesting for the presented object, because numerous electromagnetic properties can be deduced from its entries that are otherwise not accessible. Here, we are interested in the duality conservation and electromagnetic chirality.

We optimize the object by changing the pitch, major radius, and wire radius of the helix, to maximize the electromagnetic chirality $\chi(\omega) = 2|\mathbf{v}_+(\omega) - \mathbf{v}_-(\omega)|$ at a frequency of 1.5 THz, or a wavelength of approximately 200 μm, respectively. The object is surrounded by vacuum. We obtain the following parameters for the helix:

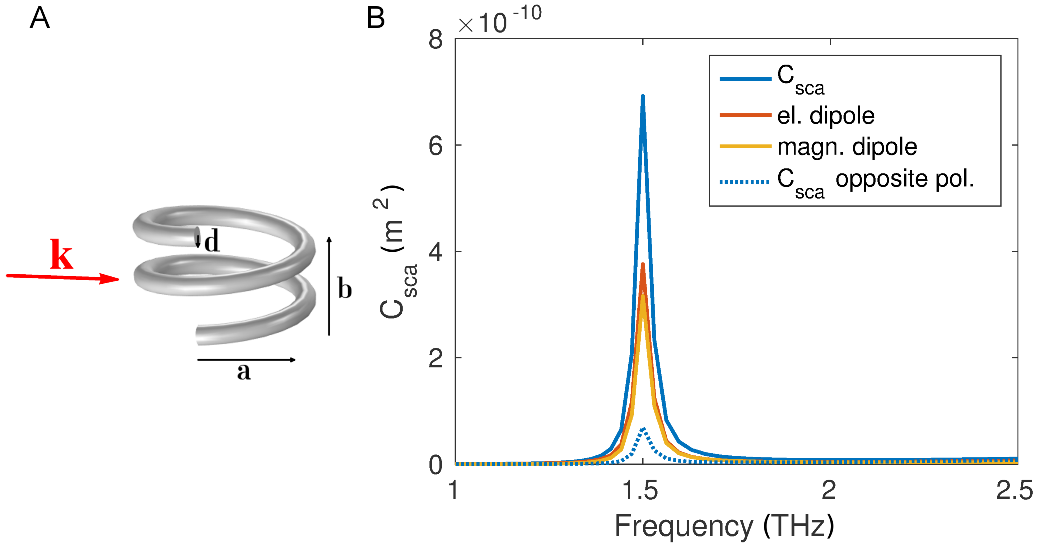

Figure 5.8: (A)Right handed metallic helix with two windings illuminated with a circular polarized plane wave. (B) Total scattering cross section for right handed (solid) and left handed (dotted) circular polarization. The electric and magnetic dipole contributions are approximately equal.

major radius $a = 6.48\ \mu$m, pitch $b = 8.52\ \mu$m, and wire radius $d = 0.8\ \mu$m (see Fig. 5.8).

As we see in Fig. 5.8, there is a strong difference in the scattering cross section if we illuminate with right or left circular polarized light, respectively. We can directly see that the object is approximately dual at the resonance frequency of 1.5 THz, because the magnetic and electric dipole contributions are balanced and no higher multipoles contribute to the total scattering [4].

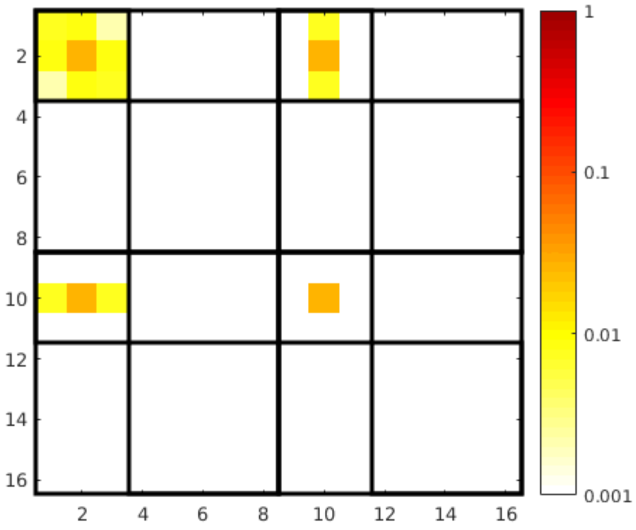

Figure 5.9: T-matrix entries of the right handed helix, calculated with the method presented in section 4.2 at 1.5 THz with 10 extra illuminations. See Fig. 4.4 for a description of the submatrices.

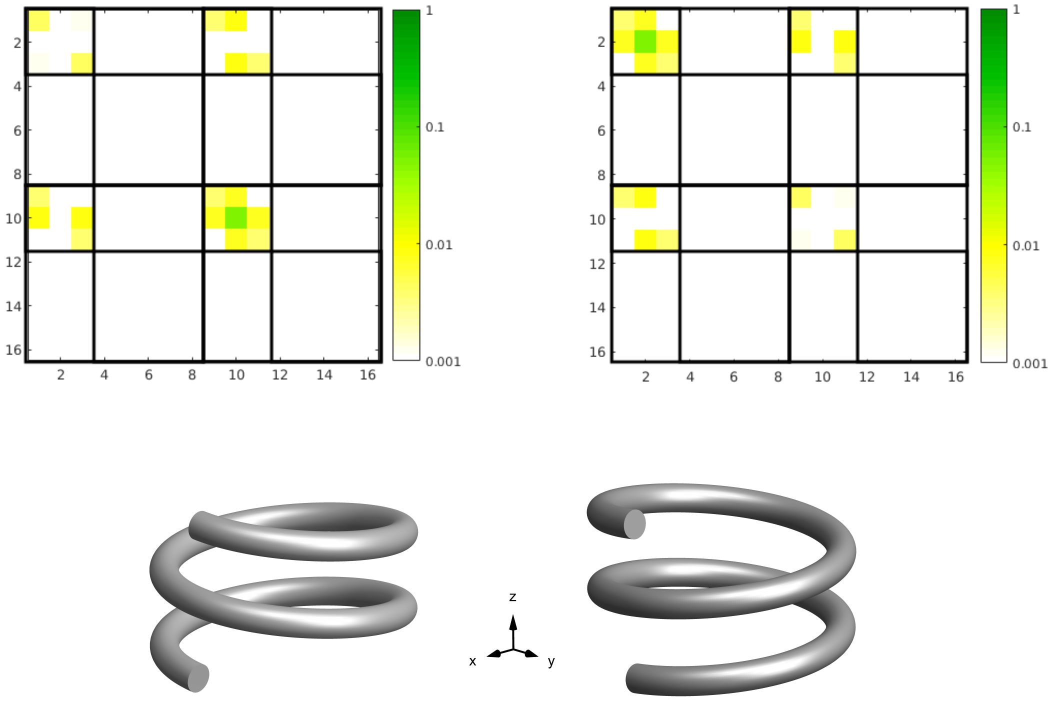

Figure 5.10: T-matrix entries in the helicity basis (obtained by Eq. 5.6) of a left and right handed helix, respectively. We clearly observe that each helix interacts primarily only with one helicity and that the mixing of different helicities is very low ($\mathbf{T}^h_{+-}$ and $\mathbf{T}^h_{-+}$). The T-matrices are ordered, in principle, in the same way as shown in Fig. 4.4, but with helicity $+$ and $-$ states instead of e and m.

By studying the T-matrix entries in Fig. 5.9, we can confirm that the object can be described in good approximation by the dipole contributions. Note that we show the entries of $|\mathbf{T}(\omega)|$ in the figure (this means The T-matrix is not shown in the helicity basis). The interesting aspect here is that the electric and magnetic dipoles have approximately the same strength and are both aligned along the z-axis at the considered frequency. Furthermore, the mixing of electric and magnetic dipole moments is also very strong. This means that an electric dipole is induced by a magnetic dipole excitation and vice versa. All these properties lead to the approximate duality symmetry of the object.

We get even more information about the duality by investigating the entries of the T-matrix in the helicity basis $\mathbf{T}^{\mathrm{h}}(\omega)$. In Fig. 5.10, the entries of the transformed matrix are depicted for a left and right handed helix, respectively. We can clearly distinguish the two cases, because each helix interacts only with one helicity. The left handed helix interacts with helicity -1 states (with the prominent entries in $\mathbf{T}^{\mathrm{h}}_{--}(\omega)$) and the right handed helix interacts with helicity $+1$ (with the prominent entries in $\mathbf{T}^{\mathrm{h}}_{++}(\omega)$). Most notably, the parts that correspond to the mixing of different helicities are approximately zero. Thus, the helix is indeed approximately dual at

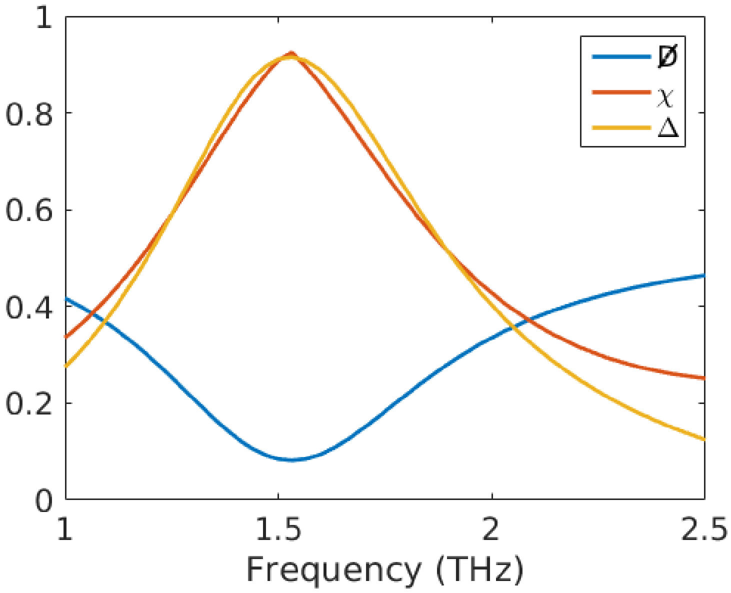

Figure 5.11: Duality breaking $\not{D}(\omega)$, normalized electromagnetic chirality $\chi(\omega)$, and cross section contrast $\Delta(\omega)$ of the helix. Large values of chirality and cross section contrast coincide with low duality breaking.

this frequency.

We define the contrast between the interaction cross sections to the two input helicities as

$$\Delta(\omega) = \frac{|\mathbf{v}_+(\omega)| - |\mathbf{v}_-(\omega)|}{C(\omega)}, \tag{5.26}$$

and the duality breaking, which quantifies the helicity change upon interaction, as

$$\not{D}(\omega) = \frac{\left|\boldsymbol{\sigma}(\mathbf{T}^{\mathrm{h}}_{+-}(\omega))\right|^2 + \left|\boldsymbol{\sigma}(\mathbf{T}^{\mathrm{h}}_{-+}(\omega))\right|^2}{C(\omega)}. \tag{5.27}$$

The interaction contrast $\Delta(\omega)$ ranges from -1 to 1 and is equal to zero if the object interacts identically with both incidence helicities. $\not{D}(\omega)$ ranges from zero to one and is zero if the object completely preserves helicity.

In Fig. 5.11 we show the duality breaking $\not{D}(\omega)$, the normalized electromagnetic chirality $\frac{\chi(\omega)}{\sqrt{C(\omega)}}$, and the interaction contrast $\Delta(\omega)$. A maximum value of $\frac{\chi}{\sqrt{C}} = 0.92$ is reached close to the target frequency of 1.5 THz. The two conditions needed to reach high electromagnetic chirality are illustrated in the figure: high contrast between the two helicity interaction cross sections and low helicity change in the interaction.

In Fig. 5.12 we show the scattering and absorption cross sections of the helix upon illumination with two oppositely circularly polarized plane waves. We can clearly see that values of high electromagnetic chirality (at 1.5 THz) are possible in the presence of material losses.

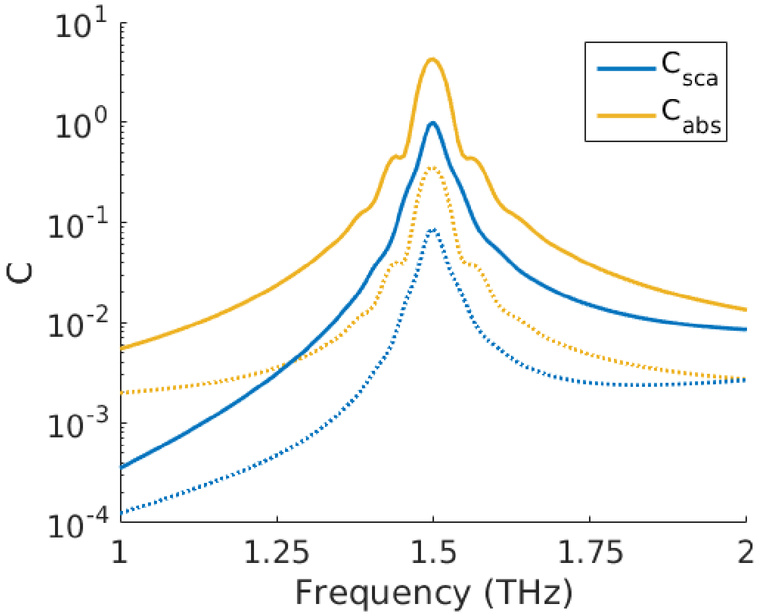

Figure 5.12: Normalized scattering and absorption cross sections of a helix, illuminated with two oppositely circularly polarized plane waves (solid and dashed lines, respectively). A notable absorption can be observed and the contrast between the two helicities amounts to one order of magnitude.

Note that the same geometry that exhibits high values of $\chi(\omega)$ at a frequency of 1.5 THz is not necessarily usable at optical frequencies. This is due to the fact that the electric and magnetic dipole resonance, which we observed at microwave frequencies, scale differently into the optical regime. The approximate duality symmetry breaks down, if they are not matched anymore. A different approach is needed to reach large values of electromagnetic chirality at visible frequencies. One possibility would be to use structures made out of dielectric spheres with high permittivity. These spheres can be designed to approximately meet the duality condition [4] and can be placed in a chiral arrangement.

5.2.3 Conclusion

We suggested a new definition for electromagnetic chirality of an object, based on how it interacts with the fields of opposite helicities. Our definition allows for an absolute ordering of objects to compare their chirality. Furthermore, the definition has an upper bound, where an object is maximally chiral. The upper bound is reached if an object is transparent to all fields of one helicity. Additionally, all maximally electromagnetically chiral objects must meet the duality symmetry condition. This means that these objects do not change the states of helicity of the fields they are interacting with.

A numerical analysis showed that a realistic object can achieve large values of electromagnetic chirality even in the presence of losses. This can be seen as an example for how the theoretical considerations in this section can be used to design a realistic scatterer with the desired properties.

5.3 Metaliquid

In this final section, we present the concept of a metaliquid. The idea is to create a three dimensional isotropic material, consisting of metaatoms fabricated by precise top-down methods. Here, the advantages of bottom-up and top-down techniques are combined.

As pointed out before, top-down fabrication techniques usually have some glaring weaknesses. The result of the fabrication is typically a two dimensional array of ordered metaatoms. However, for numerous possible applications, we need a material with an isotropic response. Furthermore, a lot of attractive metamaterial applications require a three dimensional material in a specific geometrical shape, for example to form lenses or filters, which is usually not possible with planar metasurfaces.

As pointed out in chapter 3, bottom-up methods solve some of these issues. They usually deliver a three dimensional isotropic material inherently, because the building blocks are assembled in solution. However, there are also some notable downsides. Usually, it is only possible to use spherical building blocks in most self-assembly techniques. Metaatoms made from these building blocks have usually a weaker response than top-down fabricated metaatoms, because the design possibilities are generally limited. Moreover, due to the indirectly controlled self-assembly, it is not possible to completely determine the end product. This can result in a size distribution of the particles and assemblies with different numbers of constituents. This became evident in section 3.2, where experimental realizations of self-assembled metamaterials were discussed.

Another, more sophisticated, possibility to create three dimensional metamaterials is to fabricate complicated metaatoms with top-down processes and lift them from the substrate to have them suspended in a solution. It is crucial to apply large area fabrication techniques in this process, to ensure a high number of available metaatoms [19]. We call the resulting material metaliquid. By additional drying steps, the material can be sufficiently concentrated. However, exploring such materials requires the correct prediction of their interaction with light. This is achieved by applying the previously presented T-matrix multi scattering method and comparing the result to a homogenized material.

The proposed metaliquid can be fabricated by combining top-down fabrication with bottom-up techniques. This procedure is currently ongoing with our experimental partner from the Friedrich-Schiller-University of Jena. Kay Dietrich performed the fabrication, but a final characterization of the resulting material is still pending.

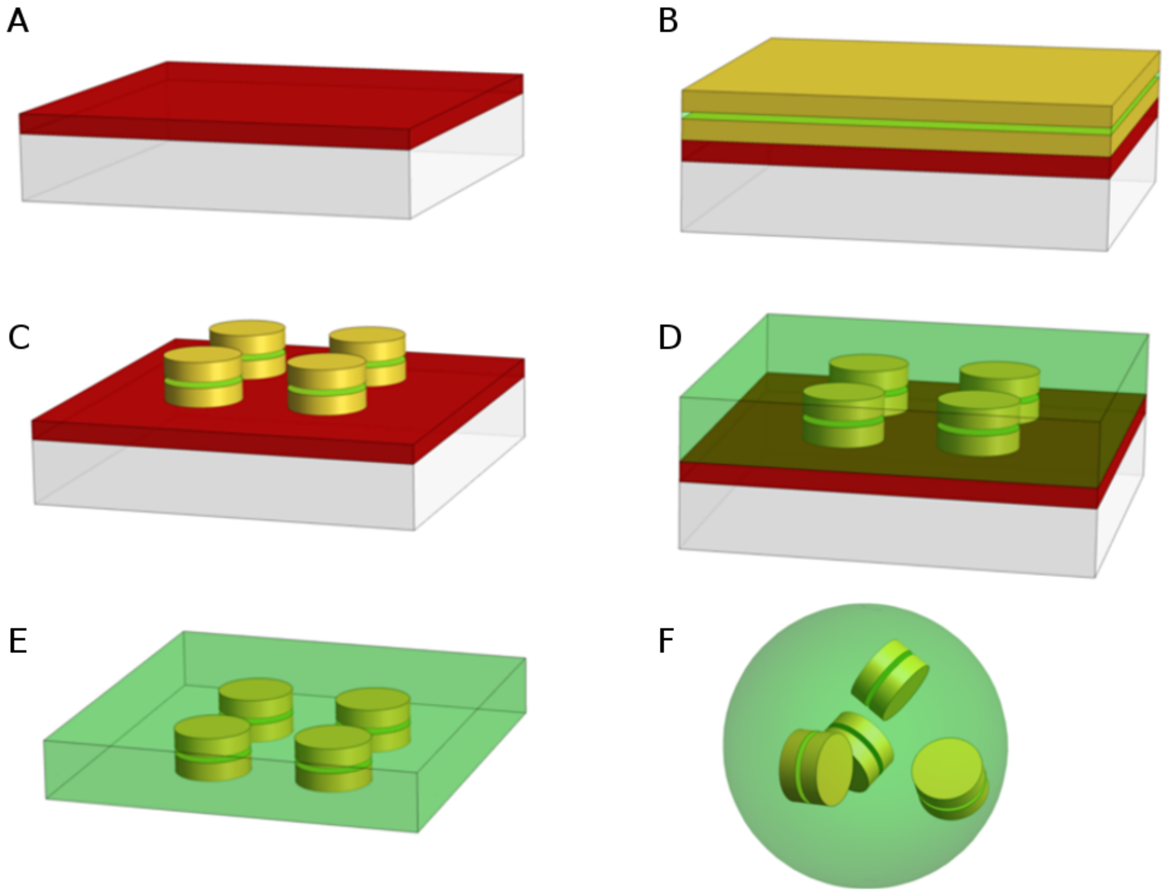

Figure 5.13: Schematic representation of the fabrication process.
(A) A sacrificial layer (red) is formed on the substrate (white).
(B) Gold and spacer layers (green) are grown on the sacrificial layer.
(C) Unwanted material is removed to form the sandwich geometry.
(D) A carrier layer is introduced (green) to hold the sandwich particles.
(E) The sacrificial layer is dissolved. This lifts the carrier layer with the particles from the substrate.
(F) Finally, the carrier layer is crumbled up and slowly dissolved. The particles are now arranged in a random three dimensional distribution.

The metaatoms are fabricated with established ion beam lithography. Different layers can be deposited, in our case a gold layer followed by a dielectric layer and finally another gold layer. The fabrication is illustrated in Fig. 5.13.

Now, the most important step is to lift the particles from the substrate to have them suspended in a three dimensional material. To achieve this, a sacrificial layer is introduced between the substrate and the particles, as indicated in Fig. 5.13 A. Then, after the sandwich particles are fabricated, an additional carrier layer is formed around the particles (Fig. 5.13 D). Finally, the sacrificial layer is dissolved to detach the particles from the substrate. The carrier layer can then be crumbled up and dissolved. This results in a random three dimensional arrangement of the particles, as is depicted in Figs. 5.13 E and F.

The partially dissolved carrier material, which acts as a host matrix for the sandwich particles, has a certain viscosity, in order to sustain a random orientation in space. If the viscosity would be too low, the sandwich particles would precipitate.

Let us now investigate the metaatom that can be fabricated by top-down methods. We consider a sandwich particle that consists of two metallic disks, separated by a dielectric spacer. The optical response of the isolated particle will determine the properties of the resulting metamaterial.

Afterwards, we consider a material made out of the presented metaatoms and show how light interacts with a chunk of the metamaterial. We employ a volumetric homogenization of the material to allow a simple description with effective material properties $\varepsilon_{\text{eff}}(\omega)$ and $\mu_{\text{eff}}(\omega)$.

5.3.1 Sandwich particle

Let us consider a single isolated sandwich particle. It consists of two metallic disks, separated by a dielectric spacer layer, as shown in Fig. 5.14 A. This particle is preferably fabricated by top-down procedures, such as electron beam lithography [19, 159].

The investigated object has a disk radius of 60 nm, metal disk height of 30 nm, and a spacer thickness of 10 nm. The metal disks consist of gold [69]. The spacer is made of SiO_2, for which we assume a nondispersive permittivity of $\varepsilon_{\text{s}} = 2.13$ and the object is surrounded by vacuum. The two separated disks support a magnetic dipole resonance, as can be seen in Fig. 5.14 B, at 336 THz. Additionally, there is a strong

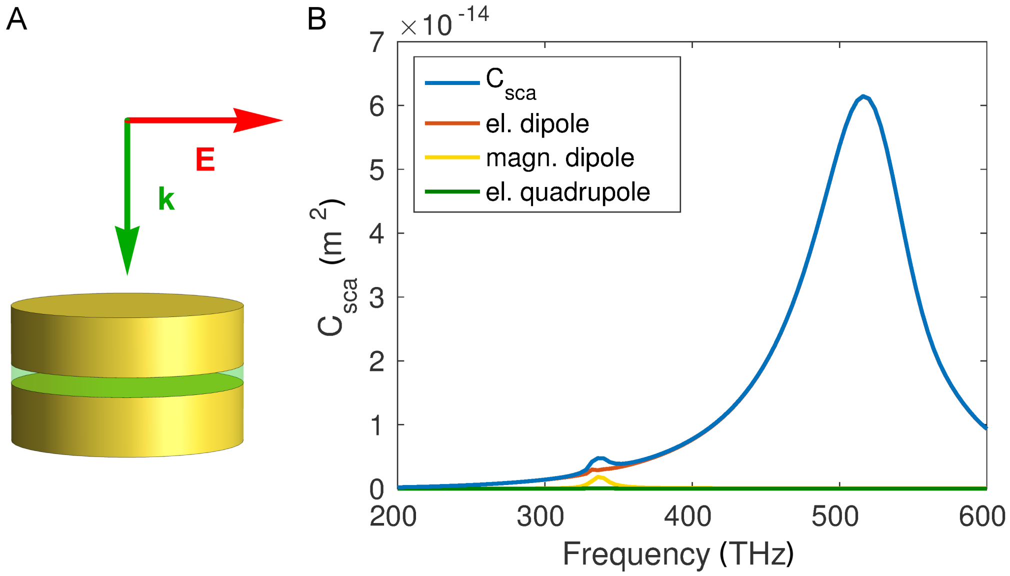

Figure 5.14: (A) Geometry and illumination of the sandwich particle. (B) Total scattering cross section (blue) of the sandwich particle and the contributions of different multipole orders. We observe an electric and a magnetic dipole resonance.

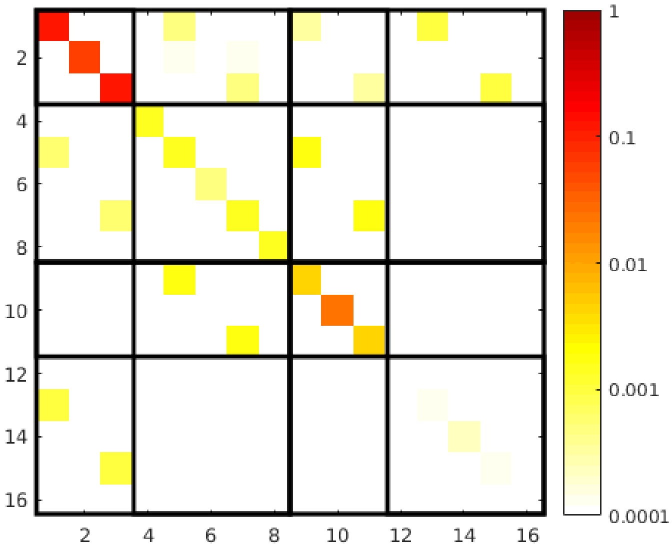

Figure 5.15: T-matrix entries of the sandwich particle, calculated with the presented method at 336 THz with 50 extra illuminations. See Fig. 4.4 for a description of the submatrices.

and broad electric dipole resonance at 520 THz that is attributed to the single disk resonance. The magnetic resonance can be understood as two oppositely oscillating electric dipoles in the disks.

We can observe a magnetic resonance that is much weaker than the electric dipole resonance, but the big advantage is that the peak is well isolated from the other resonances. Furthermore, we observe no higher multipole order contributions in the considered spectral region. This is particularly beneficial for homogenization. If the particle is well described by the first order contributions, we can apply the Clausius-Mosotti relation, which is only valid in dipole approximation. The geometry makes it possible to tune the electric and magnetic dipole resonances almost independently, because we have several parameters at hand, as opposed to the case of the dimer. The electric mode depends strongly on the radius of the disks, while the magnetic one can be tuned by changing the thickness of the gold and spacer layers, respectively.

The present geometry was chosen, because it is advantageous for a possible fabrication. An extremely strong magnetic dipole resonance is in fact undesired for a subsequent characterization of the resulting material. The reason is that the exact spectral position of a strong resonance with zero transmission can not be well determined. However, a particle with a much stronger magnetic dipole resonance can also be designed with the T-matrix algorithm.

We can get a deeper understanding of the response, by looking at the T-matrix. Figure 5.15 shows the entries of the matrix of the presented structure at the position of the magnetic resonance, 336 THz. We notice a strong similarity to the case of the dimer in section 4.2. This is because the object has almost exactly the same geometrical symmetries. However, we also see some notable differences. First, the particle can be described in very good approximation as a dipole, because the parts corresponding to higher multipoles are negligible. Furthermore, the cross coupling between the magnetic dipole and the electric quadrupole vanishes almost completely. This is the cause of the well isolated magnetic resonance we see in the scattering cross section in Fig. 5.14, in contrast to the mixed magnetic dipole and electric quadrupole resonances of the dimer.

5.3.2 3D isotropic medium

After calculating and studying the T-matrix of a single sandwich particle, we can now investigate the light propagation in a three dimensional material made out of these particles.

For this purpose, we consider exemplary a large spherical cluster made out of randomly distributed sandwich particles, as depicted in Fig. 5.16. The cluster has a radius of 600 nm and contains 50 sandwich particles. The constituting sandwiches have the same parameters as previously introduced. This amounts to a filling fraction of 6%. We choose a spherical cluster, because we can compare the result to a calculation of a solid sphere with homogeneous material parameters corresponding to the effective parameters of the metamaterial.

To homogenize the three dimensional material, we apply the Clausius-Mossotti relation, Eqs. 2.59 and 2.60. This is justified, since the particles we consider can be described very well in the dipolar regime, which was confirmed by investigating the T-matrix entries in the previous section.

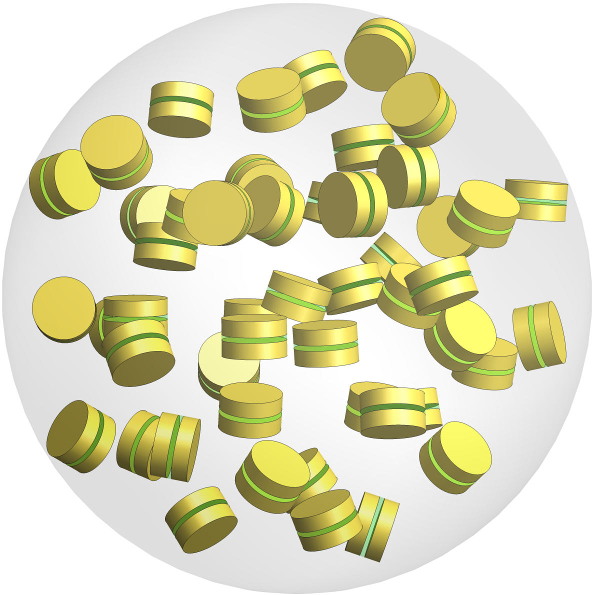

Figure 5.16: Spherical cluster with a radius of 600 nm. The cluster is composed of 50 sandwich particles.

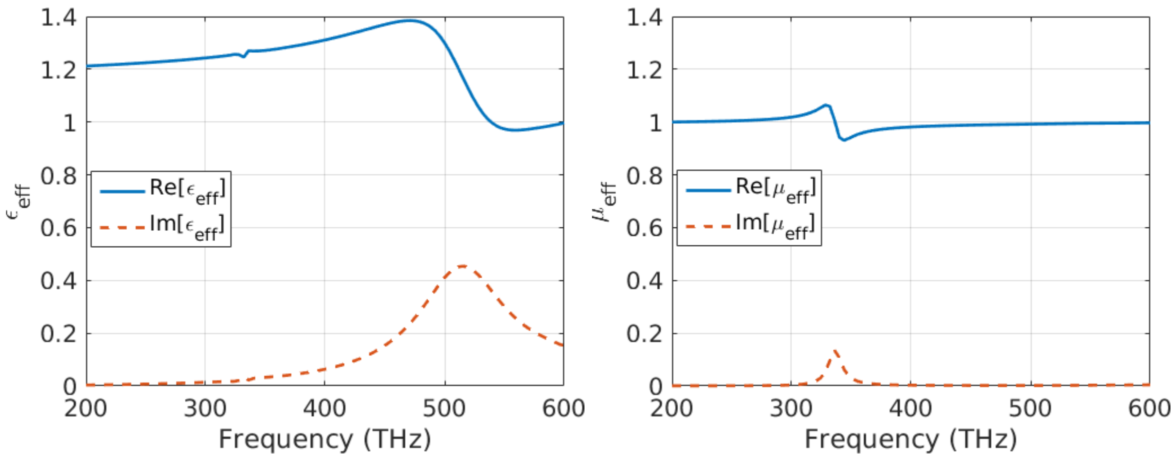

Figure 5.17: Effective permittivity and permeability of a material made out of sandwich particles with a filling fraction of 6%. We observe resonances at frequencies exactly corresponding to the positions of the electric (520 THz) and magnetic (336 THz) dipole resonances of the single particle, respectively.

The polarizability of a single sandwich particle is calculated numerically from its T-matrix, then we take the average of the different possible illumination directions. We show the results of the homogenization in Fig. 5.17. We see that the magnetic dipole resonance of the single particle causes a resonance in the effective permeability, as expected. Similarly, the electric dipole resonance causes a dispersion in the effective permittivity.

Now we can compare a simulation of the actual cluster to a simulation of a sphere with the homogenized material. We consider a spherical cluster with a radius of 600 nm filled with 50 randomly distributed and randomly oriented sandwich particles. This way, we get an approximately isotropic structure. The scattering response is calculated with the multiple T-matrix scattering method introduced in chapter 4. The cluster is illuminated with a linearly polarized plane wave. The single particles can be very well described in dipole approximation, but the large cluster is expected to exhibit higher order multipole contributions, due to the coupling and the large size, compared to the wavelength (clustersize 1200 nm and wavelength $\lambda \approx 700$ nm). We take a maximum order of $N = 9$ into account.

The results of the respective simulations are shown in Fig. 5.18. For the purpose of clarity we do not display all multipole contributions, because the higher order terms have only a marginal contribution. Again, we can clearly identify two distinct resonances in the total scattering cross section: one at 330 THz, which corresponds to the spectral position of the magnetic dipole resonance of the single sandwich particle. And a broader resonance around 500 THz, which corresponds to the electric dipole resonance of the single sandwich (compare Fig. 5.14).

We observe an excellent agreement in the two different simulations, especially at lower frequencies. The strong resonance corresponding to the electric resonance of the single sandwich particle is very well reproduced in the extinction cross section,

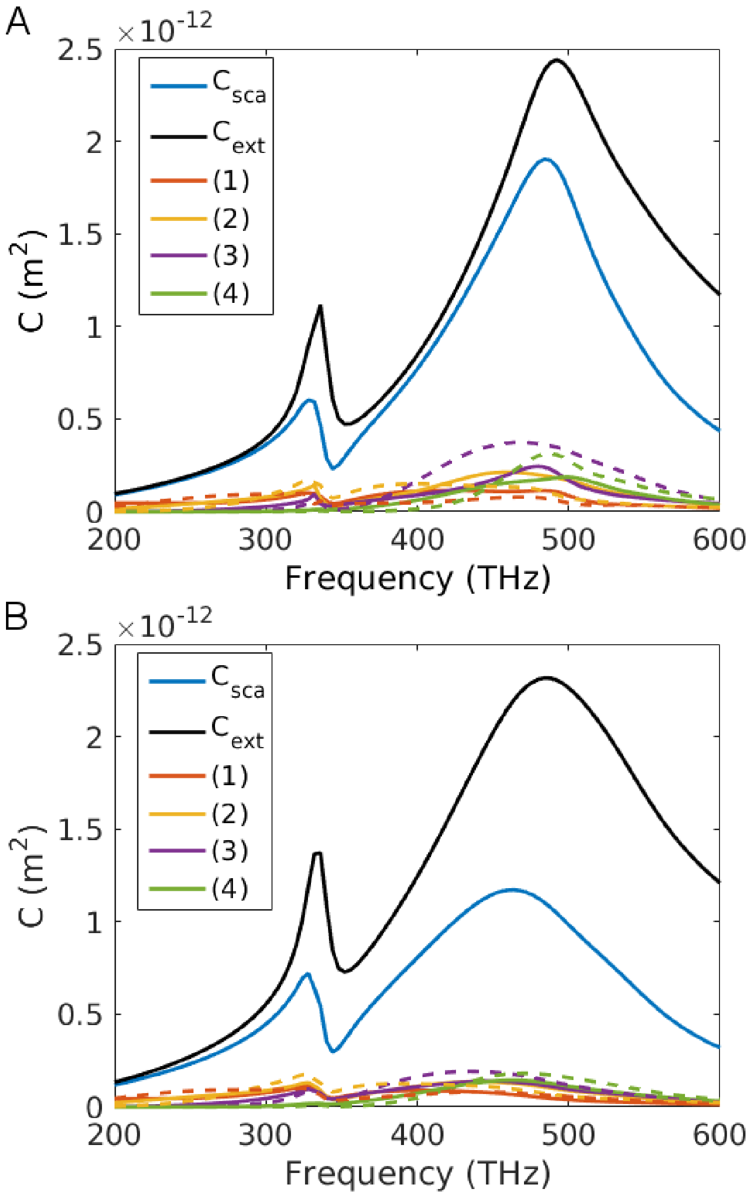

Figure 5.18: Comparison of the scattering cross section of (A) the full simulation of 50 sandwich particles with the multiple T-matrix algorithm and (B) a simulation of a large homogeneous sphere with effective properties $\varepsilon_{\mathrm{eff}}(\omega)$ and $\mu_{\mathrm{eff}}(\omega)$. The black line shows the total extinction cross section, the blue line shows the total scattering cross section, and the other colors correspond to the different multipole contributions to the scattering cross section, as indicated by their order in the legend. Here, the solid lines correspond to the electric contributions and the dashed lines correspond to the magnetic multipole contributions, respectively.

however, the scattering cross section in that spectral domain is slightly lower in the effective simulation. This suggests that the absorption is overestimated in the effective permittivity.

Even though the single sandwich particles are very well described in dipole approximation, the combined cluster has comparably strong higher order multipole contributions. The main scattering contribution comes from the third and fourth order.

The homogenized sphere with effective material parameters is expected to get higher order multipole contributions, because the sphere is much larger than the wavelength (diameter 1200 nm and $\lambda \approx 700$ nm). Most notably, also the qualitative behavior of the higher order multipole contributions to the scattering cross section is very similar in the two cases.

5.3.3 Conclusion

We presented a sophisticated method to fabricate a three dimensional metamaterial composed of complexly shaped metaatoms.

Exemplary, we investigated a sandwich particle. The particle exhibits a strong electric dipole resonance and a spectrally separated magnetic dipole resonance. Additionally, we considered a material made out of these particles. Due to the fact that the sandwich particle is well described in dipole approximation, it is suitable for a homogenization technique. Here, we applied the Clausius Mossotti relation to perform the volumetric homogenization.

With our multiple T-matrix scattering method we simulated the scattering response of a large number of coupled sandwich particles in a cluster. The results are compared to a simulation of a homogeneous sphere with dispersive effective permittivity and permeability. The results show a very good agreement, which confirms that an effective description of such a metamaterial is valid.

6 Conclusions

In this thesis, we demonstrated that there are impressive possibilities in the field of self-assembled metamaterials. After introducing the theoretical basis we showcased several interesting designs of metaatoms built out of spheres. Hereby, we were closely collaborating with experimental partners. These collaborations were fruitful, because a regular exchange of experience helps both sides to strife for new ideas. The theoretical considerations yield new ideas for metamaterial designs, while experimental restrictions need to be taken into account. Furthermore, numerical simulations are often crucial to understand the observed phenomena, as became clear in section 3.2.

A main contribution of this thesis to the broader field of self-assembled metamaterials has been the introduction of metallic nanoshells instead of solid nanospheres as building blocks in core-shell metaatoms. Hereby, we significantly improved the established design. These modified metaatoms sustain a notable magnetic response. Furthermore, an additional modification of the core object causes also a strong electric response. A resulting metamaterial, with sufficient filling fraction, exhibits a negative effective index of refraction in the near infrared. In principle, all metaatoms that are composed of spheres can be modified in the outlined way, to shift the resonance frequency and, most notably, improve the strength of the resonance.

Currently, an obstacle in the realization of these ideas is the fabrication of very thin metallic shells. As was shown in section 3.2.2, it is possible to grow very thin metallic shells on gold nanospheres with chemical reactions. A similar fabrication on dielectric nanospheres is more challenging, but should be possible in the near future. Metallic shells with thicknesses of several nanometers can already be fabricated by several different techniques [94, 95].

The main achievement of this dissertation was the multiple T-matrix scattering method. Here, we used the T-matrix to perform simulations of distributions of large numbers of arbitrarily placed and oriented objects. This method requires that we know the T-matrix of the considered objects. Therefore, we showed two efficient methods to calculate the T-matrix. The first is applicable to objects that are solely composed of spheres. The method is based on the multiple Mie scattering method, which we introduced in chapter 2. The second method is much more versatile, but also computationally more expensive. Here, the T-matrix of arbitrarily shaped particles is calculated by evaluating the scattered fields of multiple plane wave illuminations of the object.

The T-matrix is very useful to understand how an object interacts with electromagnetic fields. The object is described independently of a specific illumination. The magnitude of different entries of the matrix tells us how the object reacts to a specific exiting multipole.

In the last chapter, we applied the multiple T-matrix scattering method to gain insights into the scattering by objects with complicated geometry. We investigated a new design of a scattering cancellation device. By using plasmonic ellipsoids instead of spheres in the scattering cancellation structure we got a tunable operating frequency in the visible spectrum.

Hereby, we also applied the homogenization techniques introduced in the theoretical basis and compared the results to the full wave simulations. If the metatom under consideration is sufficiently small compared to the wavelength of the illumination, then it is well described in dipole approximation. The presented homogenization is a good model to describe the light propagation in materials composed of the considered metaatoms.

We introduced a definition of electromagnetic chirality. Hereby, we used the T-matrix calculation to optimize an object to exhibit large chirality. This is a prime example of the usefulness of the T-matrix for the design of metaatoms. If we want to design an object with specific electromagnetic properties, we often need to consider specific entries or submatricies of the T-matrix. Then, we varied the geometric and material properties of the object to achieve the desired result. We used this technique to obtain a realistic object that attains a large value of electromagnetic chirality at resonance.

Finally, we presented a scheme to construct a three dimensional metamaterial with complexly shaped metaatoms. This was done by combining parts from top-down fabrication with the advantages of self-assembly. Metaatoms are fabricated with high precision by top-down methods. Then, they are lifted off the substrate and distributed in a random isotropic manner. We investigated exemplary a metaatom that consists of two separated metal disk, called a sandwich particle. The scattering response of the resulting metamaterial was then obtained with a full wave simulation using the multiple T-matrix scattering method. Additionally, we performed a volumetric homogenization of the metamaterial and calculated effective material parameters. This way we showed that an effective description of a metamaterial composed of dipolar particles is valid. This constitutes a tremendous simplification, because we do not have to consider the fine details of the complicated material. Instead, the details are replaced by a homogenized material.

After all these considerations, we can formulate answers to the raised questions:

How does light interact with a certain object?

This information is encoded in the T-matrix. It contains the whole information about how an object interacts with electromagnetic fields. The T-matrix is independent of the illumination and, therefore, not limited to special cases, which are often assumed in the analysis of metaatoms.

How does light propagate through a material composed of such objects?

If the constituting objects can be well approximated by dipoles, we can investigate the light propagation by considering a homogenized material with effective material properties. If the metaatoms exhibit notable higher order contributions, we can apply the presented multiple T-matrix scattering method. There, we can obtain detailed information on how electromagnetic waves travel through a spatially constrained chunk of the metamaterial.

The T-matrix of a scattering object constitutes a powerful tool to investigate the optical response of the single object. With the numerical tools provided in this thesis it is much easier to obtain the T-matrix of interesting objects. Because the T-matrix can be calculated in short time, it is possible to perform optimizations of existing designs to substantially increase the performance. Thereby, it is possible to choose optimization targets that are otherwise not accessible. Examples include, but are not limited to, the excitation of specific multipole moments, duality symmetry, and electromagnetic chirality. Thus, the design of novel metaatoms can be very well supported with this T-matrix calculation at hand.

Furthermore, it is also possible to calculate the collective response of multiple arbitrarily shaped objects. With this multiple T-matrix scattering method at hand is possible to further investigate the coupling of closely spaced metaatoms. Such an analysis is possible without considering a specific illumination, by investigating the eigenstates of the T-matrix. This concept was recently shown for metaatoms made of spherical building blocks [11]. Now, with the multiple T-matrix scattering method at hand, it is also possible to extend this analysis to arbitrarily shaped metaatoms.

Finally, the method allows to calculate the propagation of an arbitrary illumination (such as a Gauß beam) through a finite arrangement of arbitrarily shaped, placed, and oriented objects. Thereby, we can take higher multipole orders into account and obtain precise results in relatively short computation time.

Acknowledgments

After all the presented work in this thesis, I want to express my gratitude to all people that supported me during my time as a PhD student.

First and foremost, I want to thank my wonderful wife Teresa, for making this thesis only the second most important thing I made. Thank you for our incredible daughter Matilda and the amazing support and motivation, especially during the time of writing this thesis!

Of course, I want to thank my supervisor Carsten Rockstuhl for providing a great deal of stimulus and support throughout my time as a PhD student. He gave me the opportunity to work on the fascinating topic of metamaterials, even though I came from a very different field and had much to learn in the beginning.
Thank you for turning me into a scientist!
I would like to thank Prof. Dr. Martin Wegener for taking the burden of providing his expert assessment as the second referee (even during Christmas time).
Furthermore, I want to express my gratitude to the whole Photonics group, or in fact both of them. I had a great time both in Jena and in Karlsruhe. Special thanks go to Stefan Mühlig, who created the multi Mie scattering algorithm, which is the foundation of the work presented in this thesis, and who introduced me to the topic of self-assembled metamaterials. Likewise, very special thanks go to Ivan Fernandez-Corbaton, who helped me with my T-matrix normalization (without which a great deal of the presented work would not have been possible) and introduced me to the concept of duality symmetry.
During my time as a PhD student, I had several fruitful collaborations. At the Friedrich-Schiller-University of Jena, I want to thank Florian Kretschmer and Reinhard Geiss with whom I did several collaborations on self-assembled metamaterials, and Kay Dietrich, who fabricated metaatoms I designed. I also want to thank Dana Cialla-May for providing insightful SERS measurements. Then, I want to thank Wiktor Lewandowski from the University of Warsaw, for contacting us to work on dynamically tunable metamaterials together. I want to thank Alessio Monti from the Niccolò Cusano University for the fruitful collaboration on metamaterial cloaks.

Additionally, I want to thank my friends from the numerical relativity group, where I did my masters. *Die Zeit war geil!* In particular, I want to Thank Dr. Toni Dietrich, Dr. Nidas Moldenhauer, and Dr. Smo Harms for proof reading the manuscript. And of course, also special cheers to the rest of the Olf Council.

Abschlieend möchte ich noch meinen Eltern für ihre unentwegte Unterstützung danken, speziell wärend meines Studiums, aber natürlich auch generell in meinem Leben. Außerdem möchte ich meinem großen Bruder Flori dafür danken, mein Interesse an Naturwissenschaften schon sehr früh geweckt zu haben.

Appendix

A Translation coefficients

$$A_{nm}^{n'm'}(\mathbf{d}_{lj},\omega) = (-1)^{m'}\frac{\gamma_{mn}}{\gamma_{n'm'}}\mathrm{e}^{i(m-m')\phi_{lj}} \sum_{q=|n-n'|}^{n+n'} f(m,n|-m',n'|q) \times g(n,n',q)\begin{bmatrix} h_p^{(1)}(kd_{lj},\omega) \\ j_p(kd_{lj},\omega) \end{bmatrix} P_q^{m-m'}(\cos\theta_{lj}) \left|\begin{matrix} r \le d_{lj} \\ r > d_{lj} \end{matrix}\right. , \tag{A.1}$$

and

$$B_{nm}^{n'm'}(\mathbf{d}_{lj},\omega) = (-1)^{m'+1}\frac{\gamma_{mn}}{\gamma_{n'm'}}\mathrm{e}^{i(m-m')\phi_{lj}} \sum_{q=|n-n'|}^{n+n'} f'(m,n|-m',n'|q,q-1) \times g'(n,n',q)\begin{bmatrix} h_p^{(1)}(kd_{lj},\omega) \\ j_p(kd_{lj},\omega) \end{bmatrix} P_q^{m-m'}(\cos\theta_{lj}) \left|\begin{matrix} r \le d_{lj} \\ r > d_{lj} \end{matrix}\right. . \tag{A.2}$$

Here, $d_{lj} = |\mathbf{d}_{lj}|$ is the distance of the coordinate systems. We used the functions

$$f(m,n|m',n'|q) = (-1)^{m+m'}(2q+1)\sqrt{\frac{(n+m)!(n'+m')!(q-m-m')!}{(n-m)!(n'-m')!(q+m+m')!}} \times \begin{pmatrix} n & n' & q \\ m & m' & -(m+m') \end{pmatrix}\begin{pmatrix} n & n' & q \\ 0 & 0 & 0 \end{pmatrix}, \tag{A.3}$$

$$f'(m,n|m',n'|q,p) = (-1)^{m+m'}(2q+1)\sqrt{\frac{(n+m)!(n'+m')!(q-m-m')!}{(n-m)!(n'-m')!(q+m+m')!}}, \times \begin{pmatrix} n & n' & q \\ m & m' & -(m+m') \end{pmatrix}\begin{pmatrix} n & n' & p \\ 0 & 0 & 0 \end{pmatrix}, \tag{A.4}$$

$$g(n,n',q) = \frac{\mathrm{i}^{n'-n+q}(2n'+1)}{2n'(n'+1)}[n(n+1)+n'(n'+1)-q(q+1)], \tag{A.5}$$

$$\tag{A.6}$$

and

$$g'(n,n',q) = \frac{\mathrm{i}^{n'-n+q}(2n'+1)}{2n'(n'+1)} \times \sqrt{(n+n'+1+q)(n+n'+1-q)(q+n-n')(q-n+n')}. \tag{A.7}$$

Here, we used the Wigner $3j$ symbols $\begin{pmatrix} n & n' & q \\ m & m' & -(m+m') \end{pmatrix}$ [62].

Bibliography

[1] M. Fruhnert, S. Mühlig, F. Lederer, and C. Rockstuhl, "Towards negative index self-assembled metamaterials," *Physical Review B*, vol. 89, no. 7, p. 075408, 2014.

[2] F. Kretschmer, M. Fruhnert, R. Geiss, U. Mansfeld, C. Höppener, S. Hoeppener, C. Rockstuhl, T. Pertsch, and U. S. Schubert, "Plasmonic nanoparticle clusters with tunable plasmonic resonances in the visible spectral region," *Journal of Materials Chemistry C*, vol. 2, no. 31, pp. 6415–6422, 2014.

[3] W. Lewandowski, M. Fruhnert, J. Mieczkowski, C. Rockstuhl, and E. Górecka, "Dynamically self-assembled silver nanoparticles as a thermally tunable metamaterial," *Nature communications*, vol. 6, no. 6590, 2015.

[4] I. Fernandez-Corbaton, M. Fruhnert, and C. Rockstuhl, "Dual and chiral objects for optical activity in general scattering directions," *ACS Photonics*, vol. 2, no. 3, pp. 376–384, 2015.

[5] M. Fruhnert, F. Kretschmer, R. Geiss, I. Perevyazko, D. Cialla-May, M. Steinert, N. Janunts, D. Sivun, S. Hoeppener, M. D. Hager, *et al.*, "Synthesis, separation, and hypermethod characterization of gold nanoparticle dimers connected by a rigid rod linker," *The Journal of Physical Chemistry C*, vol. 119, no. 31, pp. 17809–17817, 2015.

[6] M.-S. Kim, T. Scharf, S. Mühlig, M. Fruhnert, C. Rockstuhl, R. Bitterli, W. Noell, R. Voelkel, and H. P. Herzig, "Refraction limit of miniaturized optical systems: a ball-lens example," *Optics express*, vol. 24, no. 7, pp. 6996–7005, 2016.

[7] I. Fernandez-Corbaton, M. Fruhnert, and C. Rockstuhl, "Objects of maximum electromagnetic chirality," *Physical Review X*, vol. 6, p. 031013, 2016.

[8] M. Fruhnert, A. Monti, I. Fernandez-Corbaton, A. Alù, A. Toscano, F. Bilotti, and C. Rockstuhl, "Tunable scattering cancellation cloak with plasmonic ellipsoids in the visible," *Physical Review B*, vol. 93, p. 245127, 2016.

[9] A. Rahimzadegan, M. Fruhnert, R. Alaee, I. Fernandez-Corbaton, and C. Rockstuhl, "Optical force and torque on dipolar dual chiral particles," *Physical Review B*, vol. 94, no. 12, p. 125123, 2016.

[10] M. Fruhnert, I. Fernandez-Corbaton, V. Yannopapas, and C. Rockstuhl, "Optical force and torque on dipolar dual chiral particles," *Submitted to Beilstein Journal of Nanotechnology*, 2016.

[11] R. N. S. Suryadharma, M. Fruhnert, I. Fernandez-Corbaton, and C. Rockstuhl, "Studying plasmonic resonance modes of hierarchical self-assembled meta-atoms based on their transfer-matrix," *Submitted to Physical Review B*, 2016.

[12] D. R. Smith, W. J. Padilla, D. Vier, S. C. Nemat-Nasser, and S. Schultz, "Composite medium with simultaneously negative permeability and permittivity," *Physical review letters*, vol. 84, no. 18, p. 4184, 2000.

[13] J. B. Pendry, A. J. Holden, D. Robbins, and W. Stewart, "Magnetism from conductors and enhanced nonlinear phenomena," *IEEE transactions on microwave theory and techniques*, vol. 47, no. 11, pp. 2075–2084, 1999.

[14] M. S. Rill, C. Plet, M. Thiel, I. Staude, G. Von Freymann, S. Linden, and M. Wegener, "Photonic metamaterials by direct laser writing and silver chemical vapour deposition," *Nature materials*, vol. 7, no. 7, pp. 543–546, 2008.

[15] N. Anscombe, "Direct laser writing," *Nature Photonics*, vol. 4, no. 1, pp. 22–23, 2010.

[16] C. Marrian, F. Perkins, S. Brandow, T. Koloski, E. Dobisz, and J. Calvert, "Low voltage electron beam lithography in self-assembled ultrathin films with the scanning tunneling microscope," *Applied physics letters*, vol. 64, no. 3, pp. 390–392, 1994.

[17] P. M. Mendes, S. Jacke, K. Critchley, J. Plaza, Y. Chen, K. Nikitin, R. E. Palmer, J. A. Preece, S. D. Evans, and D. Fitzmaurice, "Gold nanoparticle patterning of silicon wafers using chemical e-beam lithography," *Langmuir*, vol. 20, no. 9, pp. 3766–3768, 2004.

[18] W. L. Brown, T. Venkatesan, and A. Wagner, "Ion beam lithography," *Nuclear Instruments and Methods in Physics Research*, vol. 191, no. 1-3, pp. 157–168, 1981.

[19] D. Lehr, K. Dietrich, C. Helgert, T. Käsebier, H.-J. Fuchs, A. Tünnermann, and E.-B. Kley, "Plasmonic properties of aluminum nanorings generated by double patterning," *Optics letters*, vol. 37, no. 2, pp. 157–159, 2012.

[20] G. M. Whitesides, J. P. Mathias, and C. T. Seto, "Molecular self-assembly and nanochemistry: a chemical strategy for the synthesis of nanostructures," tech. rep., DTIC Document, 1991.

[21] F. Caruso, H. Lichtenfeld, M. Giersig, and H. Möhwald, "Electrostatic self-assembly of silica nanoparticle-polyelectrolyte multilayers on polystyrene latex particles," *Journal of the American Chemical Society*, vol. 120, no. 33, pp. 8523–8524, 1998.

[22] A. M. Kalsin, M. Fialkowski, M. Paszewski, S. K. Smoukov, K. J. Bishop, and B. A. Grzybowski, "Electrostatic self-assembly of binary nanoparticle crystals with a diamond-like lattice," *Science*, vol. 312, no. 5772, pp. 420–424, 2006.

[23] S. Mühlig, A. Cunningham, S. Scheeler, C. Pacholski, T. Burgi, C. Rockstuhl, and F. Lederer, "Self-assembled plasmonic core–shell clusters with an isotropic magnetic dipole response in the visible range," *ACS nano*, vol. 5, no. 8, pp. 6586–6592, 2011.

[24] J. A. Fan, Y. He, K. Bao, C. Wu, J. Bao, N. B. Schade, V. N. Manoharan, G. Shvets, P. Nordlander, D. R. Liu, *et al.*, "Dna-enabled self-assembly of plasmonic nanoclusters," *Nano letters*, vol. 11, no. 11, pp. 4859–4864, 2011.

[25] A. Kuzyk, R. Schreiber, Z. Fan, G. Pardatscher, E.-M. Roller, A. Högele, F. C. Simmel, A. O. Govorov, and T. Liedl, "Dna-based self-assembly of chiral plasmonic nanostructures with tailored optical response," *Nature*, vol. 483, no. 7389, pp. 311–314, 2012.

[26] N. Landy, S. Sajuyigbe, J. Mock, D. Smith, and W. Padilla, "Perfect metamaterial absorber," *Physical review letters*, vol. 100, no. 20, p. 207402, 2008.

[27] N. Liu, M. Mesch, T. Weiss, M. Hentschel, and H. Giessen, "Infrared perfect absorber and its application as plasmonic sensor," *Nano letters*, vol. 10, no. 7, pp. 2342–2348, 2010.

[28] R. Alaee, M. Farhat, C. Rockstuhl, and F. Lederer, "A perfect absorber made of a graphene micro-ribbon metamaterial," *Optics express*, vol. 20, no. 27, pp. 28017–28024, 2012.

[29] J. B. Pendry, D. Schurig, and D. R. Smith, "Controlling electromagnetic fields," *Science*, vol. 312, no. 5781, pp. 1780–1782, 2006.

[30] U. Leonhardt, "Optical conformal mapping," *Science*, vol. 312, no. 5781, pp. 1777–1780, 2006.

[31] W. X. Jiang, T. J. Cui, X. M. Yang, Q. Cheng, R. Liu, and D. R. Smith, "Invisibility cloak without singularity," *Applied Physics Letters*, vol. 93, no. 19, 2008.

[32] T. Ergin, J. Fischer, and M. Wegener, "Optical phase cloaking of 700 nm light waves in the far field by a three-dimensional carpet cloak," *Physical Review Letters*, vol. 107, p. 173901, 2011.

[33] I. V. Lindell, A. Sihvola, S. Tretyakov, and A. Viitanen, *Electromagnetic waves in chiral and bi-isotropic media*. Artech House, 1994.

[34] M. Decker, M. Klein, M. Wegener, and S. Linden, "Circular dichroism of planar chiral magnetic metamaterials," *Optics letters*, vol. 32, no. 7, pp. 856–858, 2007.

[35] J. K. Gansel, M. Thiel, M. S. Rill, M. Decker, K. Bade, V. Saile, G. von Freymann, S. Linden, and M. Wegener, "Gold helix photonic metamaterial as broadband circular polarizer," *Science*, vol. 325, no. 5947, pp. 1513–1515, 2009.

[36] Y. Tang and A. E. Cohen, "Optical chirality and its interaction with matter," *Physical review letters*, vol. 104, no. 16, p. 163901, 2010.

[37] M. Ren, E. Plum, J. Xu, and N. I. Zheludev, "Giant nonlinear optical activity in a plasmonic metamaterial," *Nature communications*, vol. 3, p. 833, 2012.

[38] S. Linden, C. Enkrich, M. Wegener, J. Zhou, T. Koschny, and C. M. Soukoulis, "Magnetic response of metamaterials at 100 terahertz," *Science*, vol. 306, no. 5700, pp. 1351–1353, 2004.

[39] T.-J. Yen, W. Padilla, N. Fang, D. Vier, D. Smith, J. Pendry, D. Basov, and X. Zhang, "Terahertz magnetic response from artificial materials," *Science*, vol. 303, no. 5663, pp. 1494–1496, 2004.

[40] D. R. Smith, J. B. Pendry, and M. C. Wiltshire, "Metamaterials and negative refractive index," *Science*, vol. 305, no. 5685, pp. 788–792, 2004.

[41] V. M. Shalaev, "Optical negative-index metamaterials," *Nature photonics*, vol. 1, no. 1, pp. 41–48, 2007.

[42] J. Li and C. Chan, "Double-negative acoustic metamaterial," *Physical Review E*, vol. 70, no. 5, p. 055602, 2004.

[43] H. Chen and C. Chan, "Acoustic cloaking in three dimensions using acoustic metamaterials," *Applied physics letters*, vol. 91, no. 18, p. 183518, 2007.

[44] T. Bückmann, N. Stenger, M. Kadic, J. Kaschke, A. Frölich, T. Kennerknecht, C. Eberl, M. Thiel, and M. Wegener, "Tailored 3d mechanical metamaterials made by dip-in direct-laser-writing optical lithography," *Advanced Materials*, vol. 24, no. 20, pp. 2710–2714, 2012.

[45] T. Bückmann, M. Thiel, M. Kadic, R. Schittny, and M. Wegener, "An elastomechanical unfeelability cloak made of pentamode metamaterials," *Nature communications*, vol. 5, no. 4130, 2014.

[46] M. Farhat, S. Enoch, S. Guenneau, and A. Movchan, "Broadband cylindrical acoustic cloak for linear surface waves in a fluid," *Physical review letters*, vol. 101, no. 13, p. 134501, 2008.

[47] S. Guenneau, C. Amra, and D. Veynante, "Transformation thermodynamics: cloaking and concentrating heat flux," *Optics Express*, vol. 20, no. 7, pp. 8207–8218, 2012.

[48] Y. Ma, L. Lan, W. Jiang, F. Sun, and S. He, "A transient thermal cloak experimentally realized through a rescaled diffusion equation with anisotropic thermal diffusivity," *NPG Asia Materials*, vol. 5, no. 11, p. e73, 2013.

[49] J. Pendry, A. Holden, D. Robbins, and W. Stewart, "Low frequency plasmons in thin-wire structures," *Journal of Physics: Condensed Matter*, vol. 10, no. 22, p. 4785, 1998.

[50] P. Belov, R. Marques, S. Maslovski, I. Nefedov, M. Silveirinha, C. Simovski, and S. Tretyakov, "Strong spatial dispersion in wire media in the very large wavelength limit," *Physical Review B*, vol. 67, no. 11, p. 113103, 2003.

[51] Z. Bo, W. Zheng-Bin, Y. Zhen-Zhong, Z. Qi, Z. Jun-Ming, F. Yi-Jun, and J. Tian, "Planar metamaterial microwave absorber for all wave polarizations," *Chinese Physics Letters*, vol. 26, no. 11, p. 114102, 2009.

[52] S. Obrien, D. McPeake, S. Ramakrishna, and J. Pendry, "Near-infrared photonic band gaps and nonlinear effects in negative magnetic metamaterials," *Physical Review B*, vol. 69, no. 24, p. 241101, 2004.

[53] S. Zhang, W. Fan, N. Panoiu, K. Malloy, R. Osgood, and S. Brueck, "Experimental demonstration of near-infrared negative-index metamaterials," *Physical review letters*, vol. 95, no. 13, p. 137404, 2005.

[54] V. Yannopapas and A. Moroz, “Negative refractive index metamaterials from inherently non-magnetic materials for deep infrared to terahertz frequency ranges,” *Journal of physics: Condensed matter*, vol. 17, no. 25, p. 3717, 2005.

[55] C. Enkrich, M. Wegener, S. Linden, S. Burger, L. Zschiedrich, F. Schmidt, J. Zhou, T. Koschny, and C. Soukoulis, “Magnetic metamaterials at telecommunication and visible frequencies,” *Physical review letters*, vol. 95, no. 20, p. 203901, 2005.

[56] A. Alù and N. Engheta, “Optical nanotransmission lines: synthesis of planar left-handed metamaterials in the infrared and visible regimes,” *Journal of the Optical Society of America B*, vol. 23, no. 3, pp. 571–583, 2006.

[57] C. Rockstuhl, F. Lederer, C. Etrich, T. Pertsch, and T. Scharf, “Design of an artificial three-dimensional composite metamaterial with magnetic resonances in the visible range of the electromagnetic spectrum,” *Physical review letters*, vol. 99, no. 1, p. 017401, 2007.

[58] T. Xu, A. Agrawal, M. Abashin, K. J. Chau, and H. J. Lezec, “All-angle negative refraction and active flat lensing of ultraviolet light,” *Nature*, vol. 497, no. 7450, pp. 470–474, 2013.

[59] M. Hedayati, A. Zillohu, T. Strunskus, F. Faupel, and M. Elbahri, “Plasmonic tunable metamaterial absorber as ultraviolet protection film,” *Applied Physics Letters*, vol. 104, no. 4, p. 041103, 2014.

[60] G. Mie, “Beiträge zur optik trüber medien, speziell kolloidaler metallösungen,” *Annalen der physik*, vol. 330, no. 3, pp. 377–445, 1908.

[61] C. F. Bohren and D. R. Huffman, *Absorption and scattering of light by small particles*. John Wiley & Sons, 2008.

[62] M. I. Mishchenko, L. D. Travis, and A. A. Lacis, *Scattering, absorption, and emission of light by small particles*. Cambridge university press, 2002.

[63] Y.-l. Xu, “Electromagnetic scattering by an aggregate of spheres,” *Applied optics*, vol. 34, no. 21, pp. 4573–4588, 1995.

[64] S. Stein, “Addition theorems for spherical wave functions,” *Quarterly of Applied Mathematics*, pp. 15–24, 1961.

[65] L. Tsang, J. Kong, and R. Shin, *Theory of microwave remote sensing*. Wiley-Interscience, 1985.

[66] S. Tretyakov, *Analytical modeling in applied electromagnetics*. Artech House, 2003.

[67] C. Saeidi and D. van der Weide, “Nanoparticle array based optical frequency selective surfaces: theory and design,” *Optics Express*, vol. 21, no. 13, pp. 16170–16180, 2013.

[68] A. Alù, “Mantle cloak: Invisibility induced by a surface,” *Physical Review B*, vol. 80, p. 245115, 2009.

[69] P. B. Johnson and R. W. Christy, "Optical constants of the noble metals," *Physical Review B*, vol. 6, pp. 4370–4379, 1972.

[70] A. Sihvola and I. Lindell, "Polarizability and Effective Permittivity of Layered and Continuously Inhomogeneous Dielectric Spheres," *Journal of Electromagnetic Waves and Applications*, vol. 3, no. 1, pp. 37–60, 1989.

[71] A. Alù and N. Engheta, "Achieving transparency with plasmonic and metamaterial coatings," *Phys. Rev. E*, vol. 72, p. 016623, 2005.

[72] R. Fleury, J. Soric, and A. Alù, "Physical bounds on absorption and scattering for cloaked sensors," *Physical Review B*, vol. 89, no. 4, p. 045122, 2014.

[73] A. Monti, F. Bilotti, and A. Toscano, "Optical cloaking of cylindrical objects by using covers made of core–shell nanoparticles," *Optics letters*, vol. 36, no. 23, pp. 4479–4481, 2011.

[74] M. Calkin, "An invariance property of the free electromagnetic field," *American Journal of Physics*, vol. 33, pp. 958–960, 1965.

[75] W.-K. Tung, *Group theory in physics*. World Scientific, 1985.

[76] D. M. Lipkin, "Existence of a new conservation law in electromagnetic theory," *Journal of Mathematical Physics*, vol. 5, no. 5, pp. 696–700, 1964.

[77] I. Fernandez-Corbaton, X. Zambrana-Puyalto, N. Tischler, X. Vidal, M. L. Juan, and G. Molina-Terriza, "Electromagnetic duality symmetry and helicity conservation for the macroscopic maxwells equations," *Physical review letters*, vol. 111, no. 6, p. 060401, 2013.

[78] I. Fernandez-Corbaton and G. Molina-Terriza, "Role of duality symmetry in transformation optics," *Physical Review B*, vol. 88, no. 8, p. 085111, 2013.

[79] M. Kerker, D.-S. Wang, and C. Giles, "Electromagnetic scattering by magnetic spheres," *Journal of the Optical Society of America*, vol. 73, no. 6, pp. 765–767, 1983.

[80] X. Zambrana-Puyalto, I. Fernandez-Corbaton, M. Juan, X. Vidal, and G. Molina-Terriza, "Duality symmetry and kerker conditions," *Optics letters*, vol. 38, no. 11, pp. 1857–1859, 2013.

[81] F. Capolino, *Theory and phenomena of metamaterials*. CRC press, 2009.

[82] C. Simovski and S. Tretyakov, "Model of isotropic resonant magnetism in the visible range based on core-shell clusters," *Physical Review B*, vol. 79, no. 4, p. 045111, 2009.

[83] N. Liu, H. Guo, L. Fu, S. Kaiser, H. Schweizer, and H. Giessen, "Three-dimensional photonic metamaterials at optical frequencies," *Nature materials*, vol. 7, no. 1, pp. 31–37, 2008.

[84] A. I. Kuznetsov, A. B. Evlyukhin, C. Reinhardt, A. Seidel, R. Kiyan, W. Cheng, A. Ovsianikov, and B. N. Chichkov, "Laser-induced transfer of metallic nanodroplets for plasmonics and metamaterial applications," *Journal of the Optical Society of America B*, vol. 26, no. 12, pp. B130–B138, 2009.

[85] Y. A. Urzhumov, G. Shvets, J. A. Fan, F. Capasso, D. Brandl, and P. Nordlander, "Plasmonic nanoclusters: a path towards negative-index metafluids," *Optics express*, vol. 15, no. 21, pp. 14129–14145, 2007.

[86] J. Dintinger, B.-J. Tang, X. Zeng, F. Liu, T. Kienzler, G. H. Mehl, G. Ungar, C. Rockstuhl, and T. Scharf, "A self-organized anisotropic liquid-crystal plasmonic metamaterial," *Advanced Materials*, vol. 25, no. 14, pp. 1999–2004, 2013.

[87] L. Malassis, P. Massé, M. Tréguer-Delapierre, S. Mornet, P. Weisbecker, V. Kravets, A. Grigorenko, and P. Barois, "Bottom-up fabrication and optical characterization of dense films of meta-atoms made of core–shell plasmonic nanoparticles," *Langmuir*, vol. 29, no. 5, pp. 1551–1561, 2013.

[88] V. G. Veselago, "The electrodynamics of substances with simultaneously negative values of and?," *Soviet physics uspekhi*, vol. 10, no. 4, p. 509, 1968.

[89] S. Campione, M. Albani, and F. Capolino, "Complex modes and near-zero permittivity in 3d arrays of plasmonic nanoshells: loss compensation using gain [invited]," *Optical Materials Express*, vol. 1, no. 6, pp. 1077–1089, 2011.

[90] C. M. Soukoulis, S. Linden, and M. Wegener, "Negative refractive index at optical wavelengths," *Science*, vol. 315, no. 5808, pp. 47–49, 2007.

[91] S. P. Burgos, R. de Waele, A. Polman, and H. A. Atwater, "A single-layer wide-angle negative-index metamaterial at visible frequencies," *Nature Materials*, vol. 9, no. 5, pp. 407–412, 2010.

[92] C. Menzel, R. Alaee, E. Pshenay-Severin, C. Helgert, A. Chipouline, C. Rockstuhl, T. Pertsch, and F. Lederer, "Genuine effectively biaxial left-handed metamaterials due to extreme coupling," *Optics letters*, vol. 37, no. 4, pp. 596–598, 2012.

[93] E. Prodan, C. Radloff, N. J. Halas, and P. Nordlander, "A hybridization model for the plasmon response of complex nanostructures," *Science*, vol. 302, no. 5644, pp. 419–422, 2003.

[94] B. G. Prevo, S. A. Esakoff, A. Mikhailovsky, and J. A. Zasadzinski, "Scalable routes to gold nanoshells with tunable sizes and response to near-infrared pulsed-laser irradiation," *Small*, vol. 4, no. 8, pp. 1183–1195, 2008.

[95] T. Liu, D. Li, D. Yang, and M. Jiang, "An improved seed-mediated growth method to coat complete silver shells onto silica spheres for surface-enhanced raman scattering," *Colloids and Surfaces A: Physicochemical and Engineering Aspects*, vol. 387, no. 1, pp. 17–22, 2011.

[96] P. K. Jain and M. A. El-Sayed, "Plasmonic coupling in noble metal nanostructures," *Chemical Physics Letters*, vol. 487, no. 4, pp. 153–164, 2010.

[97] R. Zhang, Y. Zhang, Z. Dong, S. Jiang, C. Zhang, L. Chen, L. Zhang, Y. Liao, J. Aizpurua, Y. e. Luo, *et al.*, "Chemical mapping of a single molecule by plasmon-enhanced raman scattering," *Nature*, vol. 498, no. 7452, pp. 82–86, 2013.

[98] D. R. Shankaran, K. V. Gobi, and N. Miura, "Recent advancements in surface plasmon resonance immunosensors for detection of small molecules of biomedical, food and environmental interest," *Sensors and Actuators B: Chemical*, vol. 121, no. 1, pp. 158–177, 2007.

[99] X. Wang, P. Wang, C. Chen, J. Chen, Y. Lu, H. Ming, and Q. Zhan, "Plasmonic racetrack resonator with high extinction ratio under critical coupling condition," *Journal of Applied Physics*, vol. 107, no. 12, p. 124517, 2010.

[100] R. Pérez-Pineiro, M. A. Correa-Duarte, V. Salgueirino, and R. A. Alvarez-Puebla, "Sers assisted ultra-fast peptidic screening: a new tool for drug discovery," *Nanoscale*, vol. 4, no. 1, pp. 113–116, 2012.

[101] L. Rodríguez-Lorenzo, Z. Krpetic, S. Barbosa, R. A. Alvarez-Puebla, L. M. Liz-Marzán, I. A. Prior, and M. Brust, "Intracellular mapping with sers-encoded gold nanostars," *Integrative Biology*, vol. 3, no. 9, pp. 922–926, 2011.

[102] T. Nagatsuka, H. Uzawa, K. Sato, S. Kondo, M. Izumi, K. Yokoyama, I. Ohsawa, Y. Seto, P. Neri, H. Mori, *et al.*, "Localized surface plasmon resonance detection of biological toxins using cell surface oligosaccharides on glyco chips," *ACS applied materials & interfaces*, vol. 5, no. 10, pp. 4173–4180, 2013.

[103] M. Wegener, "Nano-plasmonics for bio-photonics," in *Biophotonics: Spectroscopy, Imaging, Sensing, and Manipulation*, pp. 19–23, Springer Netherlands, 2011.

[104] D. Graham, D. G. Thompson, W. E. Smith, and K. Faulds, "Control of enhanced raman scattering using a dna-based assembly process of dye-coded nanoparticles," *Nature nanotechnology*, vol. 3, no. 9, pp. 548–551, 2008.

[105] M. Homberger, S. Schmid, J. Timper, and U. Simon, "Solid phase supported click-chemistry approach for the preparation of water soluble gold nanoparticle dimers," *Journal of Cluster Science*, vol. 23, no. 4, pp. 1049–1059, 2012.

[106] X. Liu, H. Liu, W. Zhou, H. Zheng, X. Yin, Y. Li, Y. Guo, M. Zhu, C. Ouyang, D. Zhu, *et al.*, "Thermoreversible covalent self-assembly of oligo (p-phenylenevinylene) bridged gold nanoparticles," *Langmuir*, vol. 26, no. 5, pp. 3179–3185, 2009.

[107] W. P. McConnell, J. P. Novak, L. C. Brousseau, R. R. Fuierer, R. C. Tenent, and D. L. Feldheim, "Electronic and optical properties of chemically modified metal nanoparticles and molecularly bridged nanoparticle arrays," *The Journal of Physical Chemistry B*, vol. 104, no. 38, pp. 8925–8930, 2000.

[108] J. M. Wessels, H.-G. Nothofer, W. E. Ford, F. von Wrochem, F. Scholz, T. Vossmeyer, A. Schroedter, H. Weller, and A. Yasuda, "Optical and electrical properties of three-dimensional interlinked gold nanoparticle assemblies," *Journal of the American Chemical Society*, vol. 126, no. 10, pp. 3349–3356, 2004.

[109] M. Orbach, M. Lahav, P. Milko, S. G. Wolf, and M. E. van der Boom, "Setting the environmental conditions for controlling gold nanoparticle assemblies," *Angewandte Chemie International Edition*, vol. 51, no. 29, pp. 7142–7145, 2012.

[110] M. P. Stemmler, Y. Fogel, K. Mullen, and M. Kreiter, "Bridging of gold nanoparticles by functional polyphenylene dendrimers," *Langmuir*, vol. 25, no. 19, pp. 11917–11922, 2009.

[111] J. Turkevich, P. C. Stevenson, and J. Hillier, "A study of the nucleation and growth processes in the synthesis of colloidal gold," *Discussions of the Faraday Society*, vol. 11, pp. 55–75, 1951.

[112] A. Singh, D. H. Dahanayaka, A. Biswas, L. A. Bumm, and R. L. Halterman, "Molecularly ordered decanethiolate self-assembled monolayers on au (111) from in situ cleaved decanethioacetate: An nmr and stm study of the efficacy of reagents for thioacetate cleavage," *Langmuir*, vol. 26, no. 16, pp. 13221–13226, 2010.

[113] D.-H. Tsai, L. F. Pease III, R. Zangmeister, M. J. Tarlov, and M. Zachariah, "Aggregation kinetics of colloidal particles measured by gas-phase differential mobility analysis," *Langmuir*, vol. 25, no. 1, pp. 140–146, 2008.

[114] M. K. Brakke, "Density gradient centrifugation: A new separation technique," *Journal of the American Chemical Society*, vol. 73, no. 4, pp. 1847–1848, 1951.

[115] G. Chen, Y. Wang, L. H. Tan, M. Yang, L. S. Tan, Y. Chen, and H. Chen, "High-purity separation of gold nanoparticle dimers and trimers," *Journal of the American Chemical Society*, vol. 131, no. 12, pp. 4218–4219, 2009.

[116] S. Mühlig, C. Menzel, C. Rockstuhl, and F. Lederer, "Multipole analysis of meta-atoms," *Metamaterials*, vol. 5, no. 2, pp. 64–73, 2011.

[117] F. Kretschmer, U. Mansfeld, S. Hoeppener, M. D. Hager, and U. S. Schubert, "Tunable synthesis of poly (ethylene imine)–gold nanoparticle clusters," *Chemical Communications*, vol. 50, no. 1, pp. 88–90, 2014.

[118] C. Ziegler and A. Eychmuller, "Seeded growth synthesis of uniform gold nanoparticles with diameters of 15- 300 nm," *The Journal of Physical Chemistry C*, vol. 115, no. 11, pp. 4502–4506, 2011.

[119] S. D. Perrault and W. C. Chan, "Synthesis and surface modification of highly monodispersed, spherical gold nanoparticles of 50- 200 nm," *Journal of the American Chemical Society*, vol. 131, no. 47, pp. 17042–17043, 2009.

[120] N. R. Jana, L. Gearheart, and C. J. Murphy, "Evidence for seed-mediated nucleation in the chemical reduction of gold salts to gold nanoparticles," *Chemistry of Materials*, vol. 13, no. 7, pp. 2313–2322, 2001.

[121] M. J. Dicken, K. Aydin, I. M. Pryce, L. A. Sweatlock, E. M. Boyd, S. Walavalkar, J. Ma, and H. A. Atwater, "Frequency tunable near-infrared metamaterials based on vo 2 phase transition," *Optics express*, vol. 17, no. 20, pp. 18330–18339, 2009.

[122] C. Zhao, Y. Liu, Y. Zhao, N. Fang, and T. J. Huang, "A reconfigurable plasmofluidic lens," *Nature communications*, vol. 4, 2013.

[123] M. Wojcik, W. Lewandowski, J. Matraszek, J. Mieczkowski, J. Borysiuk, D. Pociecha, and E. Gorecka, "Liquid-crystalline phases made of gold nanoparticles," *Angewandte Chemie International Edition*, vol. 48, no. 28, pp. 5167–5169, 2009.

[124] W. Lewandowski, K. Jatczak, D. Pociecha, and J. Mieczkowski, "Control of gold nanoparticle superlattice properties via mesogenic ligand architecture," *Langmuir*, vol. 29, no. 10, pp. 3404–3410, 2013.

[125] W. Lewandowski, D. Constantin, K. Walicka, D. Pociecha, J. Mieczkowski, and E. Górecka, "Smectic mesophases of functionalized silver and gold nanoparticles with anisotropic plasmonic properties," *Chemical Communications*, vol. 49, no. 71, pp. 7845–7847, 2013.

[126] J. Pomplun, S. Burger, L. Zschiedrich, and F. Schmidt, "Adaptive finite element method for simulation of optical nano structures," *physica status solidi (b)*, vol. 244, no. 10, pp. 3419–3434, 2007.

[127] D. Smith, S. Schultz, P. Markoš, and C. Soukoulis, "Determination of effective permittivity and permeability of metamaterials from reflection and transmission coefficients," *Physical Review B*, vol. 65, no. 19, p. 195104, 2002.

[128] D. Traviss, R. Bruck, B. Mills, M. Abb, and O. L. Muskens, "Ultrafast plasmonics using transparent conductive oxide hybrids in the epsilon-near-zero regime," *Applied Physics Letters*, vol. 102, no. 12, p. 121112, 2013.

[129] P. Waterman, "Matrix formulation of electromagnetic scattering," *Proceedings of the IEEE*, vol. 53, no. 8, pp. 805–812, 1965.

[130] M. Mishchenko and J. Dlugach, "Coherent backscatter and the opposition effect for e-type asteroids," *Planetary and space science*, vol. 41, no. 3, pp. 173–181, 1993.

[131] T. Nieminen, H. Rubinsztein-Dunlop, and N. Heckenberg, "Calculation of the t-matrix: general considerations and application of the point-matching method," *Journal of Quantitative Spectroscopy and Radiative Transfer*, vol. 79, pp. 1019–1029, 2003.

[132] V. Yannopapas, "Layer-multiple-scattering method for photonic structures of general scatterers based on a discrete-dipole approximation/t-matrix point-matching method," *Journal of the Optical Society of America B*, vol. 31, no. 3, pp. 631–636, 2014.

[133] Z. Gimbutas and L. Greengard, "Fast multi-particle scattering: A hybrid solver for the maxwell equations in microstructured materials," *Journal of Computational Physics*, vol. 232, no. 1, pp. 22–32, 2013.

[134] L. N. Trefethen and D. Bau III, *Numerical linear algebra*, vol. 50. Siam, 1997.

[135] M. I. Mishchenko, L. D. Travis, and D. W. Mackowski, "T-matrix computations of light scattering by nonspherical particles: a review," *Journal of Quantitative Spectroscopy and Radiative Transfer*, vol. 55, no. 5, pp. 535–575, 1996.

[136] J. Li and J. B. Pendry, "Hiding under the carpet: A new strategy for cloaking," *Physical Review Letters*, vol. 101, p. 203901, 2008.

[137] J. Valentine, J. Li, T. Zentgraf, G. Bartal, and X. Zhang, "An optical cloak made of dielectrics," *Nature materials*, vol. 8, no. 7, pp. 568–571, 2009.

[138] J. H. Lee, J. Blair, V. A. Tamma, Q. Wu, S. J. Rhee, C. J. Summers, and W. Park, "Direct visualization of optical frequency invisibility cloak based on silicon nanorod array," *Optics Express*, vol. 17, no. 15, pp. 12922–12928, 2009.

[139] M. G. Silveirinha, A. Alù, and N. Engheta, "Infrared and optical invisibility cloak with plasmonic implants based on scattering cancellation," *Physical Review B*, vol. 78, p. 075107, 2008.

[140] F. Bilotti, S. Tricarico, and L. Vegni, "Electromagnetic cloaking devices for TE and TM polarizations," *New Journal of Physics*, vol. 10, no. 11, p. 115035, 2008.

[141] A. Monti, A. Alù, A. Toscano, and F. Bilotti, "Optical invisibility through metasurfaces made of plasmonic nanoparticles," *Journal of Applied Physics*, vol. 117, no. 12, p. 123103, 2015.

[142] A. Monti, A. Alù, A. Toscano, and F. Bilotti, "Optical scattering cancellation through arrays of plasmonic nanoparticles: A review," in *Photonics*, vol. 2, pp. 540–552, Multidisciplinary Digital Publishing Institute, 2015.

[143] M. Kerker, "Invisible bodies," *Journal of the Optical Society of America*, vol. 65, no. 4, pp. 376–379, 1975.

[144] F. Bilotti, S. Tricarico, F. Pierini, and L. Vegni, "Cloaking apertureless near-field scanning optical microscopy tips," *Optics Letters*, vol. 36, no. 2, pp. 211–213, 2011.

[145] S. Tricarico, F. Bilotti, and L. Vegni, "Reduction of optical forces exerted on nanoparticles covered by scattering cancellation based plasmonic cloaks," *Physical Review B*, vol. 82, p. 045109, 2010.

[146] D. Rainwater, A. Kerkhoff, K. Melin, J. Soric, G. Moreno, and A. Alù, "Experimental verification of three-dimensional plasmonic cloaking in free-space," *New Journal of Physics*, vol. 14, no. 1, p. 013054, 2012.

[147] S. Mühlig, M. Farhat, C. Rockstuhl, and F. Lederer, "Cloaking dielectric spherical objects by a shell of metallic nanoparticles," *Physical Review B*, vol. 83, p. 195116, 2011.

[148] S. Mühlig, A. Cunningham, J. Dintinger, M. Farhat, S. B. Hasan, T. Scharf, T. Bürgi, F. Lederer, and C. Rockstuhl, "A self-assembled three-dimensional cloak in the visible," *Scientific reports*, vol. 3, no. 2328, 2013.

[149] A. Monti, A. Alù, A. Toscano, and F. Bilotti, "Optical invisibility through metasurfaces made of plasmonic nanoparticles," *Journal of Applied Physics*, vol. 117, no. 12, p. 123103, 2015.

[150] J. Park and W. Lu, "Orientation of core-shell nanoparticles in an electric field," *Applied Physics Letters*, vol. 91, no. 5, 2007.

[151] C. J. Murphy, T. K. Sau, A. M. Gole, C. J. Orendorff, J. Gao, L. Gou, S. E. Hunyadi, and T. Li, "Anisotropic metal nanoparticles: synthesis, assembly, and optical applications," *The Journal of Physical Chemistry B*, vol. 109, no. 29, pp. 13857–13870, 2005.

[152] A. B. Buda and K. Mislow, "A hausdorff chirality measure," *Journal of the American Chemical Society*, vol. 114, no. 15, pp. 6006–6012, 1992.

[153] M. Petitjean, "Chirality and symmetry measures: A transdisciplinary review," *Entropy*, vol. 5, no. 3, pp. 271–312, 2003.

[154] A. Rassat and P. W. Fowler, "Is there a most chiral tetrahedron?," *Chemistry–A European Journal*, vol. 10, no. 24, pp. 6575–6580, 2004.

[155] N. Weinberg and K. Mislow, "On chirality measures and chirality properties," *Canadian Journal of Chemistry*, vol. 78, no. 1, pp. 41–45, 2000.

[156] R. P. Cameron, S. M. Barnett, and A. M. Yao, "Optical helicity, optical spin and related quantities in electromagnetic theory," *New Journal of Physics*, vol. 14, no. 5, p. 053050, 2012.

[157] H. A. Wheeler, "A helical antenna for circular polarization," *Proceedings of the IRE*, vol. 35, no. 12, pp. 1484–1488, 1947.

[158] Y. Ra'di and S. A. Tretyakov, "Balanced and optimal bianisotropic particles: maximizing power extracted from electromagnetic fields," *New Journal of Physics*, vol. 15, no. 5, p. 053008, 2013.

[159] E. M. Hicks, S. Zou, G. C. Schatz, K. G. Spears, R. P. Van Duyne, L. Gunnarsson, T. Rindzevicius, B. Kasemo, and M. Käll, "Controlling plasmon line shapes through diffractive coupling in linear arrays of cylindrical nanoparticles fabricated by electron beam lithography," *Nano letters*, vol. 5, no. 6, pp. 1065–1070, 2005.